Advanced Silicon Photonic Microcavities for Routing, Detection and Lasing Applications

by

Zhan Su

S.M. (Electrical Engineering and Computer Science)
Massachusetts Institute of Technology (2013)

Submitted to the Department of Electrical Engineering and Computer Science
in partial fulfillment of the requirements of the degree of

Doctor of Philosophy in Electrical Engineering

at the

MASSACHUSETTS INSTITUTE OF TECHNOLOGY

February 2017

Author .....

Department of Electrical Engineering and Computer Science

December 6, 2016

Certified by .....

Michael R. Watts

Associate Professor of Electrical Engineering

Thesis Supervisor

Accepted by .....

Leslie A. Kolodziejski

Professor of Electrical Engineering

Chair, Department Committee on Graduate Students

Advanced Silicon Photonic Microcavities for Routing, Detection and Lasing Applications

by

Zhan Su

Submitted to the Department of Electrical Engineering and Computer Science
on December 6, 2016, in partial fulfillment of the
requirements of the degree of
Doctor of Philosophy in Electrical Engineering

Abstract

The theoretical background of microcavities for photonic applications has been extensively investigated in theory over the past two decades. These structures provide the ability to filter wavelength, support high-Q modes and enhance intensity within the cavities while maintaining a small device footprint. Such characteristics make these structures good candidates to optimize performance and shrink the size of devices for both linear and nonlinear optics. Recent advancements in silicon-based fabrication technology provide access to dopants for active control, material layers such as germanium and silicon nitride, and 3D-integration technologies that were previously exclusive to electronics development, leading to tremendous progress in cavity-based integrated photonic circuits.

Using the silicon photonic platform developed by our group, high-performance microcavity-based structures have been demonstrated for optical signal routing, detection, and lasing applications. We first introduce partial-drop filters and present results using them to achieve a highly uniform wavelength-division-multiplexing (WDM) compatible optical multicast system. We then implement a waveguide-coupled resonant detector using a germanium layer grown on top of the silicon. In addition to having low dark current and high-speed performance, the resonant detector extends the wavelength detection range beyond 1620nm while maintaining a device radius only 4.5µm. Furthermore, an easy-to-fabricate waveguide-coupled trench-based Al_2O_3 microcavity is presented that achieves a Q-factor on the order of 10^6 with a bend radius on the scale of 100µm. Compact on-chip rare-earth-ion (ytterbium, erbium, thulium) doped Al_2O_3 lasers were then demonstrated with a sub-milliwatt lasing threshold, making trench-based cavities a suitable platform to achieve optically pumped on-chip lasers.

Thesis Supervisor: Michael R. Watts
Title: Associate Professor of Electrical Engineering

Preface and Acknowledgement

The past five and a half years at MIT have been a great experience in my life. During the period, I have not only gained knowledge on the research I have been focusing on but also learned how to work in a team and lead projects when I became more experienced.

First and foremost, I was privileged to have the opportunity to join Prof. Michael R. Watts's group. The day when I received his response that I can join his team is one of the best moment in my life. Over the past five and a half years, under his lead, we started with a small group with a little amount of equipment to a big lab with plenty of resources. His visions and passions on electronics-photonics 3D integration and on-chip laser designs provided us with great motivations and further guide the silicon photonics research into practical industrialization. BBQ and fishing trip during summer and Fire and Ice get-together during Christmas have been great memories shared by all the group members.

I am also grateful to have Prof. Erich P. Ippen on my thesis committee. Listening to his comments during project meeting and witnessing those moments when ideas came so naturally from him have been a great experience in my Ph.D. life. His encouragement and suggestions during my thesis committee meeting and thesis writing process helped me better understand the physics behind my thesis topics.

I would also like to thank Prof. Qing Hu for being one of my committee members. The time I spent in his 6.730 class during my first year not only helped me with a better understanding of solid-state physics but also provided me with a chance to collaborate with other students, who later have become my great friends and strong supports through my Ph.D. life.

I also want to thank Dr. Erman Timurdogan for his help over the past few years. I am very grateful to be his officemate and labmate. The days we spent together discussing technological designs and experiments gave us not only a deeper understanding of our research topics but also a great friendship. As a student who joined the group one year earlier than me, he helped me from the beginning of electromagnetic FDTD simulation and Cadence mask layout to further collaboration work on electronics-photonics integration. It has been a great experience to work back-to-

back in the same office, go to different places (Stata Center first floor, ground floor, student center, Starbucks in Kendall Square) for the same coffee during weekdays or sometimes weekends. Also, while getting a Ph.D. needs a lot of patience, as a life-long friend, he can always give me useful advice on dealing with different situations from his experience.

I would also like to thank my colleague Dr. Jie Sun for his help. As a pioneer in phased array in our group, he has left a rich and great legacies that laid down the foundation of silicon photonic phased array. I am so grateful to be his officemate and had the chance to work with him on a variety of research topics. His advice on research and future jobs have helped me figuring out what I want to achieve from my Ph.D. works.

I also want to thank Dr. Jonathan D. B. Bradley (now Prof. Bradley) for his great help in guiding my research. I am particularly impressed by his dedication to research. Getting a fabrication system up and running requires great effort. I was grateful to have worked with him on thulium laser development and seeing my thulium microcavity laser design worked from his film deposition was one of the greatest moment during my Ph.D. research.

MIT has been a great place to conduct research not only because of the abundant technical resources on campus but also talent people around me. I also want to thank my labmates Christopher Poulton, Manan Raval, Matthew Byrd, Jelena Notaros, Diedrik Vermeulen, Patrick Callahan, Katia Shtyrkova, Michele Moresco, Ehsan Hosseini, Purnawirman, Jerry Zhou, Nanxi Li, Salih Magden, Neetesh Singh, Alfonso Ruocco, Ami Yaacobi, David Cole, Anna Baldycheva, Cheri Sorace-Agaskar, and Aleksandr Biberman for all the time that they have spent with me.

In addition, I want to thank people from other groups, Guolong Su, Jinshuo Zhang, Ningren Han, Huaiyu Meng, Shengxi Huang, Tao Yu, Yang Yang, Qiu Xin, Xun Cai, Yichen Shen, Bo Zhen, Hung-Wen Chen, Duo Li, Hangbo Zhao, Longwu Ou, David Burghoff, Karan Mehta, Amir Atabaki and Luca Alloatti, for useful discussions and allowing me to borrow their equipment for experiment.

Last but not least, I would like to thank my wife and my parents for their constant support and consideration. Thanks for bringing the sunshine into my life and making

my life colorful.

This thesis is dedicated to my family ...

Contents

List of Figures

List of Tables

CHAPTER 1

Introduction

In this chapter, an introduction to foundry-based silicon photonics is presented, covering the on-chip laser source, transmitter and receiver platform developed through collaboration between MIT and SUNY Polytechnic Institute. The advantages of microcavities as building blocks for those applications are discussed. Finally, the layout of this thesis is presented.

1.1 Foundry-Based Silicon Photonics

With the scaling of chip multicore microprocessor systems, communications between the cores on a chip and between the cores and memory systems off-chip have become the limiting factor affecting system performance [1]. Integrated photonics provide a solution for both on- and off-chip communications, enabling massive bandwidths with low power consumption [2, 3]. While communications are driving the current interest in silicon photonics, the resulting silicon photonic platforms can be applied to various problems, ranging from sensing and phased arrays to microwave photonics and quantum optics. These platforms often achieve degrees of performance that cannot be achieved with their free-space optic counterparts [4, 5]. The general applicability of these platforms is determined by the extensibility of their component libraries. From active components such as modulators [3, 6, 7], switches [8], detectors [9], and even lasers [10, 11] to passive components such as 3dB couplers [12] and waveguide crossings [13], component libraries within silicon photonic platforms are becoming increasingly general. To further increase the integration density and take full advantage of current CMOS technology, a well-established yet flexible platform needs to be implemented and compact yet reliable building blocks are required.

In our group, through collaborations with Colleges of Nanoscale Science and Engineering (CNSE) in SUNY Polytechnic University and UC Berkeley, we have developed a platform which includes both photonics and electronics for a wafer-to-wafer bonding process [14, 15, 16]. Inside of this platform, we have incorporated two materials – silicon and silicon nitride, for optical waveguiding. We also add several doping layers of N and P dopants with different concentrations and two metal layers for active control of devices. For laser sources and receivers design, rare-earth-ion-doped Al_2O_3 is deposited as an on-chip gain material while a germanium layer is used for optical power detection. Through direct connections with state-of-art production facilities, we can not only create proof-of-concept devices or systems but also test the reliability of them in a real wafer-scale production.

Fig. 1.1(a-c) shows three major layer stacks of the platform. We started the platform development with a passive silicon layer. This enables devices such as compact

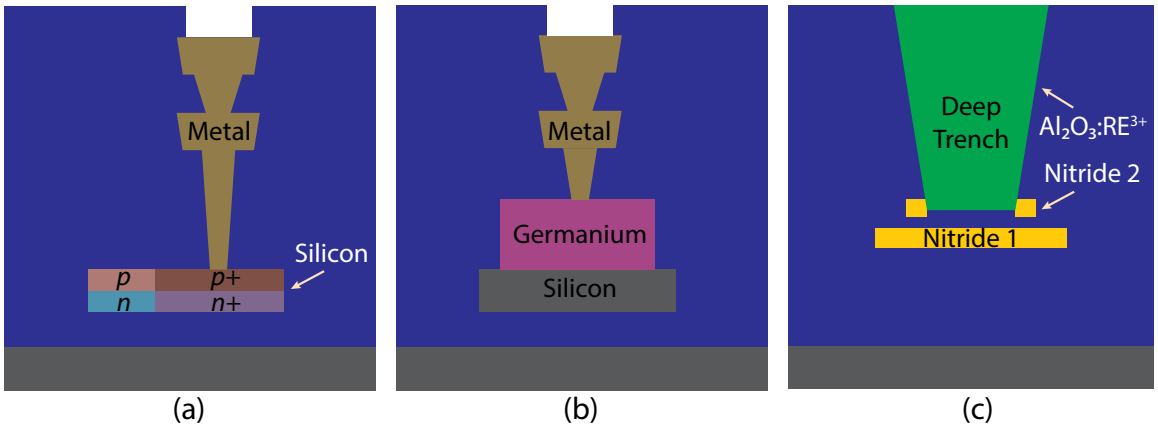

Fig. 1.1: (a) Silicon layer with dopants of different types (p- or n-type) and concentrations for applications such as modulators or tunable filters. (b) Germanium on silicon layer for photodetection applications. (c) Two silicon nitride layers (nitride 1 and nitride 2) with a deep trench on top for the on-chip optically pumped laser development.

vertical emitters [4], polarization beam splitters [17, 18] and adiabatic microring cavities [19]. The highly uniform and large-scale fabrication process made it possible to have over 10,000 optical devices working together within mm×mm scale [4, 20, 21, 22]. Though the development of passive devices enables the creation of large-scale photonic circuits, applications of passive devices are limited due to lack of the ability to actively manipulate light on a chip such as data encoding through modulation and beam steering via phase control. Therefore, we introduced an active light control by incorporating doping layers into silicon, as shown in Fig. 1.1(a), to utilize its thermal and electric properties. With the help of the carrier plasma effect [23], both the real and imaginary part of silicon refractive index can be modulated by introducing carriers to or extracting them from silicon, enabling dynamic light modulation with ultra low power consumption [3]. In addition, the large thermal coefficient of silicon material combined with the introduction of a doping layer as a local heater makes it easier to implement efficient thermal phase shifters on chip [4, 24, 25, 26, 27]. By connecting the doping layers to upper metal layers, active devices can be individually controlled by external electrical drivers.

Although silicon is an excellent material for waveguiding, modulating and shifting on-chip light, it is not an efficient material for either light detection or light generation.

Therefore, we utilized germanium and silicon nitride that have been widely used in CMOS foundries to provide these two functions in the platform. Fig. 1.1(b) shows the layer stack of the germanium detector. Intrinsic germanium is epitaxially grown on top of the silicon, and the top part of the germanium material is doped with an n-type dopant and contacted with metals on top. By introducing a p-type dopant into the bottom silicon, a vertical p-i-n junction is formed to achieve the photodetection function.

For the laser related layer stacks (shown in Fig. 1.1(c)), we utilize a rare-earth-ion-doped glass approach to take advantage of its low noise and narrow linewidth. However, the disadvantages of this laser type are low gain per unit length and the requirement of optical pumping. The former requires a low-loss material at the signal wavelength to enable a low-loss cavity design, while the latter requires the material to be low-loss at the pump wavelength to reduce pump power attenuation. Therefore, we utilize silicon nitride as a waveguiding material for its capability to be low-loss for a broad range of wavelengths and a deep trench for rare-earth-ion-doped Al_2O_3 deposition outside of the CMOS foundry.

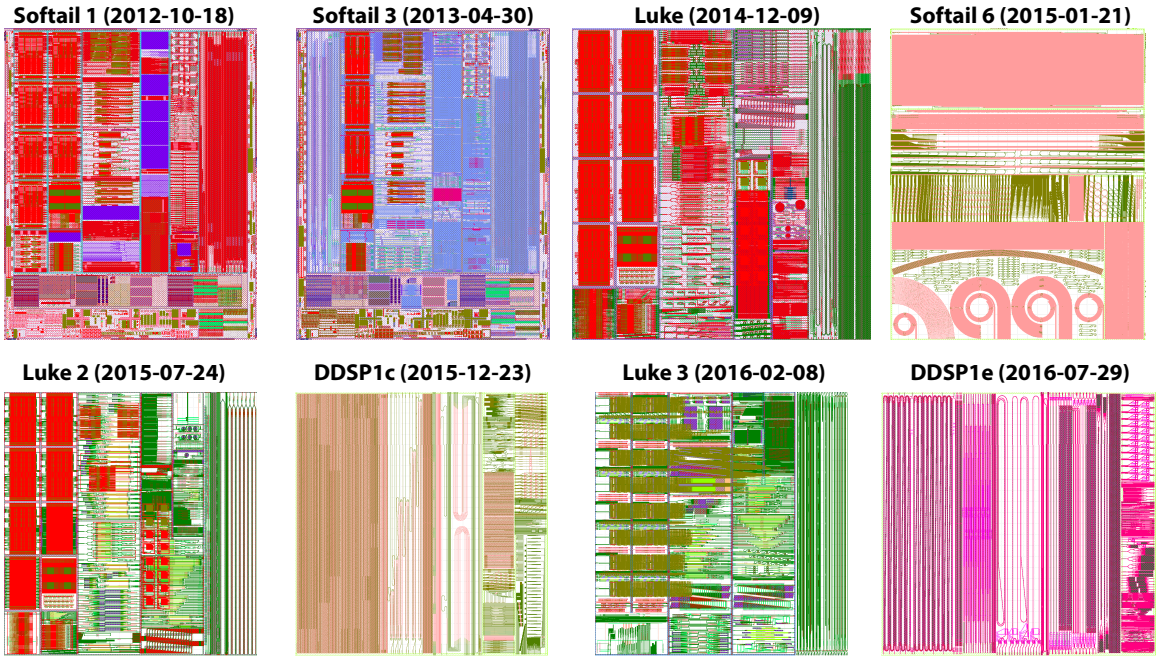

Fig. 1.2: Masks taped out during my Ph.D. study.

During my Ph.D. study, I was actively involved in eight different tapeouts (snap-

shots of the masks are shown in Fig. 1.2, covering a variety of topics such as optical routing system [28, 29, 30], on-chip polarization manipulation devices [17], germanium-on-silicon detector development [31], rare-earth-ion-doped Al_2O_3-based laser [11, 32], wafer-scale fabrication tolerance measurement of microcavity [19], and electronics-photonics 3D integration system [14]).

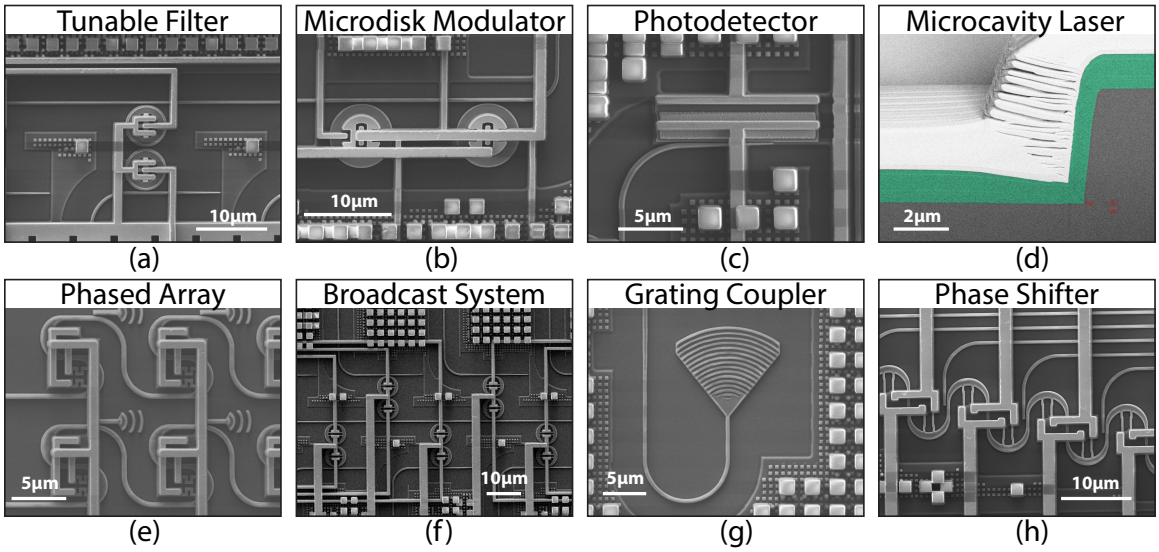

Fig. 1.3: A gallery of silicon photonic devices fabricated in the platform developed by MIT and SUNY Polytechnic Institute. Top-view SEMs were taken after a reactive-ion-etching (RIE) of the SiO_2 cladding material. (a) A second-order tunable microring filter. (b) Two microdisk modulators. (c) A waveguide-coupled Ge-on-Si photodetector. (d) The cross-section of a microcavity laser. (e) A two-dimensional phased array with a dynamic thermal tuning. (f) A microring-based optical broadcast/multicast system. (g) A grating coupler. (h) A set of cadcaded thermal phase shifters.

Based on the platform developed, we have designed and tested a wide variety of building blocks for silicon photonics. Examples of devices developed in our group at MIT are shown in Fig. 1.3, covering components such as a grating coupler, tunable filter, modulator, photodetector, microcavity laser, and system-level demonstrations such as a large-scale phased array and optical broadcast system.

While most foundry-based processes are rigid and design rules are not flexible, the platform we developed together with CNSE, SUNY Polytechnic Institute is more extensive with the capabilities such as material thickness adjustment, deep trench formation, III-V material to silicon bonding (wafer-to-wafer or metal-to-metal) and

electronics-photonics 3D integration. The flexibility of the platform not only facilitates commercialization of silicon photonics in the communication and data-center industry, but also enables a large variety of new applications such as LIDAR, biosensing, and quantum computations.

1.2 Microcavities

Theories on microcavities were extensively investigated two decades ago [33]. A variety of experimental demonstrations of microcavities in laser implementations [11, 32], modulators [3, 6, 7], and detectors [34, 31, 35] have been achieved following the advancement in fabrication technologies. Regarding device level performance, microcavities can be 10 to 100 times better than non-resonant devices while maintaining a much more compact footprint. However, problems such as fabrication tolerance and process dependence [36] of microcavity designs make it hard to achieve complex photonic circuits. Therefore, robust designs of microcavities and a standardized fabrication platform that can provide devices for various applications have become a necessity.

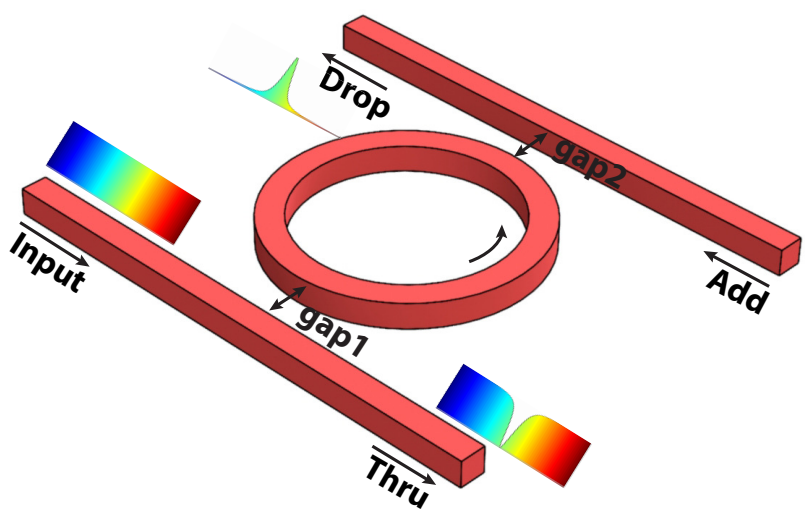

Fig. 1.4: An illustration of a waveguide-coupled microcavity used as a channel-dropping filter.

There are several advantages associated with microcavities. The first one is the wavelength-division-multiplexing compatibility by using a microcavity as a channel-dropping filter (shown in Fig. 1.4), which is a common property for resonant-based

structures. With a low-loss waveguide, data carried by the resonant wavelength/frequency can be selected by the microcavity and directed to drop ports of the filter with only a small amount of power loss, making it a good candidate for WDM-compatible routing systems. In Chap. 2 of this thesis, we will introduce a partial-drop filter as a new concept, which is capable of selecting only part of the input power while still maintaining the wavelength selectivity of the microcavity. With the help of partial-drop filter, further simplifications of optical multicasting networks can be achieved.

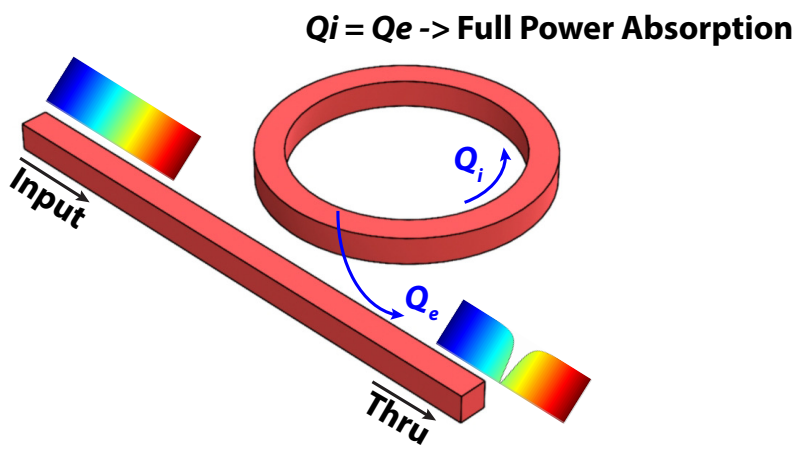

Fig. 1.5: An illustration of a waveguide-coupled microcavity used as an high-efficiency absorber. Q_i denotes the intrinsic Q-factor of the cavity and Q_e represents the external Q-factor. When $Q_i = Q_e$, full power absorption can be achieved when the input wavelength matches one of the resonances in the cavity.

The second property is the Q-matching feature of the microcavity. As shown in Fig. 1.5, for a microcavity coupled to an external source input (e.g. in Fig. 1.5, the cavity is coupled to a bus waveguide), apart from separate resonances determined by the discrete modes within the cavity, the response of the cavity is also affected by both the loss inside the cavity (denoted as quality factor Q_i) and the coupling to the bus waveguide (indicated by quality factor Q_e). When the condition $Q_i = Q_e$ is satisfied for the resonant wavelength, the microcavity will be able to trap the input light in the microcavity, providing a full absorption of the light. This concept is very useful for structures such as detectors for which a full absorption of the input power is necessary. The idea will be discussed more in Chap. 3 with both theoretical analysis

and experimental demonstrations.

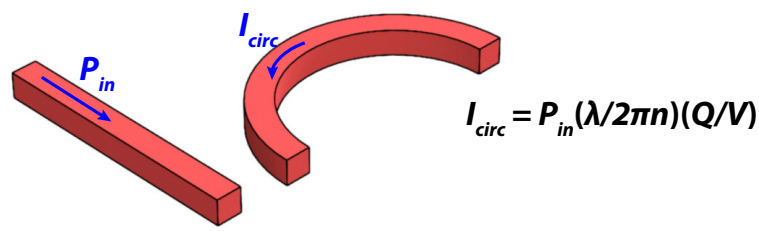

Fig. 1.6: An illustration of optical intensity enhancement using a microcavity side-coupled to a bus waveguide.

The third property of microcavity is the intensities enhancement inside the resonant cavity (shown in Fig. 1.6). As mentioned in Ref. [37], the circulating intensity (I_{circ}) in the microcavity is linked to the input power in the bus waveguide (P_{in}) as

$$I = P_{in}(\lambda/2\pi n)(Q/V) \tag{1.1}$$

where n is the index of the resonant mode. Therefore, even if the input power is relatively weak, the circulating intensity inside the cavity can be much higher, making it a proper platform for applications in both linear and nonlinear optics [37, 38, 39].

The last one is the power consumption reduction for electrically controlled integrated photonic devices such as modulators [3, 40, 7]. The switching energy for depletion-based pn-junction structures can be represented as $E_s = CV^2$ where C is the device capacitance, and V is the required bias voltage. Therefore, the decrease in voltage with resonance enhancement and reduction in the device capacitance as a result of compactness of the microcavity will dramatically reduce the power budget. An example of comparing the power consumptions of a microcavity-based and Mach-Zehnder-interferometer-based modulator is included in Appendix D.

1.3 Outline of this Thesis

This thesis focuses mostly on the first three properties of microcavities while the reduction in power consumption using a microcavity as a modulator has been rigorously investigated in Dr. Erman Timurdogan's thesis [41].

In Chapter 2, a new concept of a microcavity-based filter – the partial-drop filter is introduced. Based on the idea, a new architecture of wavelength-division-

multiplexing-compatible optical multicasting system is presented. The investigation focuses on the power uniformity, channel crosstalk, and high-speed data communication operations of the designed system. The results presented in this chapter were published in [28, 30, 42].

In Chapter 3, a waveguide-coupled resonant germanium-on-silicon detector is presented. Different aspects of the photodetector are investigated, with an emphasis on achieving high-speed operations and increasing the photo responsivities for longer wavelengths. The results presented in this chapter were submitted to Optics Letters.

In Chapter 4, a robust on-chip Al_2O_3 microcavity design and its applications in on-chip rare-earth-ion-based lasers are presented. The analysis of the microcavity design focuses on the dependence of intrinsic Q-factors on polarization, bending radius, wavelength, and deposited film thickness. Based on the cavity design, optically-pumped ytterbium and thulium lasers are designed and investigated. Part of the results presented in this chapter was published in [32, 43, 44] and the passive cavity analysis is in preparation for Optics Express.

In Chapter 5, a wafer-scale analysis of adiabatic microring resonators is presented. The design is investigated using both simulation tools and large quantities of devices fabricated on a 300mm wafer. In addition, Q-factors of this type cavity under contact insertion are also analyzed and optimized with rigorous 3D finite-difference time-domain simulations, providing a new insight into using adiabatic microring resonators as a general replacement to conventional microring resonators. The results presented in this chapter were published in [19].

CHAPTER 2

Optical Routing and Multicasting Systems

In this chapter, a new architecture of a WDM-compatible optical multicasting system is presented. First, the concept of a partial-drop filter was introduced and investigated using the coupled-mode-theory. The concept was then extended to a cascaded system to achieve an optical multicasting function while maintaining a wavelength selectivity. Based on the analysis, a 1-by-8 first-order microring-based multicasting system was designed and fabricated. Uniform responses and error-free data communication operations across all eight drop ports were achieved. Furthermore, to improve the roll-off speed of the filter-based structure to allow denser wavelength channel spacing for practical applications, higher-order filter-based multicast systems were studied and a 2nd-order filter-based system was demonstrated as an example.

2.1 Introduction

In on-chip communication networks, bus (or broadcast) topologies are among the most widely deployed, enabling all-to-all communications for rapid dissemination of instructions and data across a system. Recently, it has been proposed that wavelength selective all-to-all communications, with the transmit wavelength being tied to a particular core, offer a particularly compelling implementation for all-to-all on-chip networks [45]. In an integrated photonic platform, bus topologies can be implemented by cascaded power splitters [12] connected to multiprocessors. However, with simple power dividers, all wavelengths must be dropped at all sites along the network, limiting the potential network topologies. Importantly, a limitation of simple all-to-all topologies is that the optical power requirements scale with N^2, where N is the number of sites. As a result, for large-scale implementations, limited all-to-all topologies, where the information is shared among a select group of sites are often more attractive. In order to implement limited all-to-all communications networks, wavelength selective partial drops are required (see Fig. 2.1(a)) [46] with a select group of wavelengths. The most challenging component of the all-to-all communications network is shown in Fig. 2.1(b). The resonant detectors can be implemented by connecting drop ports of ring resonators to on- or off-chip detectors (DET) [inset of Fig. 2.1(b)], but are not essential for demonstrating the partial drop functionality. Thus, for the rest of the chapter, the broadcast network in Fig. 2.1(b) will be simplified to a parallel optical drop filter bank with off-chip detectors.

Previously, single large radius rings with multiple drop ports have also been utilized to act as a wavelength selective power divider [47]. However, the limited free spectral range (FSR) makes the approach incompatible with dense wavelength-division-multiplexed communications. To overcome these limitations, small-radius ring resonators are preferred to enable large FSRs and broad optical bandwidths in an on-chip network.

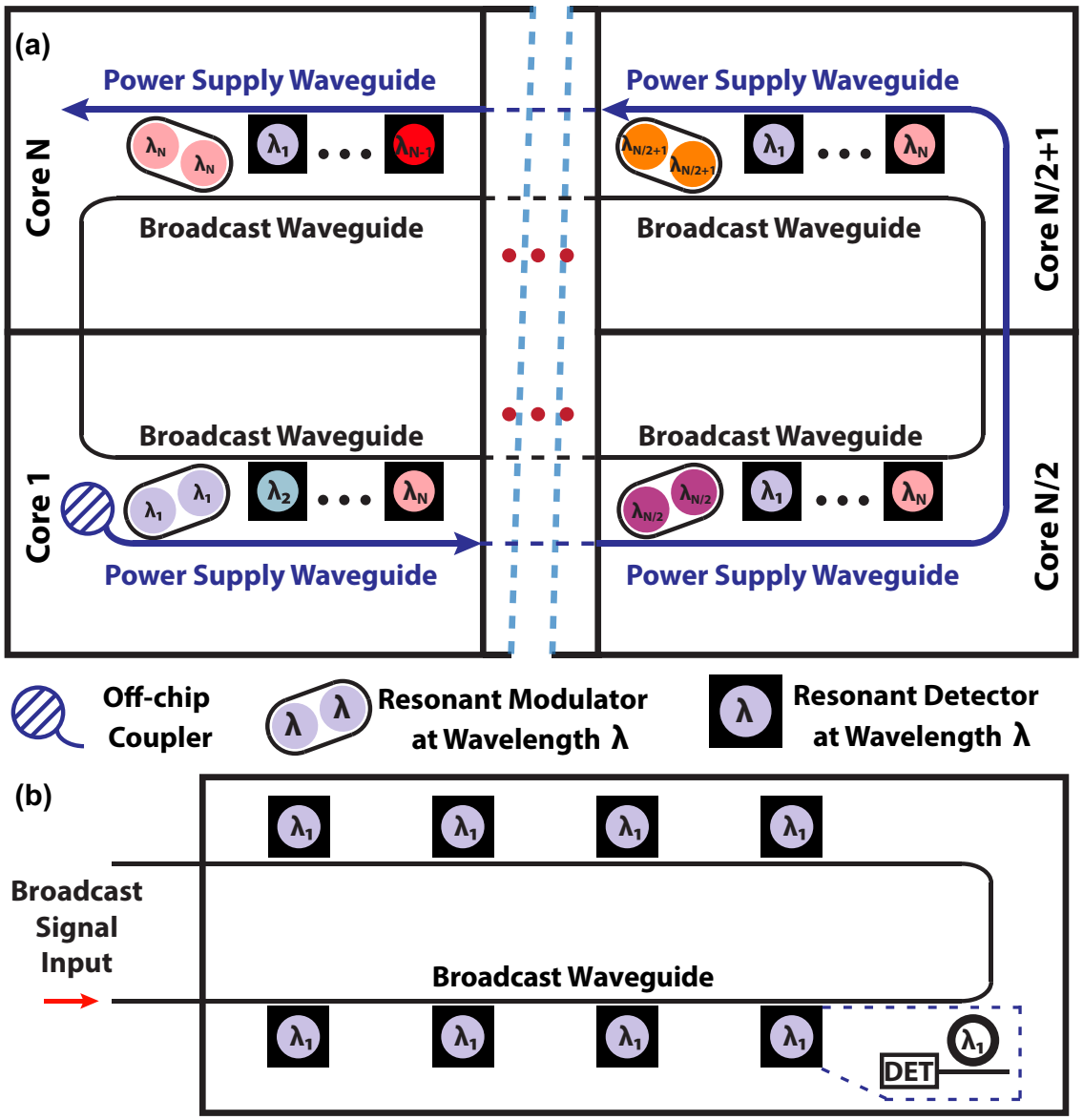

Fig. 2.1: (a) An example approach of using wavelength selective partial drop filters in an all-to-all communications network. (b) A simplified 1-by-8 on-chip broadcast network. Inset: Implementation of resonant detector at wavelength λ_1.

2.2 1st-Order Optical Multicasting System

2.2.1 Theory – Single Device

We started with the model of a 1st-order filter, shown in Fig. 2.2. It has two important parameters – gap1 and gap2. For an input with a broad wavelength range, wavelengths correspond to the resonances of the cavity will be selected and guided to

the drop port, featuring a Lorentzian response shape. For a conventional filter design, gap1 and gap2 are chosen to be the same when the loss inside the cavity is negligible. This way, all the power will be guided to the drop port when the input wavelength matches one of the resonances in the cavity. However, a full power selection is not desired for all applications. Applications such as broadcasting or multicasting, require a partial power delivery to the drop port.

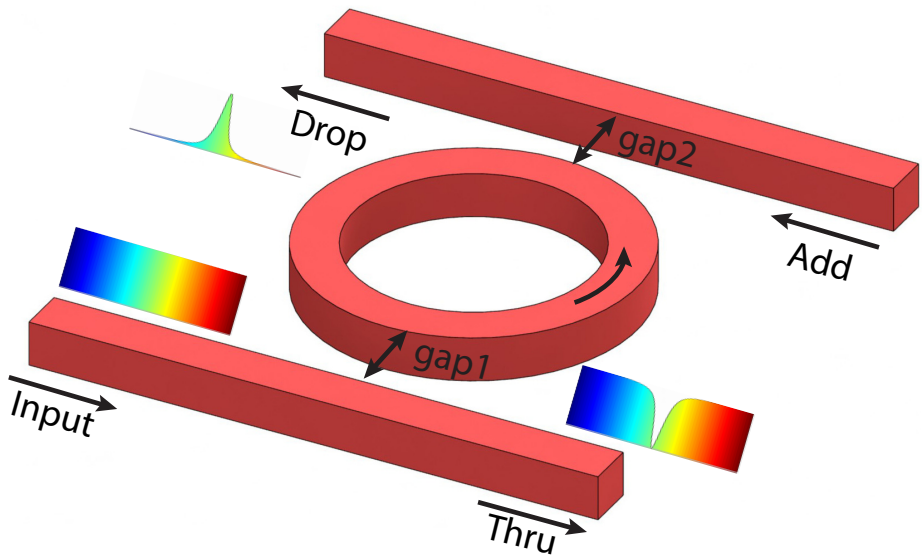

Fig. 2.2: A schematic of a single-ring-based filter.

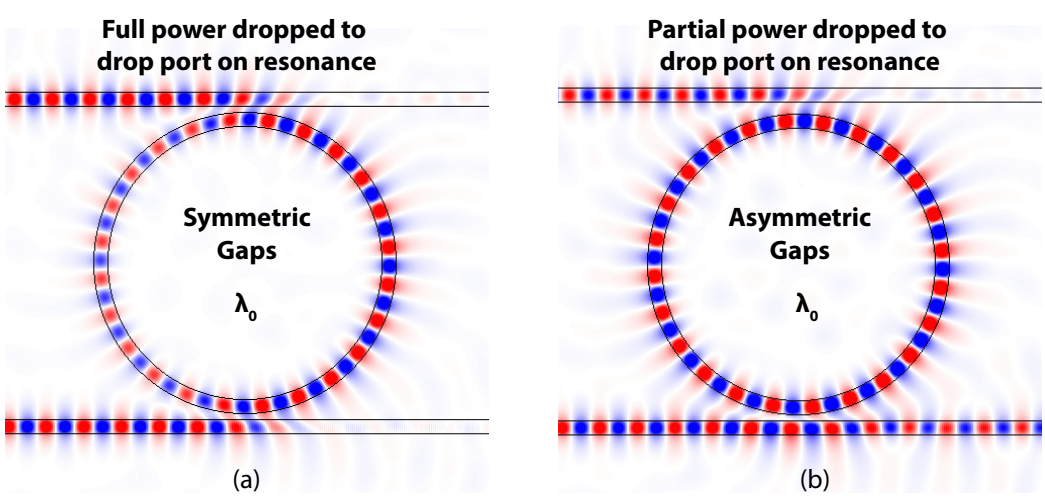

Fig. 2.3: 2D FDTD simulations of microring-based filters with (a) a symmetric coupling configuration and (b) an asymmetric coupling configuration.

A novel way to approach this problem is bringing asymmetry into the structure

by setting gap1 to be different from gap2. The adjustment of gap1 and gap2 would provide a freedom to adjust the selected power level and filter bandwidth. We define this type of structure as a **partial-drop filter**. We first tested this idea with a 2D finite-difference time-domain (FDTD) simulation. The simulation results for both symmetric and asymmetric coupling configurations are shown in Fig. 2.3 (the colors are saturated for a better contrast). We observe that all the power on resonance is guided to the drop port for the symmetric case while only a portion of the input power is collected by the drop port for the asymmetric case. The leftover power for the latter case still stays in the bus waveguide and will continue its propagation.

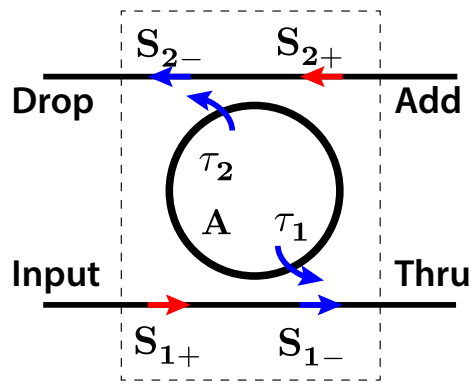

Fig. 2.4: A coupled-mode-theory (CMT) model of a microring filter.

The phenomenon can be well explained by the coupled-mode-theory (CMT) in the time domain [48]. The model is shown in Fig. 2.4. Assuming that the internal loss of the cavity is negligible compared to the coupling strength from the waveguide, the system, therefore, can be modeled by the following equations:

$$\frac{\mathrm{d}A}{\mathrm{d}T} = -i\omega_0 A - \sum_{l=1}^{2}(\frac{A}{\tau_l} + \sqrt{\frac{2}{\tau_l}}S_{l+}) \tag{2.1}$$

$$S_{l-} = -S_{l+} + \sqrt{\frac{2}{\tau_l}}A \tag{2.2}$$

The ω_0 represents the cavity resonant frequency; A is the energy amplitude of the cavity, which is normalized so that $|A|^2$ stands for the total energy stored in the cavity; and S is the wave amplitude, which is normalized so that $|S|^2$ represents the power. The $+$ and $-$ denote the input and output to the cavity, respectively. The time constant, τ, represents the amplitude decay time constant of the cavity due to

coupling to the bus or drop waveguide. For the single input case, S_{2+} is zero. Since A is the energy amplitude of the cavity, for an input frequency of ω, $\mathrm{d}A/\mathrm{d}T = -i\omega A$. Therefore, with simple mathematic derivations, we can achieve the thru and drop port frequency responses as

$$\textbf{Thru} = |\frac{S_{1-}}{S_{1+}}|^2 = \frac{(\omega_0 - \omega)^2 + (1/\tau_1 - 1/\tau_2)^2}{(\omega_0 - \omega)^2 + (1/\tau_1 + 1/\tau_2)^2} \tag{2.3}$$

$$\textbf{Drop} = |\frac{S_{2-}}{S_{1+}}|^2 = \frac{4/(\tau_1\tau_2)}{(\omega_0 - \omega)^2 + (1/\tau_1 + 1/\tau_2)^2} \tag{2.4}$$

When $\tau_1 \neq \tau_2$ and $\omega = \omega_0$, the drop port response (shown in Eqn. 2.4) gives a value that is lower than 1 while maintaining a Lorentzian filter shape across a broadband of spectrum.

2.2.2 Theory – Cascaded System

While a standalone partial-drop filter offers partial power selection with wavelength selectivity, it cannot be treated as a termination port in a network because of the leftover power propagating in the bus waveguide. To extend the single device into a systematic design to achieve multicasting function, here we utilize a cascade-type schematic (shown in Fig. 2.5). Compared to Fig. 2.4, Fig. 2.5 adds i to represent the stage number. With the cascading effect, we have one additional constraint

$$S^i_{1-} = S^{i+1}_{1+} \tag{2.5}$$

to connect the previous stage to the current stage.

Combining Eqn. 2.3, 2.4, and 2.5, we get the following conditions to achieve a uniform power splitting into N drop ports:

$$\tau_1^{i+1} \cdot \tau_2^{i+1} = \tau_1^i \cdot \tau_2^i \tag{2.6}$$

$$|\frac{1}{\tau_1^{i+1}} + \frac{1}{\tau_2^{i+1}}| = |\frac{1}{\tau_2^i} - \frac{1}{\tau_1^i}| \tag{2.7}$$

for $i = 1, ...N-1$. Assuming that the peak power at ω_0 for each port is $1/N$ of the total input power and the total decay time constant for the first stage is $\tau \equiv 1/(1/\tau_1^1 + 1/\tau_2^1)$

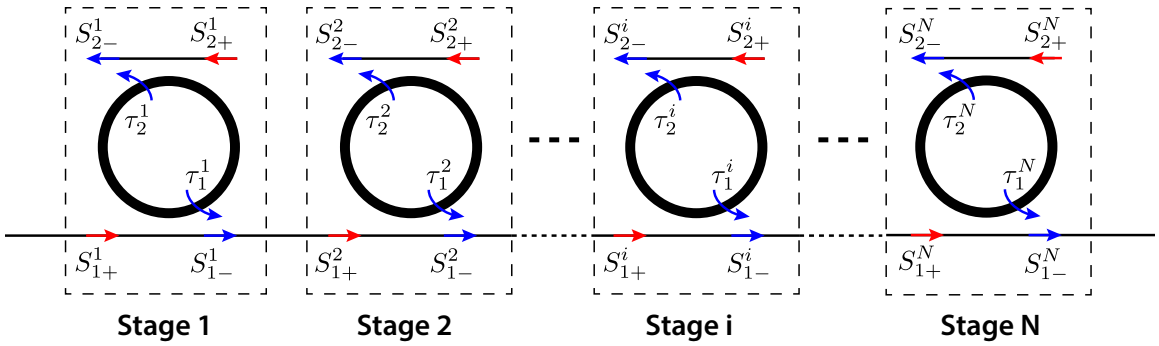

Fig. 2.5: A schematic of an N-stage ring-based cascaded partial-drop filter system. Each ring supports a circulating mode with energy amplitude A, incident wave amplitude S_{1+}, transmitted wave amplitude S_{1-}, drop port output wave amplitude S_{2-}, and input wave amplitude S_{2+}. τ denotes the amplitude decay time constant of each cavity due to the coupling to a separate waveguide.

where $\tau_1^1 > \tau_2^1$, we can get explicit expressions for τ_1^i and τ_2^i as

$$\tau_1^1 = 2[\sqrt{N(N-1)} + N]\tau \tag{2.8}$$

$$\tau_2^1 = \frac{\sqrt{N(N-1)} + N}{\sqrt{N(N-1)} + N - 1/2}\tau \tag{2.9}$$

$$\tau_1^{i+1} = 1/2[\tau_1^i - \tau_2^i + \sqrt{(\tau_1^i)^2 + (\tau_2^i)^2 - 6\tau_1^i\tau_2^i}] \tag{2.10}$$

$$\tau_2^{i+1} = 1/2[\tau_1^i - \tau_2^i - \sqrt{(\tau_1^i)^2 + (\tau_2^i)^2 - 6\tau_1^i\tau_2^i}] \tag{2.11}$$

for $i = 1, ...N-1$. With the constraints listed in Eqn. 2.8, 2.9, 2.10, and 2.11, all the drop port responses will be the same and can be represented by a Lorentzian frequency response function

$$|\frac{S_{2-}^i}{S_{1+}^i}|^2 = \frac{4/(\tau_1^1\tau_2^1)}{(\omega-\omega_0)^2 + (1/\tau)^2} \tag{2.12}$$

We notice that the function has a peak value of $1/N$ on resonance and a filter response bandwidth that depends only on the chosen τ value.

For practical design, we use dimensionless parameters such as Q-factors instead of decay time constants (τ). The relation between Q and τ is $Q = \omega_0\tau/2$. For an eight-stage system with a total Q-factor of the first stage of 2,000, the Q-factors for each stage from the theory are plotted in Fig. 2.6. We notice that the $1/N$ equipartition condition requires the ith stage to take $1/(N-i+1)$ of the optical power that is still left in the bus waveguide. In addition, to ensure the same bandwidth at each stage,

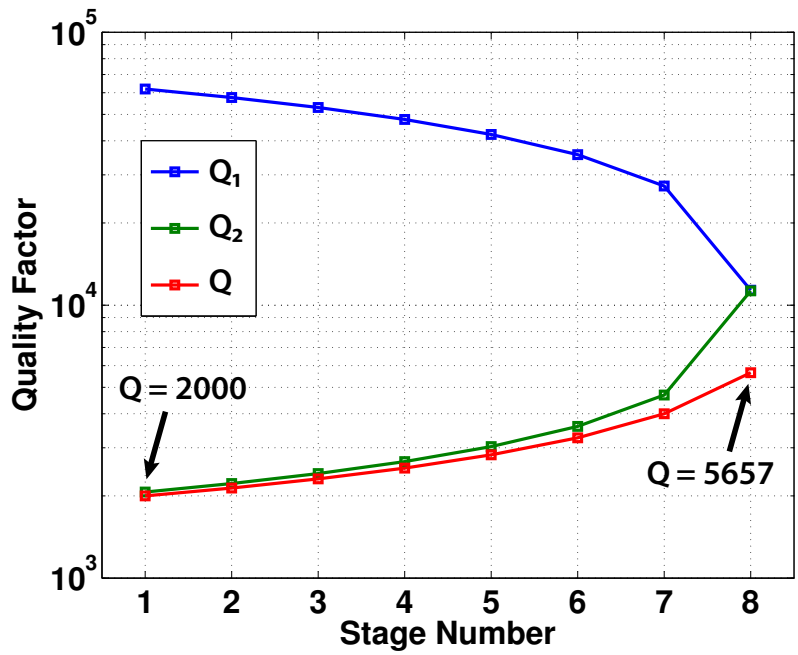

Fig. 2.6: Quality factors calculated from the coupled-mode-theory to maintain an equal power distribution in an eight-stage partial-drop filter bank.

Q-factors associated with the thru and drop ports must vary. This theoretical model can be easily extended to cases where the intrinsic loss of the cavity is not negligible by including a loss term τ_r in Eqn. 2.1 to represent the decay constant of energy in the cavity due to intrinsic loss such as radiation, material or fabrication loss.

2.2.3 Experimental Implementation

In order to demonstrate this system on a wafer-scale fabrication platform, we also need to consider fabrication errors, wafer variations [36] and coupling induced frequency shifts (CIFS) [49] of resonant devices. Therefore, a thermal tuning mechanism needs to be incorporated into the system. For the rest of this chapter, we will utilize an adiabatic microring resonator design to add an efficient wavelength tunability to the resonators used in the system. Details of the adiabatic microring resonators design are discussed in Chap. 5.

The schematic of a 3-μm-radius tunable adiabatic microring resonator is shown in Fig. 2.7(a). Integrated heaters are introduced by a p-type doping to the silicon at a concentration of 1×10^{18} cm^{-3} in the adiabatic ring waveguide, and contacts are

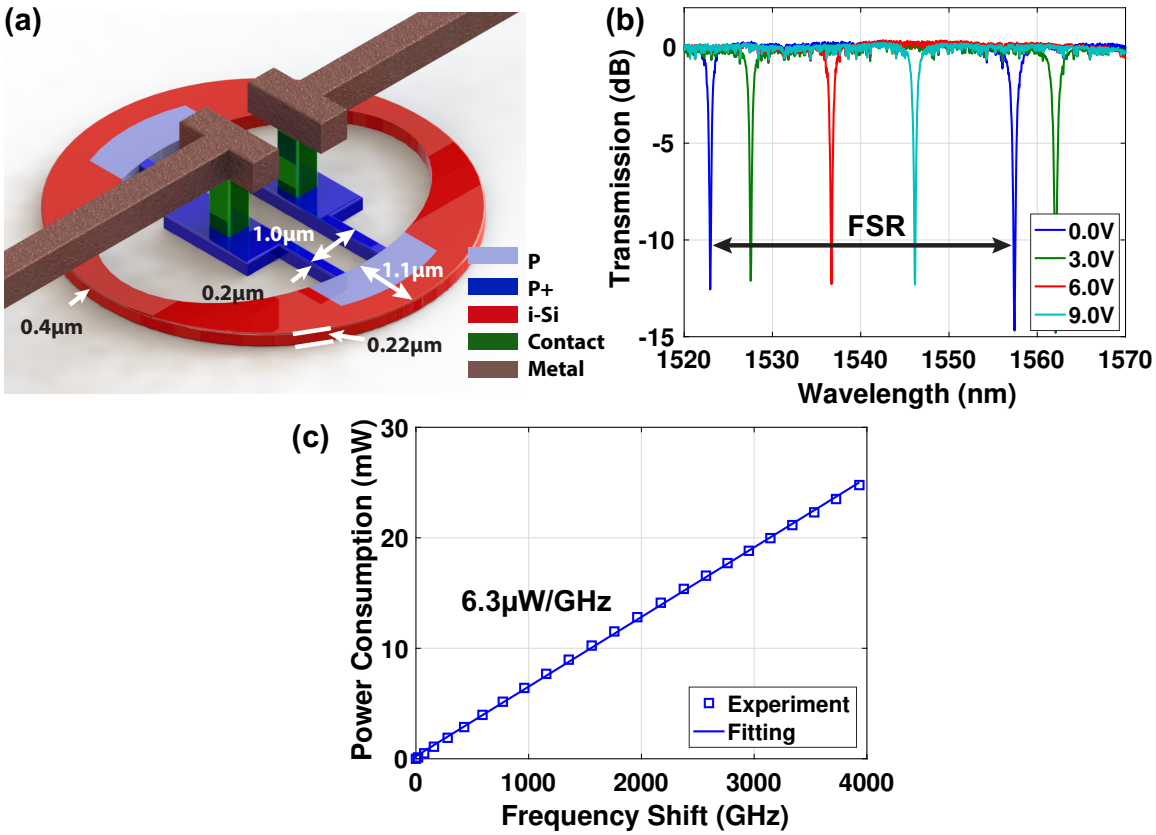

Fig. 2.7: (a) A schematic of a tunable adiabatic microring resonator. (b) The transmission spectra of a 3μm-radius adiabatic microring resonator under different bias voltages, showing a clean free-spectra-range (FSR). (c) Power consumption of the integrated heater vs. resonant frequency shift, showing a thermal tuning efficiency of 6.3μW/GHz.

connected to the heaters by small tethers of silicon with a p+ doping at a concentration of 1×10^{20} cm^{-3}. The microring width is adiabatically broadened from 0.4μm to 1.1μm to minimize the loss introduced by the insertion of an integrated heater. The transmission spectra of the tunable adiabatic microring resonator under different bias voltages are shown in Fig. 2.7(b), demonstrating an uncorrupted free-spectral-range of over 34nm. The tuning efficiency curve of the adiabatic microring resonator is shown in Fig. 2.7(c). We observed a tuning efficiency of 6.3μW/GHz, a little bit lower than the previous demonstration in Ref. [50]. The decrease in efficiency is mostly due to the simplification of the tether design in connection to the microcavity, resulting in a less optimized design in thermal management.

Coupling coefficients from the bus waveguide to the microcavity can be calculated

using finite-difference-time-domain (FDTD) simulations. The coefficients can then be converted to the quality factors using the following relation:

$$Q = \frac{2\pi\omega_0}{\kappa^2 \cdot FSR(\omega)} \tag{2.13}$$

where κ^2 represents the coupling coefficient, ω_0 denotes the resonant angular frequency, and $FSR(\omega)$ stands for the free-spectral-range of the resonator measured in angular frequency.

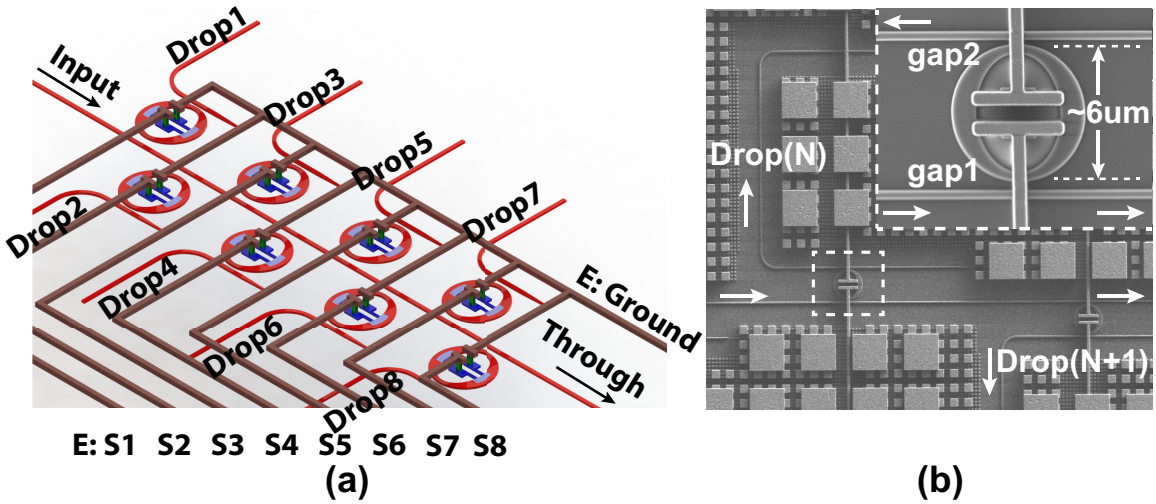

Fig. 2.8: (a) A schematic of the optical multicast system. All the microrings shown in the figure have the same resonant frequency with different couplings to the bus and drop waveguide. (b) A scanning electron micrograph (SEM) of the fabricated device. Inset: a close-up view of the fabricated tunable adiabatic microring filter.

A schematic of a 1-by-8 optical multicast system is shown in Fig. 2.8(a). We fabricated the design in CNSE, SUNY Polytechnic Institute at Albany. The SEM of the fabricated device after dry etching to remove the top SiO_2 cladding is shown in Fig. 2.8(b).

For the experiment, we first took the transmission spectra of the thru port and all of the drop ports. The transmission spectra of the untuned system is shown in Fig. 2.9(a). We noticed that the resonances of all the resonators are different from each other, making it harder to tell whether the structure was correctly fabricated. In order to compensate the variations, we applied power to the integrated heaters and started aligning all the resonances to the same wavelength of 1554nm. A list

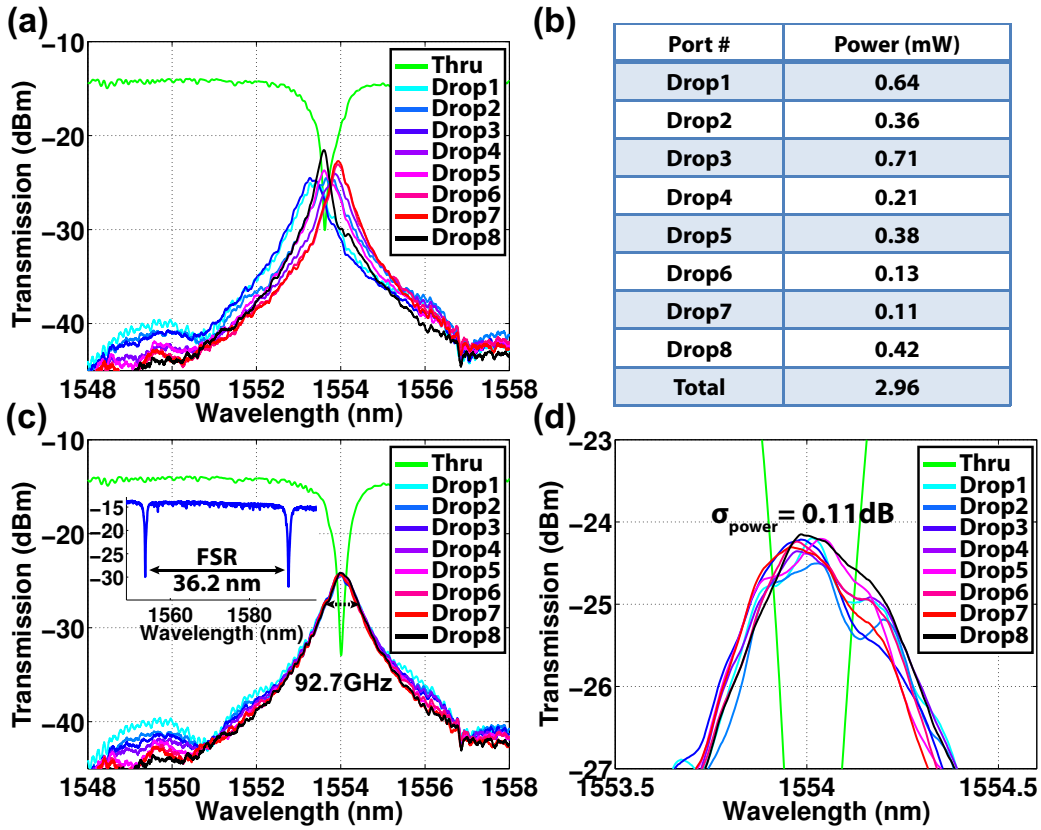

Port #	Power (mW)
Drop1	0.64
Drop2	0.36
Drop3	0.71
Drop4	0.21
Drop5	0.38
Drop6	0.13
Drop7	0.11
Drop8	0.42
Total	2.96

Fig. 2.9: (a) Transmission spectra of the 1-by-8 multicasting system before thermal tuning. (b) Tuning power of each drop port. (c) Transmission spectra of the multicasting system after thermal tuning. Inset: spectral response of the device showing an uncorrupted 36.2nm free-spectral-range. (d) Close-up view of the transmission spectra of the multicasting system after thermal tuning, showing a power variation of 0.11dB on resonance with 2.96mW total tuning power.

of the tuning power for the rings of each stage is shown in Fig. 2.9(b). With the thermal tuning, the transmission spectra of those stages were aligned closely with each other (shown in Fig. 2.9(c)). The average 3dB bandwidth of the drop port responses is 92.7GHz, making this type of device capable of handling high-speed data traffic. The resulting broad range scan of the thru port is shown in the inset of the Fig. 2.9(c), showing an uncorrupted FSR of 36.2nm. The large FSR demonstrated makes it possible to allow the coexistence of more frequency channels with less mutual interference or crosstalk. A zoom-in of the top part of the transmission spectra is shown in Fig. 2.9(d), revealing a resonance variation as low as 1.7GHz and a power variation of less than 0.11dB on resonance, which are small enough to ensure equal

power distributions among all drop ports. Although in this system, eight rings and heaters are used, the total loss of the structure is only 1.1dB – no worse than that for a single fully coupled filter, a result that makes sense given that, in aggregate, the coupling of the eight-way power splitter equates to the coupling of a single fully coupled ring resonator.

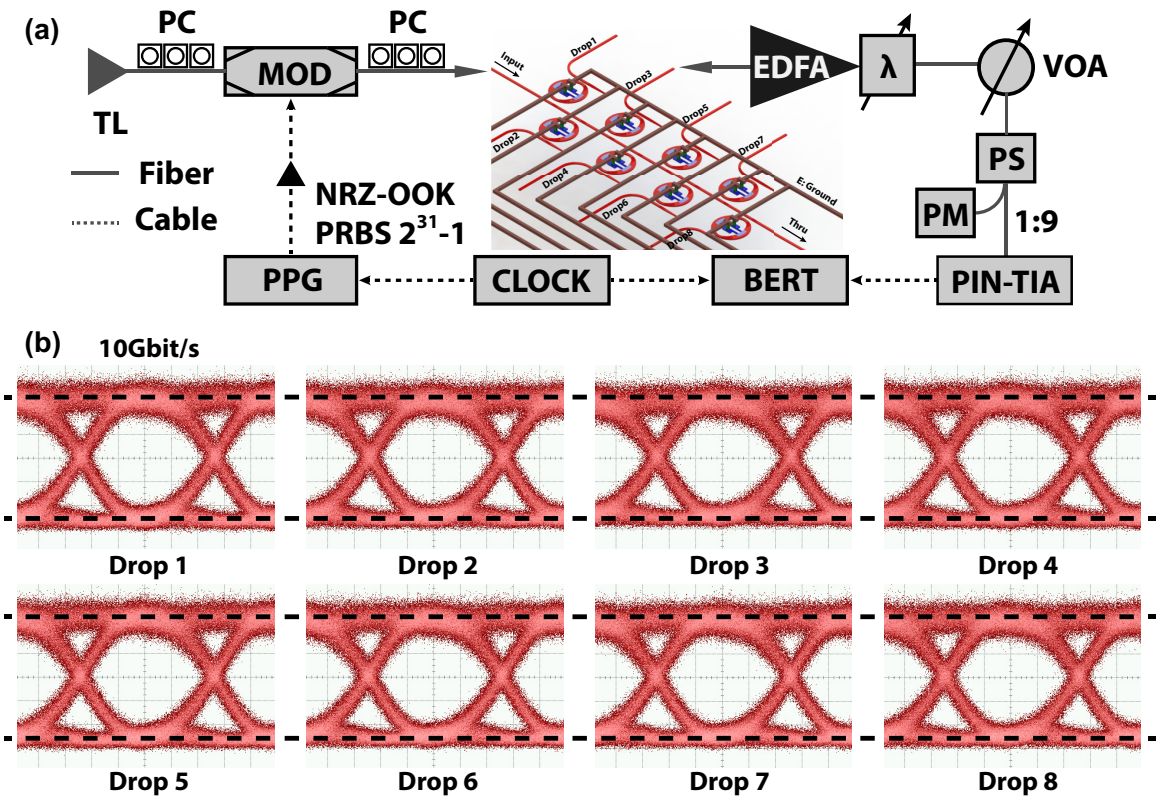

Fig. 2.10: (a) A diagram of the experimental setup for characterizing the data transmission performance. (b) Eye-diagrams for drop ports 1 to 8 with 10Gbit/s data rate generated from external commercial $LiNbO_3$ modulator with input laser wavelength at 1554nm.

This parallel-drop filter bank allows for high-speed data to be transmitted to all eight drop-ports with equal power distributions. A diagram of the experimental setup used to characterize the filter bank performance is depicted in Fig. 2.10(a). A continuous-wave tunable laser source (TL) was first coupled into a single mode fiber. The light was then transmitted through a commercial lithium niobate ($LiNbO_3$) modulator with polarization controllers (PCs) before and after the modulator to align the polarization to the transverse electric (TE) waveguide mode. In this work, the data was coded with non-return-to-zero (NRZ) on-off-keying (OOK) using a pulse

pattern generator (PPG) with a 2^{31}-1 pseudo-random bit sequence (PRBS). The modulated light was then coupled onto the silicon chip. By thermally tuning the rings, all of the resonant frequencies were aligned to the same wavelength. For the input, the light of the tunable laser was spectrally aligned to the resonant wavelength to drop the signal to each drop port. Off-chip, the modulated optical signal was then passed through an erbium-doped fiber amplifier (EDFA), a fiber-based tunable grating filter (λ) with a 1-nm 3dB bandwidth, and a variable optical attenuator (VOA). A 1:9 power splitter (PS) was used after the VOA to direct 10% of the total power to a power meter for monitoring while transmitting the rest (90%) power to a high-speed (10Gbit/s) PIN photodiode and transimpedence amplifier (PIN-TIA) receiver. The signal was then evaluated using a bit-error-rate (BER) tester (BERT). Both the PPG and the BERT were synchronized to the same clock.

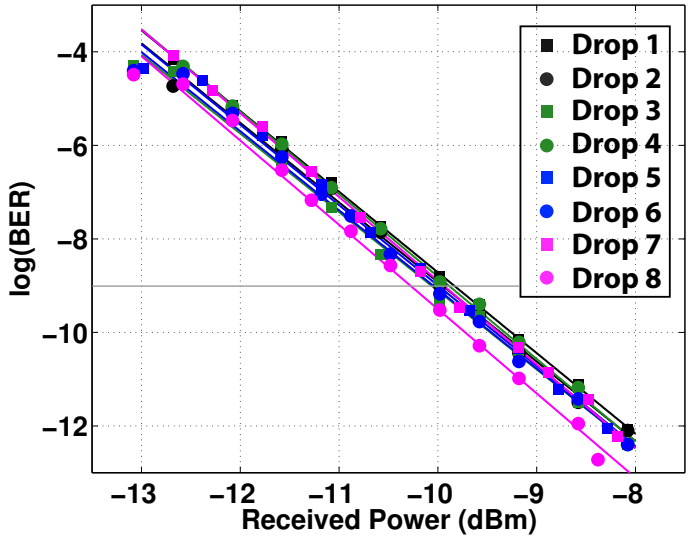

Fig. 2.11: Experimentally measured bit-error-rate (BER) curves for the partial drop broadcast system for each drop port with a 10Gbit/s data rate generated from an external commercial $LiNbO_3$ modulator.

Fig. 2.10(b) shows the obtained eye-diagrams for all drop ports with 10Gbit/s data rate. The resulting diagrams are equally open. We then took BER curves and measured power penalties for each port using the 10Gbit/s data rate to quantify the differences between each transmission [shown in Fig. 2.11]. For each BER curve, we also verified error-free operation, achieving BERs below 10^{-12}. The BER curves val-

idate our initial observations about power uniformity across channels, showing a less than 0.5dB power penalty difference among the eight channels. Though the device demonstrated has slow roll-off with first-order filter responses, limiting the frequency channel spacing for WDM applications, with the help of high order filter designs [33], the same technique developed here can be readily applied to a narrower bandwidth parallel drop filter bank for dense wavelength division multiplexed (DWDM) applications.

2.2.4 Conclusion

In this section, a theoretical framework for a 1-by-N-port first-order ring-based optical multicast system is analyzed. With the developed theory, a 1-by-8 wavelength-selective optical multicast system is demonstrated using eight partial-drop tunable adiabatic microring filters. The multicast system shows a low power variation (0.11dB) among all of the outputs and a small excess loss of 1.1dB in aggregate. Error-free operations for 10Gbit/s data rates are achieved for all the eight drop ports, with less than 0.5dB power penalty difference among those ports. The wavelength selectivity and large FSR (36.2nm) enabled by small-radius microrings offer a promising solution to achieving WDM optical broadcasting networks and high-sensitivity receivers.

2.3 Unicast and Multicast Network in a Ring-Based Photonic System

With the partial-drop filter concept introduced in the previous section, a more complex on-chip optical system can be implemented. The ring-based structures have a significant advantage over non-resonant devices – the wavelength division multiplexing (WDM)-compatibility. The capacity of a ring-based network can be easily extended to a larger capacitance by increasing the numbers of frequency channels to carry more data. Two primary functions – unicast and multicast, are important in a data transmission system. Before the emergence of the idea of the partial-drop filter, ring-based filters could easily handle the unicast function since a full-drop filter will direct the information to a preallocated destination. However, getting a multicast function into the ring-based network is relatively difficult without interfering unicast functions. While a photonic multicast network has been demonstrated before using

four-wave-mixing (FWM), where a modulated signal at pump wavelength is replicated into signals carried by multiple optical wavelengths (i.e. frequency channels) [51], the nonlinear nature and high optical intensity constraint of FWM limited the implementation of this technique in large-scale networks. In this section, we will focus on using both full-drop and partial-drop filters to combine unicast and multicast functions within a same ring-based network.

2.3.1 Device Schematic

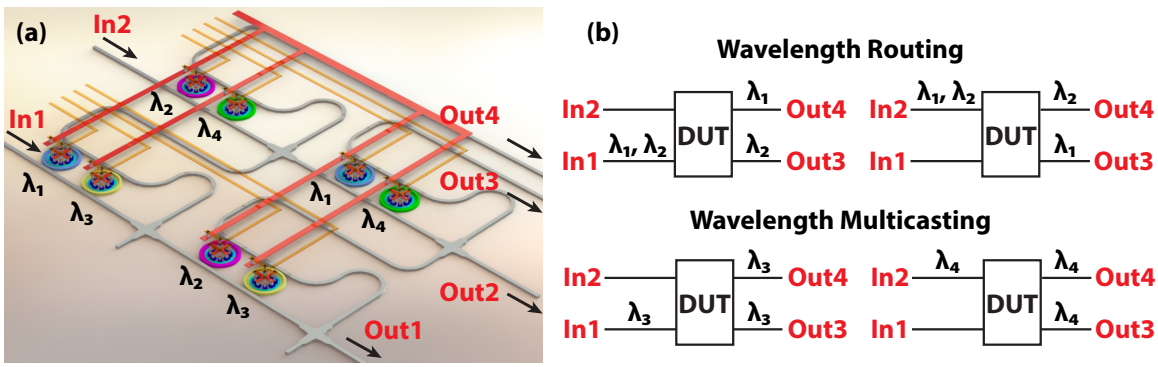

Fig. 2.12: (a) A schematic of the ring-based wavelength unicast and multicast network. The wavelengths (λ_1 to λ_4) on the side of the rings denote the resonances of the corresponding microring resonators. (b) An illustration of the functions of the system.

The schematic of the wavelength routing and multicasting network is shown in Fig. 2.12(a) and its corresponding functions are illustrated in Fig. 2.12(b). It consists of two input ports and four output ports (two thru ports and two drop ports). In the schematic, λ_1 and λ_2 denote conventional ring filters with the same coupling gaps to bus and drop waveguides where the channel-dropping functions (uni-casting) are performed. As a result, information encoded in a different wavelength to the same input port will be routed to a different output port (Out3 or Out4 ports). Different from the full-dropping functions of λ_1 and λ_2 filters, partial-drop functions are utilized in λ_3 and λ_4 filters. Therefore, in the network, information carried by λ_3 from input-1 (In1) and λ_4 from input-2 (In2) will be multicasted to both drop ports. In total, only one wavelength channel is occupied for multicasting purposes for each input port.

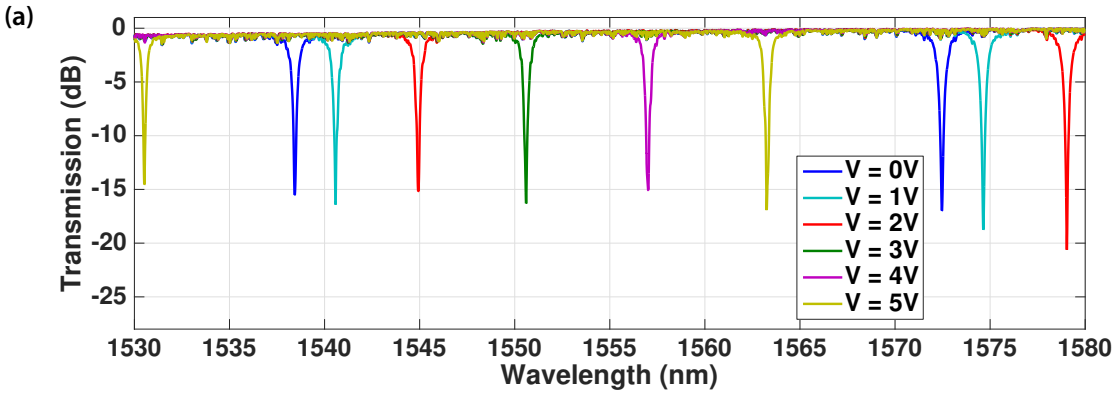

(b)

Voltage (V)	Current (mA)	Power (mW)	Shift (GHz)	Resistance (kΩ)
0	0	0	0	N.A.
1	0.44	0.44	47.4	2.27
2	1.44	2.88	318.3	1.39
3	2.55	7.65	866.1	1.18
4	3.42	13.68	1575.3	1.17
5	4.057	20.285	2372.8	1.23

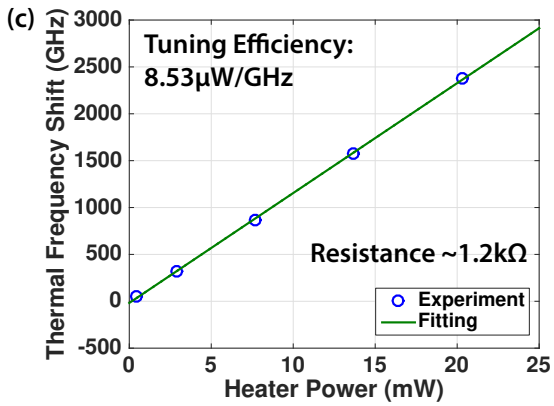

Fig. 2.13: (a) Transmission spectra of the tunable interior-ridge microring resonator with different applied voltages. (b) Tuning power, frequency shift and device resistance for various applied voltages. (c) Thermal frequency shift vs. thermal tuning power.

2.3.2 Device Characterization

We fabricated the design using the same fabrication process described in Sec. 2.2.3. The interior ridge microring combined with a 400nm wide bus waveguide ensures a single-mode coupling into the microring resonators [24]. The thru port responses of the tunable microring resonator with different tuning voltages are shown in Fig. 2.13(a). Detailed information on current, power, frequency shift and device resistance is listed in Fig. 2.13(b). We observe that the device resistance is varying while the resistance becomes more stable with higher voltages, converging to a resistance value of ∼1.2kΩ. The relation between the resonant frequency shift and the applied heater power is plotted in Fig. 2.13(c), showing a tuning efficiency of 8.53μW/GHz.

In total, eight tunable ring filters were utilized in this network. Each ring has a tuning efficiency of ∼8.25 μW/GHz. The transmission spectra of the system af-

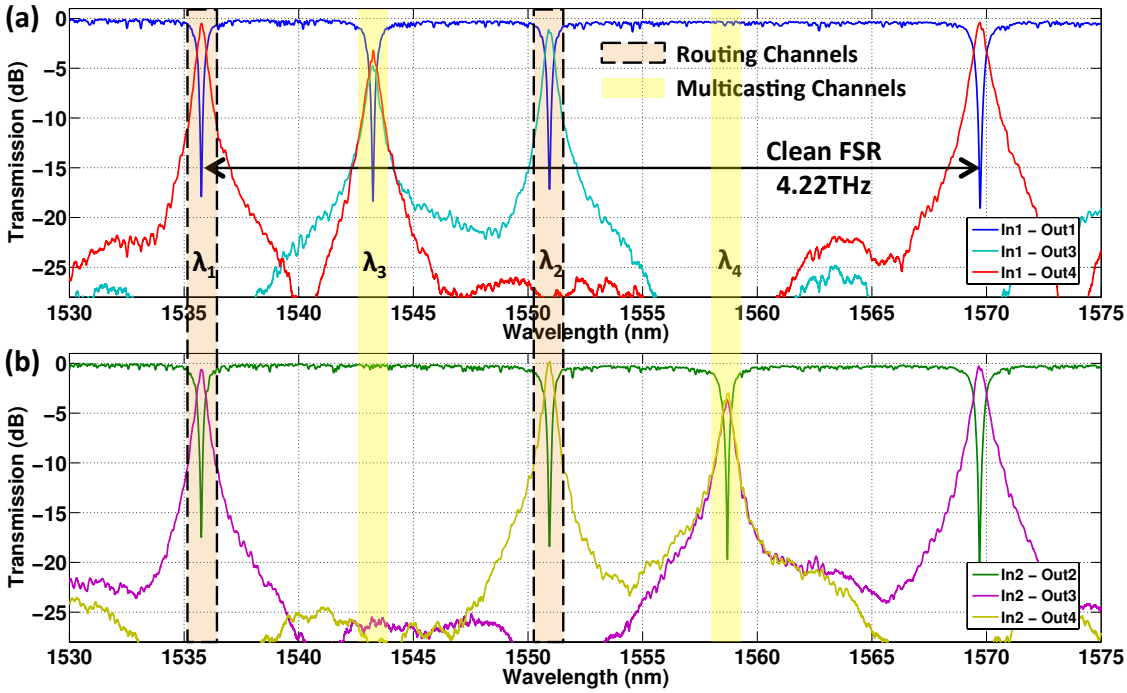

Fig. 2.14: (a) Transmission spectra of In1 to output ports 1, 3 and 4. (b) Transmission spectra of In2 to output ports 2, 3 and 4.

ter thermal tuning are shown in Fig. 2.14(a) and (b). A broad and uncorrupt FSR of 4.22THz and four well-separated wavelength channels (marked in Fig. 2.14) are demonstrated. We also observe that the received powers of the multicasting wavelengths channels (λ_3 and λ_4) are ~3dB less than the routing wavelength channels (λ_1 and λ_2). The decrease in the received power is related to the multicasting function where the total input power is uniformly divided between the two output ports. The full-width-half-maximum (FWHM) of tunable partial- and full-drop filters were 54GHz and 62GHz, respectively. The FWHM is targeted to achieve almost no insertion loss (<0.1dB) per tunable filter [24]. The total tuning power for compensating wafer-scale variations and aligning the resonant wavelengths of eight microring filters is aggregated to be 0.5mW, which can be further reduced by utilizing a more fabrication-tolerant design [19]. The wavelength crossings demonstrated in Ref. [12], are utilized in the network. Less than 1dB power difference is observed due to different aggregated losses of waveguide crossings along each path.

With microring technologies, high-speed data can be transmitted through the de-

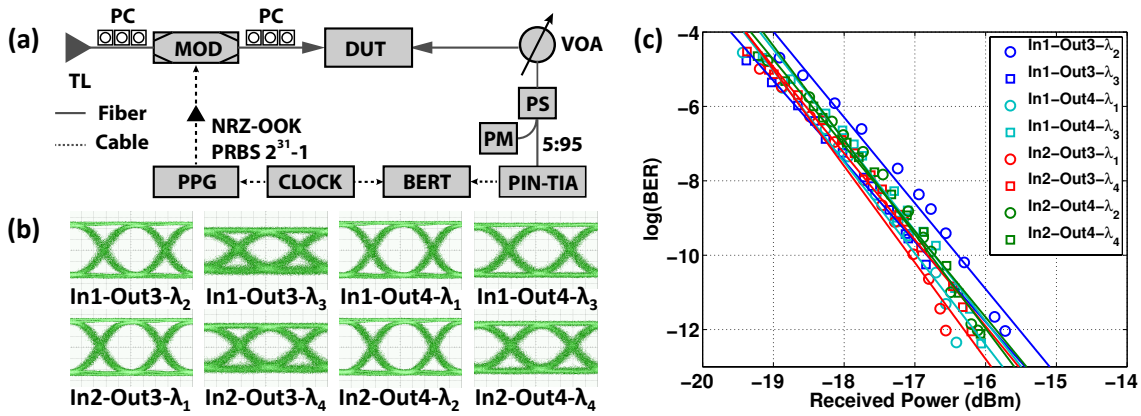

Fig. 2.15: (a) A schematic of the high-speed data transmission measurement system. (b) Eye diagrams of different routing/multicasting function of the designed network. (c) Experimentally measured bit-error-rate (BER) curves for all configurations of the developed system with 10Gbit/s data rates generated from an external commercial $LiNbO_3$ modulator.

vice. The setup shown in Fig. 2.15(a) was used to test the wavelength routing and multicasting functions of the device. A continuous-wave tunable laser (TL) source was first coupled into a single-mode-fiber. The light was then transmitted through a commercial lithium niobate ($LiNbO_3$) modulator with polarization controllers (PCs) before and after the modulator to align the input polarization to the on-chip transverse-electric (TE) waveguide mode. The modulator was encoded with non-return-to-zero (NRZ) on-off keying (OOK) pseudo-random bit sequence (PRBS) using a pulse pattern generator (PPG) with a pattern length of 2^{31}-1. The output from the chip was then transmitted to a 5/95 power splitter and went through the variable optical attenuator before being received by the PIN-TIA (Trans-Impedance-Amplifier) detector with a limiting amplifier. The signal was evaluated using a Bit-Error-Rate tester (BERT). Both the PPG and BERT were synchronized to the clock synthesizer.

Fig. 2.15(b) shows the eye diagrams of 10Gbit/s data rate for both wavelength routing (λ_1 and λ_2) and multicasting (λ_3 and λ_4) functions. In both cases, clear and open eye diagrams were observed, and the designed functionalities were achieved. We then took the BER curves and measured the power penalty of the individual functions for 10Gbit/s data rate. The BER curves for the overall network performance are shown in Fig. 2.15(c). The power penalty differences among all the functions

are less than 0.8dB, indicating an insignificant degradation of the signal integrity bypassing the whole network. Though the system shown here only shows a two-wavelength routing and a two-wavelength multicasting in a two-by-two cross-grid waveguide structure, by increasing the number of rings and utilizing higher-order filter designs, a more complex network consisting of more wavelength channels for both unicast and multicast functions can readily be achieved.

2.3.3 Conclusion

In this section, we presented a design using both full-drop and partial-drop filters to combine the unicast and multicast functions together in one system. The total thermal tuning power is 0.5mW, and the network shows less than 0.8dB power penalty at a BER of 1×10^{-9} among all the designed functions. The flexibility of the cross-grid waveguide system and the easy extension of the ring-based resonator structure to a large number of wavelength channels make it a viable solution for on-chip communication networks.

2.4 2nd-Order Optical Multicasting System

As we have discussed in previous sections, first-order filters provide an excellent way to demonstrate prototype device in silicon photonics. However, as shown in Eqn. 2.4, first-order filters have a Lorentzian-shape drop port response, which suffers a slow roll-off speed. If a first-order filter-based device is used in a practical wavelength-division-multiplexing system, it will introduce a significant amount of channel crosstalk when channel spacings get tighter. As a result, their applications in data- or tele-com communications are substantially limited.

A high-order filter-based system can solve this problem. Fig.2.16 shows frequency responses of drop ports of different orders of ring-based filters with respect to a frequency offset normalized to 3dB bandwidth. We can see that with the same 3dB bandwidth, by using high-order filter designs, the roll-off speed can be significantly increased. While a first-order filter has a relatively high channel crosstalk, a 2nd-order filter can achieve lower than -30dB crosstalk efficiently with only 3× of its bandwidth as the channel spacing. However, though high-order filters provide better

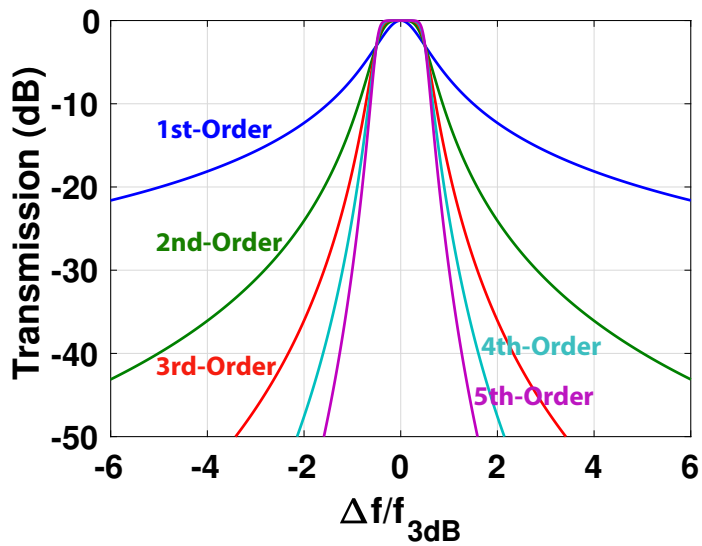

Fig. 2.16: Frequency responses of drop ports of different orders of ring-based filters with frequency offset normalized to 3dB bandwidth based on the coupled-mode-theory theory.

performance, the designs of high-order filters, especially for using them in multicast system designs, become more complex.

2.4.1 Theory – Single Device

We start the design with a coupled-mode-theory model (shown in Fig. 2.17) of a second-order filter. Here we use the notation system defined in [33] for convenience. The system can be modeled with the following equations:

$$\frac{\mathrm{d}}{\mathrm{d}t}a_1 = (j\omega_0 - \frac{1}{\tau_1})a_1 - j\mu a_2 - j\sqrt{\frac{2}{\tau_1}}S_i \tag{2.14}$$

$$\frac{\mathrm{d}}{\mathrm{d}t}a_2 = (j\omega_0 - \frac{1}{\tau_2})a_2 - j\mu a_1 \tag{2.15}$$

$$S_t = S_i - j\sqrt{\frac{2}{\tau_1}}a_1 \tag{2.16}$$

$$S_d = -j\sqrt{\frac{2}{\tau_2}}a_2 \tag{2.17}$$

where τ_1 is related to the coupling strength on the bus waveguide side while τ_2 is related to the coupling strength on the drop port side. The ω_0 is the cavity resonant frequency; a represents the energy amplitude of the cavity, which is normalized so that $|a|^2$ represents the total energy stored in the cavity; and S is the wave amplitude, which is normalized so that $|S|^2$ represents the power. The subscript i, t and d stand

for input, thru and drop port, respectively.

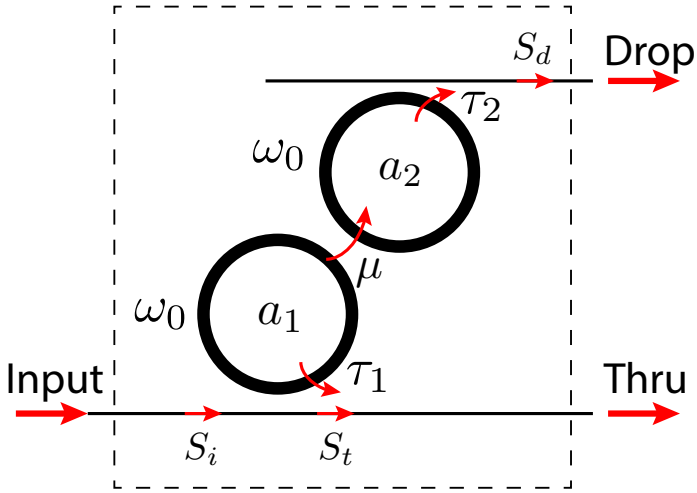

Fig. 2.17: A schematic of the CMT model of a second-order filter.

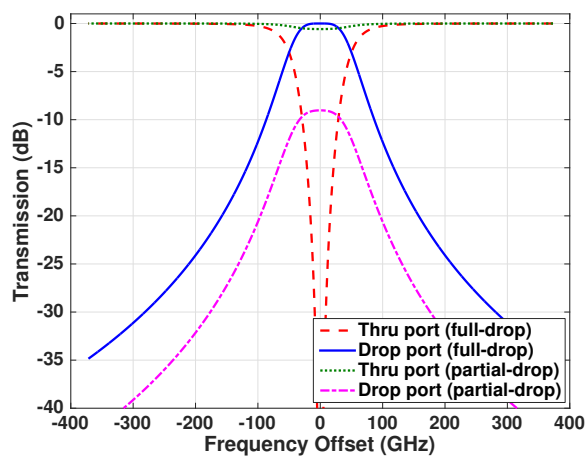

Fig. 2.18: Simulated transmission spectra of thru ports and drop ports for both a lossless full-drop filter and a partial-drop filter with the same FWHM bandwidth and 1/8 power splitting ratio on resonance.

Through mathematic computations, we can get the response of the thru and drop ports as

$$t = \frac{S_t}{S_i} = \frac{j\Delta\omega - \frac{1}{\tau_1} + \frac{\mu^2}{j\Delta\omega + \frac{1}{\tau_2}}}{(j\Delta\omega + \frac{1}{\tau_1} + \frac{\mu^2}{j\Delta\omega + \frac{1}{\tau_2}})} \tag{2.18}$$

$$d = \frac{S_d}{S_i} = \frac{j\mu\sqrt{\frac{2}{\tau_1}}\sqrt{\frac{2}{\tau_2}}}{(j\Delta\omega + \frac{1}{\tau_1} + \frac{\mu^2}{j\Delta\omega + \frac{1}{\tau_2}})(j\Delta\omega + \frac{1}{\tau_2})} \tag{2.19}$$

where $\Delta\omega = \omega - \omega_0$, $|t|^2$ and $|d|^2$ represent the power spectra of the thru and drop ports respectively. From the equation, we can see that by bringing τ_1 and τ_2 to be unequal, a partial power delivery is possible. Here we show a comparison between a second-order full-drop filter and partial-drop filter in Fig. 2.18. We observe that a Butterworth or maximally flat-top filter response can be achieved while having a partial power delivery.

To further calculate the conditions for the Butterworth or flat-top response mathematically, we define a power loss ratio using the similar definition in [33]:

$$\begin{aligned} P_{LR}(\Delta\omega) &\equiv \frac{|S_i|^2}{|S_d|^2} \\ &= P_0 + P_N(\Delta\omega^2) \end{aligned} \tag{2.20}$$

where P_0 represents a function irrelevant to $\Delta\omega$. $P_{LR}(\Delta\omega)$ is a polynomial function of $\Delta\omega^2$. A maximally flat filter response requires the coefficients of all orders of $\Delta\omega^2$ to vanish except for the highest. Therefore, for a second-order filter, $P_N(\Delta\omega^2)$ will be proportional to $\Delta\omega^4$. $P_{LR}(\Delta\omega)$ can be calculated as

$$P_{LR}(\Delta\omega) = \frac{(\frac{1}{\tau_1\tau_2} + \mu^2)^2}{\mu^2\frac{4}{\tau_1\tau_2}} + \frac{\Delta\omega^4 + (\frac{1}{\tau_1^2} + \frac{1}{\tau_2^2} - 2\mu^2)\Delta\omega^2}{\mu^2\frac{4}{\tau_1\tau_2}} \tag{2.21}$$

Therefore, a maximally flat response requires

$$2\mu^2 = \frac{1}{\tau_1^2} + \frac{1}{\tau_2^2} \tag{2.22}$$

and the corresponding drop port power on resonance is

$$\text{Drop}(\Delta\omega = 0) = \frac{\mu^2\frac{4}{\tau_1\tau_2}}{(\frac{1}{\tau_1\tau_2} + \mu^2)^2} \tag{2.23}$$

With the constraint in Eqn. 2.22, the full-width-half-maximum FWHM(dω) of the filter can be represented as

$$\begin{aligned} \mathrm{d}\omega &= 2\sqrt{\frac{1}{\tau_1\tau_2} + \mu^2} \\ &= \sqrt{2}(\frac{1}{\tau_1} + \frac{1}{\tau_2}) \end{aligned} \tag{2.24}$$

2.4.2 Theory – Cascaded System

To make use of the second-order partial-drop filter design developed in the previous section, we cascade the partial-drop filters into a multicasting system. A schematic

of the multicasting system is shown in Fig. 2.19. The numbers in the square brackets denote the stage numbers.

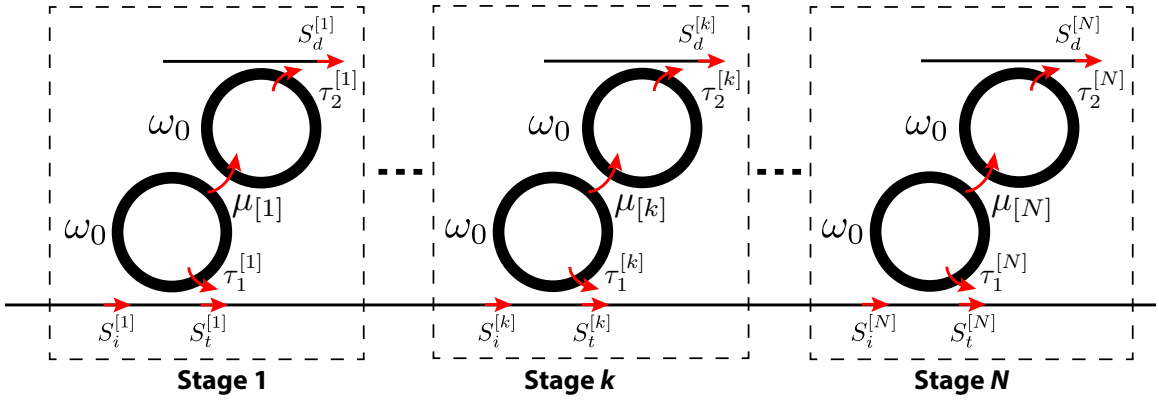

Fig. 2.19: A schematic of an N-stage second-order ring-based multicasting system.

We define the transfer functions for thru and drop ports of each stage as

$$\text{thru: } t^{[k]} = \frac{S_t^{[k]}}{S_i^{[k]}} \tag{2.25}$$

$$\text{drop: } d^{[k]} = \frac{S_d^{[k]}}{S_i^{[k]}} \tag{2.26}$$

for $k = 1,...N$.

To have the same response for all the drop ports, we need to satisfy the following condition:

$$|t^{[k]} \cdot d^{[k+1]}|^2 = |d^{[k]}|^2 \tag{2.27}$$

for $k = 1,...N$-1. Combining Eqn. 2.27, 2.18, and 2.19, we arrive at three specific conditions:

$$-\frac{1}{\tau_1^{[k]}} + \frac{1}{\tau_2^{[k]}} = \frac{1}{\tau_1^{[k+1]}} + \frac{1}{\tau_2^{[k+1]}} \tag{2.28}$$

$$-\frac{1}{\tau_1^{[k]}\tau_2^{[k]}} + \mu_{[k]}^2 = \frac{1}{\tau_1^{[k+1]}\tau_2^{[k+1]}} + \mu_{[k+1]}^2 \tag{2.29}$$

$$\frac{\tau_1^{[k]}\tau_2^{[k]}}{\mu_{[k]}^2} = \frac{\tau_1^{[k+1]}\tau_2^{[k+1]}}{\mu_{[k+1]}^2} \tag{2.30}$$

for $k = 1,...N$-1. Therefore, given the parameters of the first stage, the solutions for the following stages can be easily computed.

For filter designs, we usually use the bandwidth of the filter as a design specification instead of the decay time constant. Therefore, it would be useful to calculate the first stage based on a target filter bandwidth. For a second-order filter, the drop port power spectrum is

$$\mathrm{Drop}(\Delta\omega) = \frac{\mu^2 \frac{4}{\tau_1\tau_2}}{(-\Delta\omega^2 + \frac{1}{\tau_1\tau_2} + \mu^2)^2 + (\frac{1}{\tau_1} + \frac{1}{\tau_2})^2\Delta\omega^2} \tag{2.31}$$

We first define here

$$A = \frac{1}{\tau_1} + \frac{1}{\tau_2} \tag{2.32}$$

$$B = \frac{1}{\tau_1\tau_2} \tag{2.33}$$

and FWHM as $\mathrm{d}\omega$. For an N-split system, we need to satisfy

$$\frac{4B\mu^2}{(B+\mu^2)^2} = \frac{1}{N} \tag{2.34}$$

$$\frac{4B\mu^2}{(-\mathrm{d}\omega^2/4 + B + \mu^2)^2 + A^2\mathrm{d}\omega^2/4} = \frac{1}{2N} \tag{2.35}$$

Therefore, given the N and $\mathrm{d}\omega$, by specifying the value of B, we can calculate parameters μ, A, τ_1 and τ_2 as shown below:

$$\mu = \frac{(\sqrt{N} \pm \sqrt{N-1}) \cdot \sqrt{4B}}{2} \tag{2.36}$$

$$A = \sqrt{\frac{8BN\mu^2 - (-\mathrm{d}\omega^2/4 + B + \mu^2)^2}{\mathrm{d}\omega^2/4}} \tag{2.37}$$

$$\frac{1}{\tau_1} = \frac{A \pm \sqrt{A^2 - 4B}}{2} \tag{2.38}$$

$$\frac{1}{\tau_2} = \frac{A \mp \sqrt{A^2 - 4B}}{2} \tag{2.39}$$

Although the model described here does not include the loss inside the cavity for simplicity, in fact, similar to the first-order case, by adding a loss term τ_r into the calculation, we are able to arrive at the same recursive relations for an equal power delivery to all the drop ports for a second-order filter-based system. For even higher order partial-drop systems, the loss term cannot cancel itself during calculation and therefore plays a role in the recursive relations of the system. The inclusion of the cavity loss in high-order systems will be discussed in Sec. 2.5 of this chapter.

2.4.3 Experimental Implementation

Based on the developed theory, we designed a 1-by-8-port 2nd-order partial-drop system. The proposed structure was fabricated in a state-of-art CMOS foundry on a 300-mm SOI wafer with a 220-nm device layer using 193-nm optical immersion lithography. A scanning electron micrograph (SEM) of the fabricated device after a dry etch to remove the top SiO_2 cladding is shown in Fig. 2.20(a). It consists of eight 2nd-order partial-drop filters coupled to the same bus waveguide. Input laser power was coupled into the bus waveguide from the left side and filtered by each filter. Integrated heaters are introduced to each filter using the same way as described in Sec. 2.2.3. The fabricated adiabatic rings are 6-μm in diameter, ensuring a single-mode operation and a large free-spectral-range (FSR) of 36.2nm for WDM applications. A zoom-in of the first stage of the system is shown in Fig. 2.20(b). We observe that the 2nd-order filter has different coupling gaps to bus and drop waveguides. This difference allows the first stage to partially select the input power into the Drop1 port. In contrast, the last stage, as shown in Fig. 2.20(c), utilizes a symmetric coupling scheme, allowing a full power collection on resonance so as to achieve the same drop port spectrum as previous stages.

The transmission spectra of port Thru and Drop1 of the designed 1-by-8-port 2nd-order multicast filter bank are shown in Fig. 2.21(a). The FWHM bandwidth of Drop1 is ∼73 GHz. The experimental result matches well with the simulated one (blue dashed line). The simulated port Drop1 response of a 1-by-8-port 1st-order multicast filter bank is also plotted in Fig. 2.21(a) for comparison. Assuming a $<$ -25dB channel-to-nearest-channel crosstalk, a 1st-order system demands a 648 GHz channel spacing (marked by 1 in Fig. 2.21(a)), while a 2nd-order system only requires 250 GHz channel spacing (denoted by 2 in Fig. 2.21(a)), enabling ∼2.6× better channel density than the 1st-order design [28, 29]. The overall transmission spectra of the designed system after thermal tuning are shown in Fig. 2.21(b), and a zoom-in of the top part of the responses (marked by a dashed box in Fig. 2.21(b)) is shown in Fig. 2.21(c). The responses of Drop1 to Drop8 overlap closely with each other, showing a power variation of 1/4 dB on resonance and an FWHM bandwidth variation of 5.4 GHz, demonstrating the accuracy of both design and fabrication. In

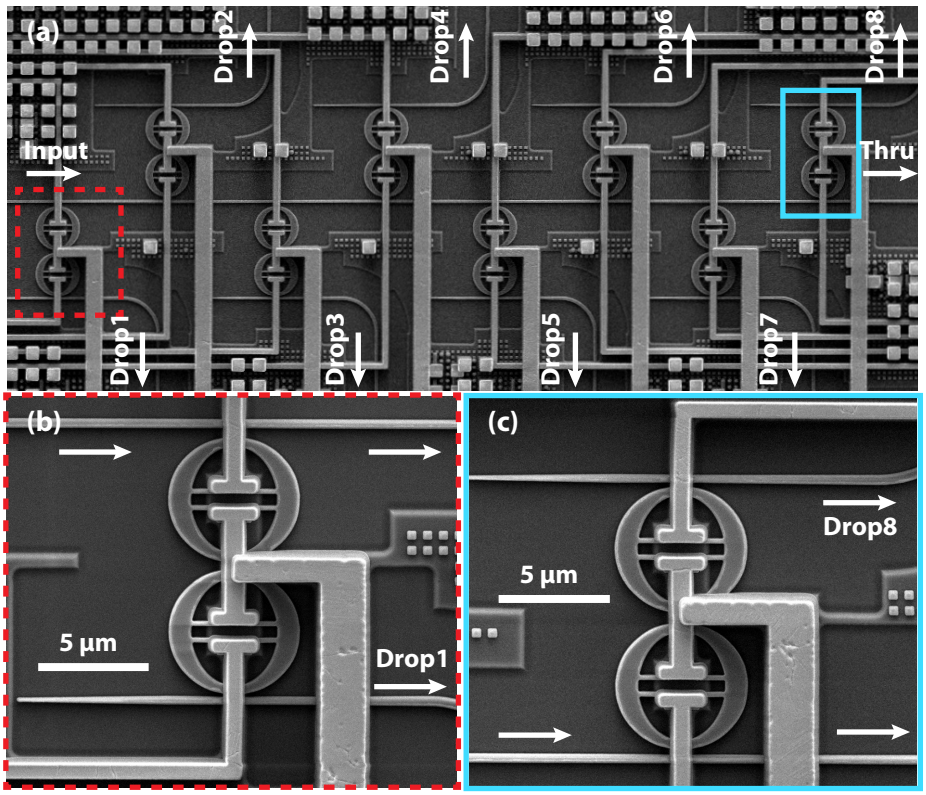

Fig. 2.20: (a) A scanning electron micrograph (SEM) of the fabricated device after a dry etching to remove the top SiO_2 cladding. (b) A zoom-in of the first stage (red dashed box in (a)). (c) A zoom-in of the last stage (solid cyan box in (a)).

addition, it is worth noticing that the overall loss of the system is only 1.7 dB, despite a large number of heaters and ring resonators involved in the system.

2.4.4 Conclusion

In this section, we proposed and demonstrated a 2nd-order wavelength selective 1-by-8-port multicast system using adiabatic microring tunable filters. The system provides an average 80.2GHz channel bandwidth with only a 5.4GHz standard deviation while maintaining a low 1/4 dB resonant power variation across all eight drop ports, demonstrating nearly identical responses. Compared with a 1st-order-based design, the sharp roll-off of the 2nd-order filter reduces channel spacing from 648GHz to 250GHz, enabling $\sim$2.6$\times$ higher channel density, making it attractive for applications such as on-chip multicast communications and integrated high-sensitivity transceiver designs.

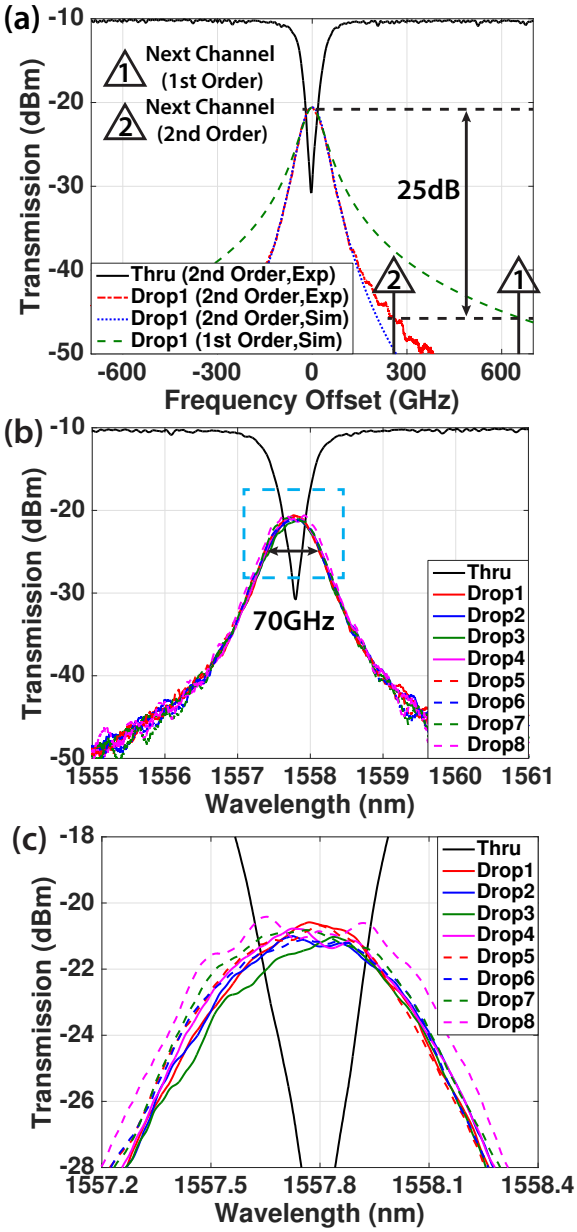

Fig. 2.21: (a) The transmission spectra of port Thru and Drop1 of the designed 1-by-8-port 2nd-order multicast filter bank. Simulated port Drop1 responses for both 1-by-8-port 1st-order and 2nd-order multicast filter bank with the same FWHM bandwidth are included for comparison. Nearby frequency channels with < -25dB crosstalk level are marked with 1 and 2 for 1st-order and 2nd-order system, respectively. (b) Transmission spectra of the thru and eight drop ports of the 2nd-order partial-drop filter bank after thermal tuning. (c) A zoom-in of the transmission spectra of the system (marked by a dashed box in (b)), showing a power variation of 1/4dB at the resonant wavelength.

2.5 Extension to Higher-Order Filter-Based Structure

While second-order filters offer a faster roll-off speed compared to first-order filters, there are situations where an even higher-order filter is required for a tighter channel spacing. Although the theoretical calculations become more complex for filters with higher orders, the recursive conditions are, in fact, not difficult to achieve.

Here we give an example for how to achieve a third-order even-split system. Based on the coupled-mode-theory, we can write the thru and drop port amplitude responses as

$$t = \frac{(j\Delta\omega - \frac{1}{\tau_1})[j\Delta\omega(j\Delta\omega + \frac{1}{\tau_2}) + \mu_2^2] + \mu_1^2(j\Delta\omega + \frac{1}{\tau_2})}{(j\Delta\omega + \frac{1}{\tau_1})[j\Delta\omega(j\Delta\omega + \frac{1}{\tau_2}) + \mu_2^2] + \mu_1^2(j\Delta\omega + \frac{1}{\tau_2})} \tag{2.40}$$

$$d = \frac{\mu_1\mu_2\sqrt{\frac{2}{\tau_1}}\sqrt{\frac{2}{\tau_2}}}{(j\Delta\omega + \frac{1}{\tau_1})[j\Delta\omega(j\Delta\omega + \frac{1}{\tau_2}) + \mu_2^2] + \mu_1^2(j\Delta\omega + \frac{1}{\tau_2})} \tag{2.41}$$

The equal-power-split condition is

$$t_{[k]} \cdot d_{[k+1]} = d_{[k]} \tag{2.42}$$

for any value of $\Delta\omega$. Therefore, we need the following conditions

$$(\frac{\mu_1^2\mu_2^2}{\tau_1\tau_2})_{[k]} = (\frac{\mu_1^2\mu_2^2}{\tau_1\tau_2})_{[k+1]} \tag{2.43}$$

$$\begin{aligned}&\{(j\Delta\omega - \frac{1}{\tau_1})[j\Delta\omega(j\Delta\omega + \frac{1}{\tau_2}) + \mu_2^2] + \mu_1^2(j\Delta\omega + \frac{1}{\tau_2})\}_{[k]}\\ =&\{(j\Delta\omega + \frac{1}{\tau_1})[j\Delta\omega(j\Delta\omega + \frac{1}{\tau_2}) + \mu_2^2] + \mu_1^2(j\Delta\omega + \frac{1}{\tau_2})\}_{[k+1]}\end{aligned} \tag{2.44}$$

to be satisfied for k = 1,...N-1 and any value of $\Delta\omega$. By matching all the orders of $\Delta\omega$ in Eqn. 2.44, we can simplify Eqn. 2.43 and Eqn. 2.44 into four conditions:

$$\frac{\mu_{1[k]}^2\mu_{2[k]}^2}{\tau_1^{[k]}\tau_2^{[k]}} = \frac{\mu_{1[k+1]}^2\mu_{2[k+1]}^2}{\tau_1^{[k+1]}\tau_2^{[k+1]}} \tag{2.45}$$

$$-\frac{\mu_{2[k]}^2}{\tau_1^{[k]}} + \frac{\mu_{1[k]}^2}{\tau_2^{[k]}} = \frac{\mu_{2[k+1]}^2}{\tau_1^{[k+1]}} + \frac{\mu_{1[k+1]}^2}{\tau_2^{[k+1]}} \tag{2.46}$$

$$\mu_{1[k]}^2 + \mu_{2[k]}^2 - \frac{1}{\tau_1^{[k]}\tau_2^{[k]}} = \mu_{1[k+1]}^2 + \mu_{2[k+1]}^2 + \frac{1}{\tau_1^{[k+1]}\tau_2^{[k+1]}} \tag{2.47}$$

$$-\frac{1}{\tau_1^{[k]}} + \frac{1}{\tau_2^{[k]}} = \frac{1}{\tau_1^{[k+1]}} + \frac{1}{\tau_2^{[k+1]}} \tag{2.48}$$

The conditions for a fourth-order filter-based multicast system are also listed here for reference.

$$\frac{\mu_{1[k]}^2\mu_{2[k]}^2\mu_{3[k]}^2}{\tau_1^{[k]}\tau_2^{[k]}} = \frac{\mu_{1[k+1]}^2\mu_{2[k+1]}^2\mu_{3[k+1]}^2}{\tau_1^{[k+1]}\tau_2^{[k+1]}} \tag{2.49}$$

$$\mu_{1[k]}^2\mu_{3[k]}^2 - \frac{\mu_{2[k]}^2}{\tau_1^{[k]}\tau_2^{[k]}} = \mu_{1[k+1]}^2\mu_{3[k+1]}^2 + \frac{\mu_{2[k+1]}^2}{\tau_1^{[k+1]}\tau_2^{[k+1]}} \tag{2.50}$$

$$-\frac{\mu_{2[k]}^2 + \mu_{3[k]}^2}{\tau_1^{[k]}} + \frac{\mu_{1[k]}^2 + \mu_{2[k]}^2}{\tau_2^{[k]}} = \frac{\mu_{2[k+1]}^2 + \mu_{3[k+1]}^2}{\tau_1^{[k+1]}} + \frac{\mu_{1[k+1]}^2 + \mu_{2[k+1]}^2}{\tau_2^{[k+1]}} \tag{2.51}$$

$$\mu_{1[k]}^2 + \mu_{2[k]}^2 + \mu_{3[k]}^2 - \frac{1}{\tau_1^{[k]}\tau_2^{[k]}} = \mu_{1[k+1]}^2 + \mu_{2[k+1]}^2 + \mu_{3[k+1]}^2 - \frac{1}{\tau_1^{[k+1]}\tau_2^{[k+1]}} \tag{2.52}$$

$$-\frac{1}{\tau_1^{[k]}} + \frac{1}{\tau_2^{[k]}} = \frac{1}{\tau_1^{[k+1]}} + \frac{1}{\tau_2^{[k+1]}} \tag{2.53}$$

To generalize the even-power-split conditions for an mth-order filter-based system, we define functions f and G as

$$f_\mu(x) = j\Delta\omega + \frac{\mu^2}{x} \tag{2.54}$$

$$G = f_1(\tau_2) \tag{2.55}$$

This way, we convert the conditions into

$$(\frac{\prod_{i=1}^{m-1}\mu_i^2}{\tau_1\tau_2})_{[k]} = (\frac{\prod_{i=1}^{m-1}\mu_i^2}{\tau_1\tau_2})_{[k+1]} \tag{2.56}$$

$$\begin{aligned}&\{G \cdot f_{\mu_{m-1}}(G) \cdot f_{\mu_{m-2}}(f_{\mu_{m-1}}(G)) \cdot \ \cdots \ \cdot f_{\mu_2}(\cdots(f_{\mu_{m-1}}(G)))\\ &\cdot [f_{\mu_1}(\cdots(f_{\mu_{m-1}}(G))) - \frac{1}{\tau_1}]\}_{[k]} = \{G \cdot f_{\mu_{m-1}}(G) \cdot f_{\mu_{m-2}}(f_{\mu_{m-1}}(G)) \cdot \ \cdots\\ &\cdot f_{\mu_2}(\cdots(f_{\mu_{m-1}}(G))) \cdot [f_{\mu_1}(\cdots(f_{\mu_{m-1}}(G))) + \frac{1}{\tau_1}]\}_{[k+1]}\end{aligned} \tag{2.57}$$

Therefore, even-power-split conditions for an m-order filter-based system can be gen-

eralized as

$$(\frac{\prod_{i=1}^{m-1}\mu_i^2}{\tau_1\tau_2})_{[n]} = (\frac{\prod_{i=1}^{m-1}\mu_i^2}{\tau_1\tau_2})_{[n+1]} \tag{2.58}$$

$$(-\frac{1}{\tau_1}+\frac{1}{\tau_2})_{[n]} = (\frac{1}{\tau_1}+\frac{1}{\tau_2})_{[n+1]} \tag{2.59}$$

$$(-\frac{1}{\tau_1\tau_2}+\sum_{i=1}^{m-1}\mu_i^2)_{[n]} = (\frac{1}{\tau_1\tau_2}+\sum_{i=1}^{m-1}\mu_i^2)_{[n+1]} \tag{2.60}$$

$$(-\frac{\sum_{i=2}^{m-1}\mu_i^2}{\tau_1}+\frac{\sum_{i=1}^{m-2}\mu_i^2}{\tau_2})_{[n]} = (\frac{\sum_{i=2}^{m-1}\mu_i^2}{\tau_1}+\frac{\sum_{i=1}^{m-2}\mu_i^2}{\tau_2})_{[n+1]} \tag{2.61}$$

$$(-\frac{\sum_{i=2}^{m-2}\mu_i^2}{\tau_1\tau_2}+\sum_{i=1}^{m-1}\sum_{j=i+2}^{m-1}\mu_i^2\mu_j^2)_{[n]} = (\frac{\sum_{i=2}^{m-2}\mu_i^2}{\tau_1\tau_2}+\sum_{i=1}^{m-1}\sum_{j=i+2}^{m-1}\mu_i^2\mu_j^2)_{[n+1]} \tag{2.62}$$

$$\begin{aligned}(-\frac{\sum_{i=2}^{m-1}\sum_{j=i+2}^{m-1}\mu_i^2\mu_j^2}{\tau_1}+\frac{\sum_{i=1}^{m-2}\sum_{j=i+2}^{m-1}\mu_i^2\mu_j^2}{\tau_2})_{[n]} = \\ (\frac{\sum_{i=2}^{m-1}\sum_{j=i+2}^{m-1}\mu_i^2\mu_j^2}{\tau_1}+\frac{\sum_{i=1}^{m-2}\sum_{j=i+2}^{m-1}\mu_i^2\mu_j^2}{\tau_2})_{[n+1]}\end{aligned} \tag{2.63}$$

$$\begin{aligned}&(-\frac{\sum_{i=2}^{m-2}\sum_{j=2}^{m-2}\mu_i^2\mu_j^2}{\tau_1\tau_2}+\sum_{i=1}^{m-1}\sum_{j=i+2}^{m-1}\sum_{k=j+2}^{m-1}\mu_i^2\mu_j^2\mu_k^2)_{[n]} \\ &= (\frac{\sum_{i=2}^{m-2}\sum_{j=2}^{m-2}\mu_i^2\mu_j^2}{\tau_1\tau_2}+\sum_{i=1}^{m-1}\sum_{j=i+2}^{m-1}\sum_{k=j+2}^{m-1}\mu_i^2\mu_j^2\mu_k^2)_{[n+1]}\end{aligned} \tag{2.64}$$

.....

for $n = 1$,...N-1, where N is the number of splits. Eqn. 2.58 is the general condition for filter-based system of any order. When $m = 1$, it reduces to $(1/\tau_1\tau_2)_{[n]} = (1/\tau_1\tau_2)_{[n+1]}$. The number of total conditions for an mth-order filter-based system is m+1. While the above conditions ignore the contributions of internal loss of the cavities, a similar calculation process can be used to calculate the case when the internal loss is not negligible. The results can be easily achieved by replacing $1/\tau_1$ and $1/\tau_2$ on the left side of Eqn. 2.59–2.64 with $1/\tau_1 - 1/\tau_r$ and $1/\tau_2 + 1/\tau_r$ while replacing right-sided $1/\tau_1$ and $1/\tau_2$ with $1/\tau_1 + 1/\tau_r$ and $1/\tau_2 + 1/\tau_r$ respectively. We observe that the recursive relations for first-order and second-order filter-based even-drop structures will be independent of internal loss even if the loss is relatively high, while higher-order filter-based multicast systems need to take account of internal loss during the design process.

CHAPTER 3

Resonant Germanium-on-Silicon Detector

In this chapter, a waveguide-coupled resonant germanium-on-silicon detector is presented. Based on silicon and germanium refractive indices information, coupled-mode-theory was first used to analyze the feasibility of this structure type. The design was then implemented in a CMOS fabrication foundry by introducing a vertical p-i-n junction within a cavity. A dark current of nA-scale, photoresponsivity of 1A/W and optoelectric bandwidth of 32GHz were demonstrated with a device radius of 4.5μm. In addition, its potential applications in an optical multicast system were also investigated, providing an excellent solution to further simplification of optical networks.

3.1 Introduction

Silicon photonics provides a promising solution to the ever-worsening bandwidth and power-consumption bottlenecks in both on- and off-chip interconnections [52]. The active participation of well-established Complementary-Metal-Oxide-Semiconductor (CMOS) foundries paves the way for custom fabrication processes tailored for large-scale electronics-photonics integration [10, 14, 15, 53]. Thus far, near infrared photodetection has been achieved in a variety of materials, including germanium [54, 55, 56, 57, 9, 58, 59], polycrystalline silicon [60, 35, 34], III-V materials [61, 62, 63, 64], and two-dimensional materials [65]. Among them, germanium has the advantages of high responsivity and CMOS-compatible integration on silicon.

Germanium has a direct band gap of ∼0.8eV, making it a perfect detecting material for wavelengths shorter than 1.55μm. Sub-bandgap photodetection requires an increase of detector sizes, which, in turn, introduces a larger dark current and results in a slower performance. In order to achieve an efficient photodetection beyond 1.55μm without compromising the device performance, engineering material bandgaps with strained germanium processes was offered as a solution [54]. Demonstrations in guided optical devices were followed using butt- or evanescent-coupled waveguide designs [55, 56, 57, 9, 58, 59]. However, for those designs, interaction lengths are still relatively short to enable efficient detections for longer wavelengths (e.g. L-band - 1565 to 1625 nm). The increase in device length, however, can be compensated by utilizing resonant structures where the absorption will only be limited to Q-factor matching instead of physical device size. Apart from a performance improvement in responsivity, a resonant detector is, by itself, a combination of both filter and detector, making it possible to further reduce the footprint of a WDM receiver as the integrated system becomes denser and denser. While resonant detectors have been demonstrated in polycrystalline silicon [60, 35, 34], resonant germanium-on-silicon photodetectors integrated on a silicon photonic platform are to-date unexplored.

3.2 Theories and Simulations

For crystal silicon material used in our platform, we have a combined (material and fabrication) loss of ∼2dB/cm. This gives us a material limited Q-factor of

$\sim 3\times10^5$. For simulation purpose, we select the refractive index of the silicon to be $3.48+6\times10^{-6}i$ for convenience, corresponding to a loss of 2dB/cm for the silicon waveguides. In our platform, a layer of germanium is grown on top of the silicon. Therefore, the loss inside the germanium-on-silicon microcavities will include absorptions from both germanium and silicon. Light can be coupled into the cavity from a nearby waveguide through evanescent coupling. This type of system can be modeled with coupled-mode-theory [33] using the following equations:

$$\frac{d}{dt}a_1 = (j\omega_0 - \frac{1}{\tau_1} - \frac{1}{\tau_{Si}} - \frac{1}{\tau_{Ge}})a_1 - j\sqrt{\frac{2}{\tau_1}}S_i \tag{3.1}$$

$$S_t = S_i - j\sqrt{\frac{2}{\tau_1}}a_1 \tag{3.2}$$

where τ_1 is the time constant related to coupling coefficient, and τ_{Si} and τ_{Ge} stand for the time constants due to silicon and germanium material in the cavity, respectively. Therefore, the power absorbed by germanium can be represented as

$$\text{Absorption}(Ge) = \frac{\frac{4}{\tau_1 \cdot \tau_{Ge}}}{(\omega_0 - \omega)^2 + (1/\tau_1 + 1/\tau_{Si} + 1/\tau_{Ge})^2} \tag{3.3}$$

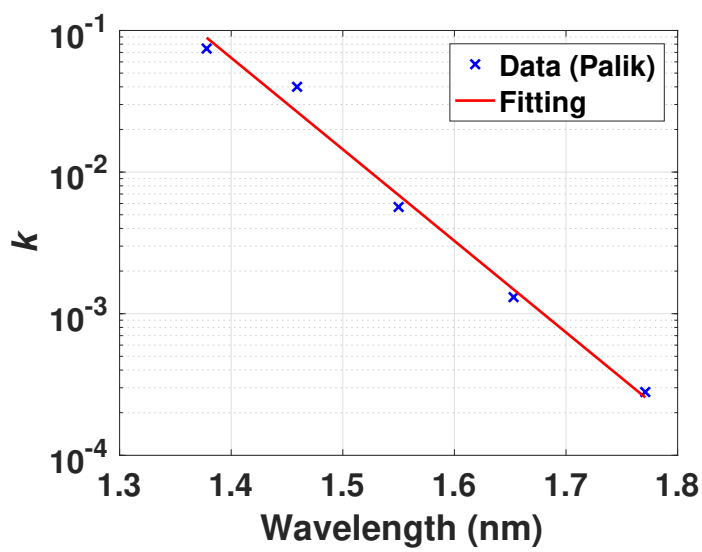

Fig. 3.1: Imaginary components of the germanium refractive indices for wavelength from 1.4-1.8μm in Ref. [66].

For the following simulation, we use germanium indices information provided in Ref. [66]. The imaginary components (k) of the refractive indices for wavelengths from 1.4-1.8μm are shown in Fig. 3.1. We observe that k roughly follows an exponential

decay for the wavelength range of interest. For a wavelength change from 1.50μm to 1.65μm, k drops around ten times, leading to a less efficient absorption for a longer wavelength. However, even though k is small for a longer wavelength, if we make a resonator that supports a mode that is mostly inside the germanium, the resulting loss of the cavity will be significant, leading to a relatively low intrinsic Q-factor. Under that situation, the designed resonant detector will have a broad optical bandwidth and, therefore, fail to act as a filter.

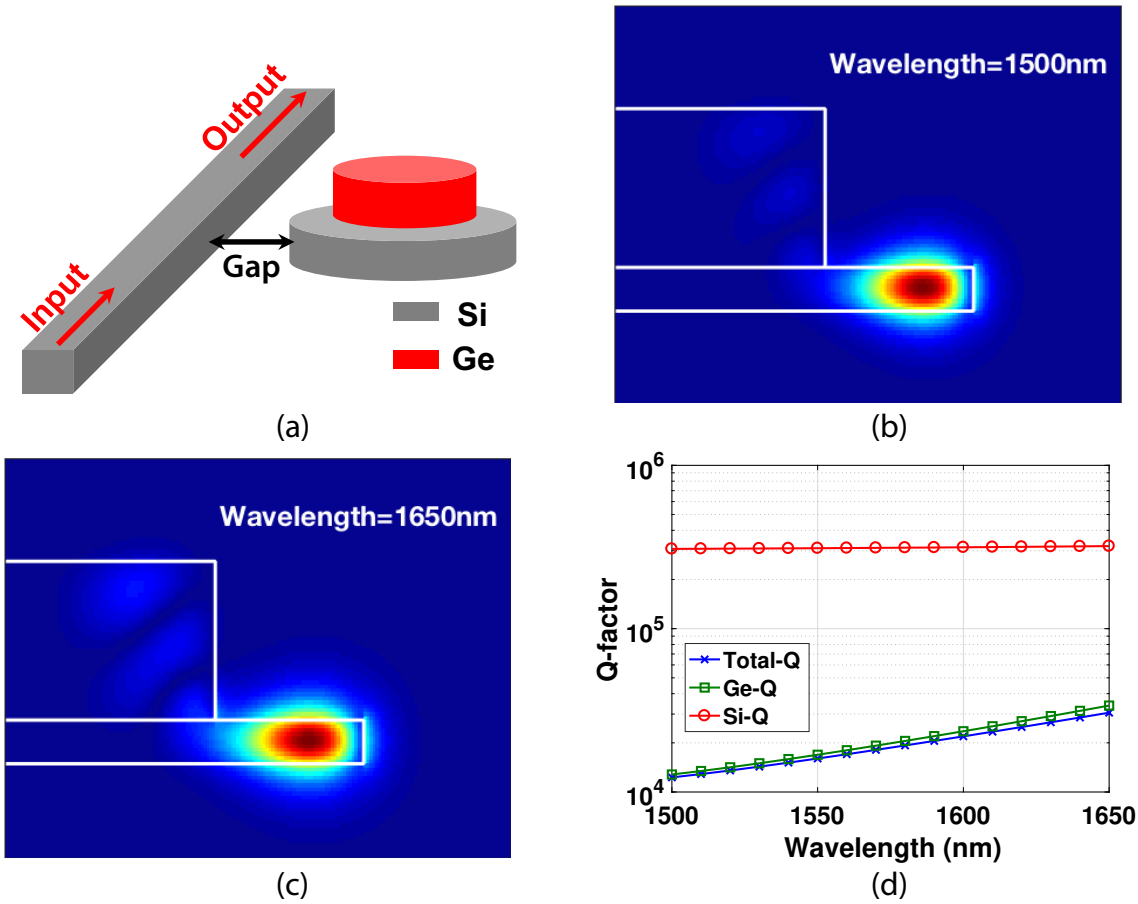

Fig. 3.2: (a) A schematic of the proposed waveguide-coupled germanium-on-silicon photodetector. (b) Fundamental mode (TE_{11}) at $\lambda = 1500$nm. (c) Fundamental mode (TE_{11}) at $\lambda = 1650$nm. (d) Calculated total intrinsic Q-factors for wavelengths from 1500 to 1650nm. Contributions from the Ge absorption and silicon absorption to the total Q of the Ge-on-Si microcavity are also plotted separately.

The proposed waveguide-coupled Ge-on-Si resonator is shown in Fig. 3.2(a). In our platform, germanium is directly grown on top of the silicon which has a far

lower absorption than that of germanium. The difference in absorption coefficients provides a possibility to create a relatively high-Q mode with only a partial intensity overlap with germanium. However, eigenmodes of a photonics device tend to have a significant overlap with high-index materials. Therefore, to create a resonant mode that are mostly inside low-index material, the large difference in the real part of the refractive indices between germanium and silicon needs to be mitigated. The desired mode was achieved with concentric silicon and germanium disk cavities where the outer radius of the germanium disk is offset inward. Fig. 4.7(b) and (c) shows the calculated fundamental mode (TE_{11}) of the cavity for wavelength of 1500 and 1650nm, respectively. We observe that with the help of a relatively small bend radius, the eigenmode of the cavity is pushed outward, reducing the overlap with germanium material.

Another benefit of this cavity is its less dependence of intrinsic Q-factor on the wavelength. By comparing Fig. 3.2(b) and (c), we observe that the resonant mode starts having more mode overlap with germanium when the wavelength gets longer, which compensates the decrease of germanium absorption coefficient, making it possible to detect wavelengths of different optical bands with a single device. Fig. 3.2(d) shows the calculated intrinsic Q-factor dependence on the wavelength. The decomposed contributions from germanium and silicon to the total intrinsic Q-factor are also plotted separately. We notice that the major contribution to the total Q-factor is germanium, as is required to generate the photocurrent. The calculated intrinsic Q-factor is increased by only three times from 1500 to 1650nm, while in contrast, the Q-factor will increase by ten times if no mode expansion occurs.

To simulate the coupling Q-factors from the bus waveguide to the Ge-on-Si detector, we use the coupling to a silicon disk resonator as an approximation in FDTD simulations since the resonant mode has only a small fraction of overlap with the germanium material. The schematic of the simulated structure is shown in Fig. 3.3(a), consisting of a silicon bus waveguide coupled to a silicon disk resonator. The bus waveguide width is selected to be 400nm for phase matching to the resonant mode while allowing an adequate power coupling for a waveguide-to-disk separation larger than 100nm (gap size limited by the foundry process). Since a microdisk resonator is

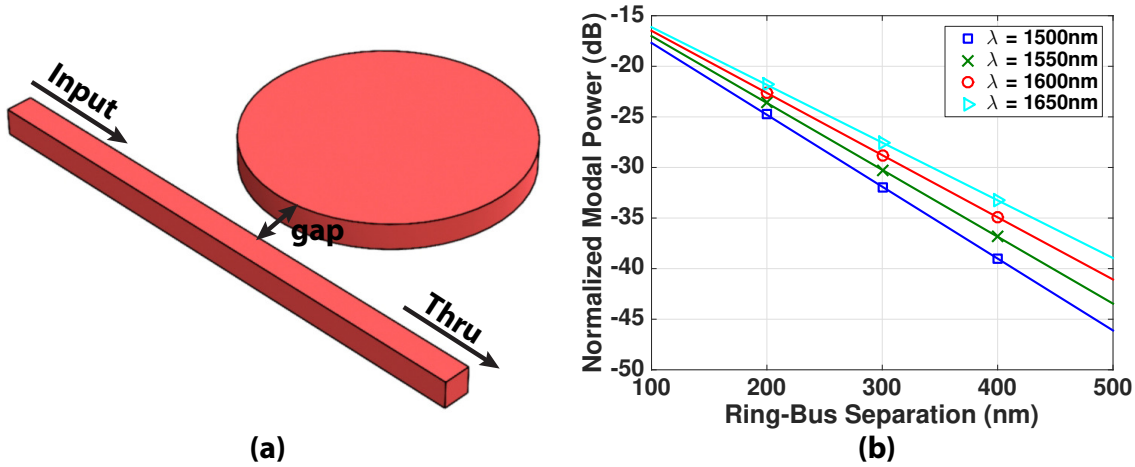

Fig. 3.3: (a) A schematic of a waveguide coupled to a microdisk for FDTD simulations. (b) Coupling strengths vs. coupling gap sizes and wavelengths.

multimode in its nature, multiple modes will be excited with the bus waveguide coupling. We took mode overlap of the overall excited modes with the fundamental TE mode of the cavity. The normalized modal power for different ring-bus separations is shown in Fig. 3.3(b).

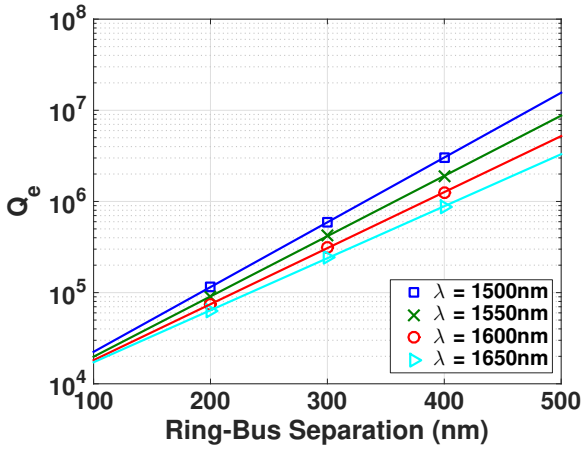

Fig. 3.4: Coupling Q-factor (Q_e) for different ring-bus separations and wavelengths.

For a 4.5μm-radius disk, the simulated free-spectral-range in wavelength is 24.7nm. Therefore, we can convert the normalized modal power couplings into coupling Q-factors using

$$Q = \frac{2\pi\omega_0}{\kappa^2 \cdot FSR(\omega)} \tag{3.4}$$

where κ^2 represents the coupling coefficient, ω_0 is the resonant angular frequency

and $FSR(\omega)$ stands for the free-spectra-range of the resonator measured in angular frequency. Fig. 3.4 shows the converted coupling Q-factor (Q_e) for different ring-bus separations and wavelengths. We can see that Q_e decreases for longer wavelengths and the difference of Q_e between shorter and longer wavelengths becomes smaller for smaller coupling gaps.

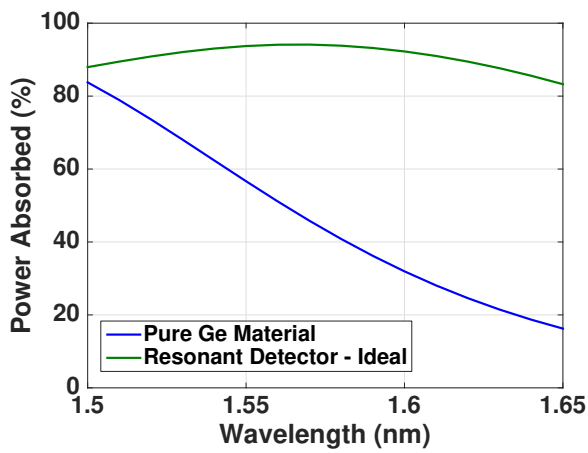

Fig. 3.5: Comparison of a 15µm-long pure germanium absorption and a resonant Ge-on-Si photodetector absorption.

For a coupling gap of 100nm, the absorbed power is calculated using both Q_i and Q_e. A comparison between the simulated resonant germanium detector and a pure germanium material (assuming 15µm in length) is shown in Fig. 3.5. We observe that for shorter wavelengths, the resonant detector has a similar absorption as the straight germanium material. However, for longer wavelengths, with the resonance enhancement, the resonant detector shows a factor of four improvement in power absorption at the wavelength of 1650nm, proving the effectiveness of the resonant-based design.

3.3 Design and Performance Characterization

3.3.1 Device Fabrication and Passive Cavity Calibration

To implement the simulated device in our fabrication process, a schematic cross-section view of the proposed resonant-based germanium-on-silicon detector is shown in Fig. 3.6(a). The waveguide width is 400nm to ensure a single-mode operation in the bus waveguide for wavelengths around 1550nm. ΔR_{Si-Ge} on Fig. 3.6(a) stands

for the separation between the germanium and silicon outer-radius. Silicon doping (bottom of Fig. 3.6(a)), intrinsic germanium (i-Ge) and germanium doping together form the p-i-n junction of the resonant detector. For metal contacts to the germanium, circular contacts [3] are utilized to bring metal contacts close to where the carriers are generated, which further reduces the device resistance. Input power from a bus waveguide is coupled into the resonator and absorbed inside the cavity. The photodetector responsivity will be primarily limited by the ratio between the absorption of the intrinsic germanium which generates electron-hole pairs and other loss mechanisms such as the radiation loss of the cavity design and absorption losses of doped silicon and doped germanium. Radiation loss of the resonator is negligible with a radius of 4.5-µm and a high refractive index contrast between silicon (∼3.48) and silicon dioxide (∼1.44). In order to reduce the doping-induced loss, the silicon underneath germanium is lowly doped to keep the absorption loss low while maintaining an efficient collection of the generated photocurrent. Besides, the separation ΔR_{Si-Ge} is carefully selected to allow a small tail of the resonant mode to be in the intrinsic germanium, reducing overlap with the doped germanium on top. Through matching the external quality factor (Q-factor) to the intrinsic Q-factor of the cavity, power at the resonant wavelength can be fully coupled and absorbed with a high quantum efficiency.

We fabricated the design shown in Fig. 3.6(a) on a 300-mm silicon-on-insulator wafer with a 220-nm silicon layer and a 2-µm buried oxide using a 193-nm optical immersion lithography. Germanium of ∼0.8-µm-thick is hetero-epitaxially grown into the deep oxide trench on top of the thin silicon layer using a similar technique described in Ref. [14]. Fig. 3.6(b) shows a top-view optical microscope image of the fabricated resonant detector.

We first measured the intrinsic Q-factors of the resonant cavity by fitting the transmission responses of a series of devices with different coupling gaps (for different external Q-factors) and different sizes of ΔR_{Si-Ge} (for different internal Q-factors) to the coupled-mode-theory model [67, 33]. Fig. 3.7 shows the measured intrinsic Q-factors of three transverse-electric (TE) modes (TE_{11}, TE_{21} and TE_{31}) of different orders with different silicon to germanium separations ($\Delta R_{Si-Ge} = 1.0$ to 2.0µm). As

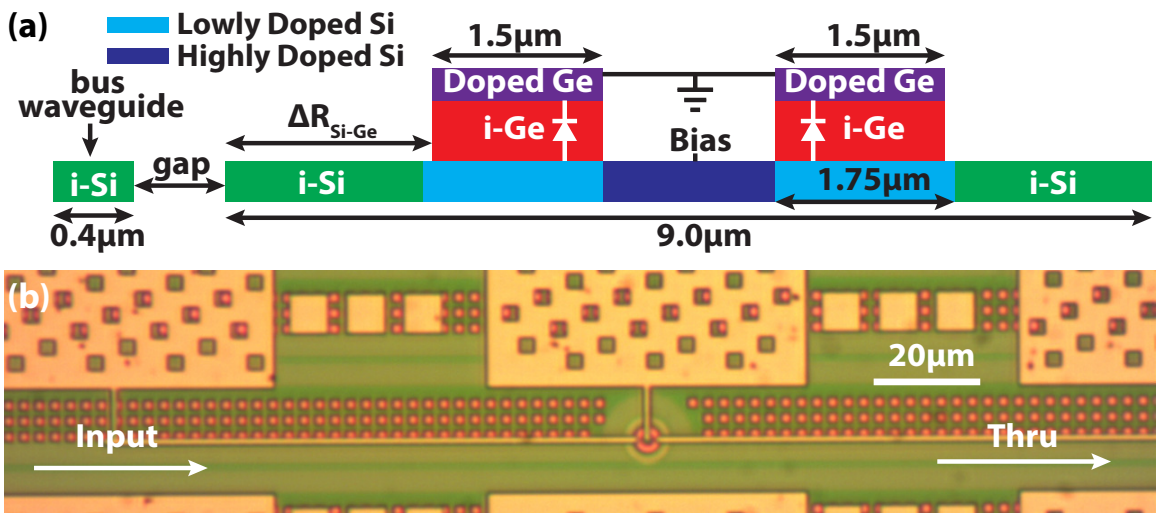

Fig. 3.6: (a) A schematic cross-sectional view of the resonant germanium-on-silicon detector. ΔR_{Si-Ge} here stands for the difference between the germanium and silicon outer-radius. (b) A top-view optical microscope image of the fabricated resonant detector.

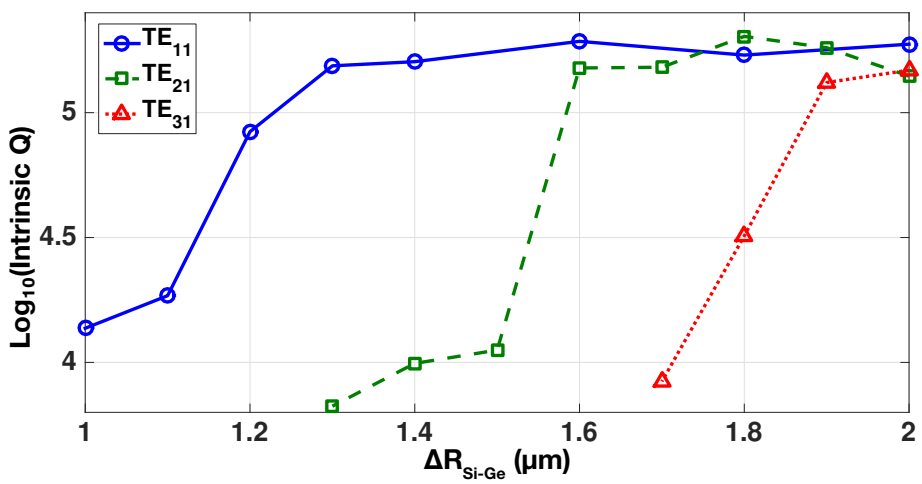

Fig. 3.7: Intrinsic Q-factors for transverse-electric modes (TE_{11}, TE_{21}, and TE_{31}) with different silicon and germanium outer-radius distances (ΔR_{Si-Ge}) for a wavelength around 1530nm.

the separation ΔR_{Si-Ge} gets smaller, the intrinsic Q-factors of the modes in the cavity decrease, indicating increasing mode overlaps with germanium. The radial order of the mode also affects the mode overlap with the germanium as higher order modes are less confined, resulting in germanium absorption limited intrinsic Q-factors occurring at $\Delta R_{Si-Ge} = 1.1$, 1.5 and 1.8µm for TE_{11}, TE_{21} and TE_{31} modes, respectively. While the experimental results are straightforward, the overall system is relatively difficult

to simulate without the exact information of the indices (both real and imaginary part) of the specific germanium used in the process. This problem can be solved in future device iterations with characterization structures on-chip for the process calibration.

3.3.2 Dark Current and Responsivity

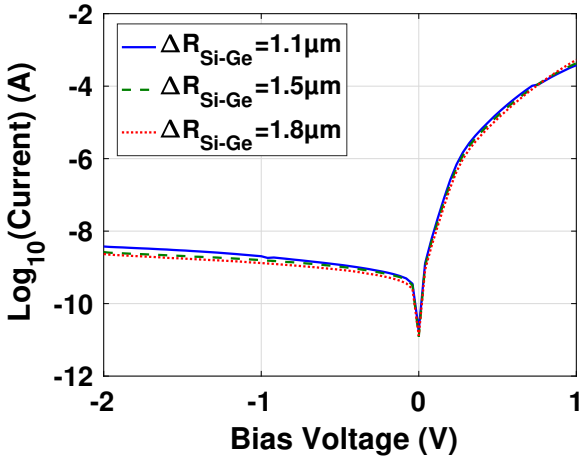

Fig. 3.8: I-V curves of resonant detector with ΔR_{Si-Ge} of 1.1, 1.5 and 1.8μm, showing nA-scale dark currents at -1V bias voltage.

I-V curves for germanium p-i-n diodes within resonant detectors with ΔR_{Si-Ge} = 1.1, 1.5 and 1.8μm are measured, showing nA-scale dark currents at -1V bias voltage (Fig. 3.8). The dark current of the device with ΔR_{Si-Ge} of 1.1μm is measured to be 2.03nA at a -1V bias voltage, corresponding to a dark current density of 8.13mA/cm^2. The measured germanium dark current is comparable to the straight waveguide detector demonstrated in Ref. [14], which was fabricated using the same germanium recipe.

To characterize responsivities of the detectors, we use a tunable laser with a tuning range from 1460 to 1640nm. The tunable laser was adjusted to the TE polarization and coupled in and out of the fabricated chip using single-mode fibers. The transmission spectrum of the through port was recorded using an external detector. A ground-signal-ground (GSG) high-speed probe was contacted to the device. A Keithley Source Measure Unit (SMU) was used to bias the photodetector and readout the photocurrent at the same time. The transmission spectra together with the measured

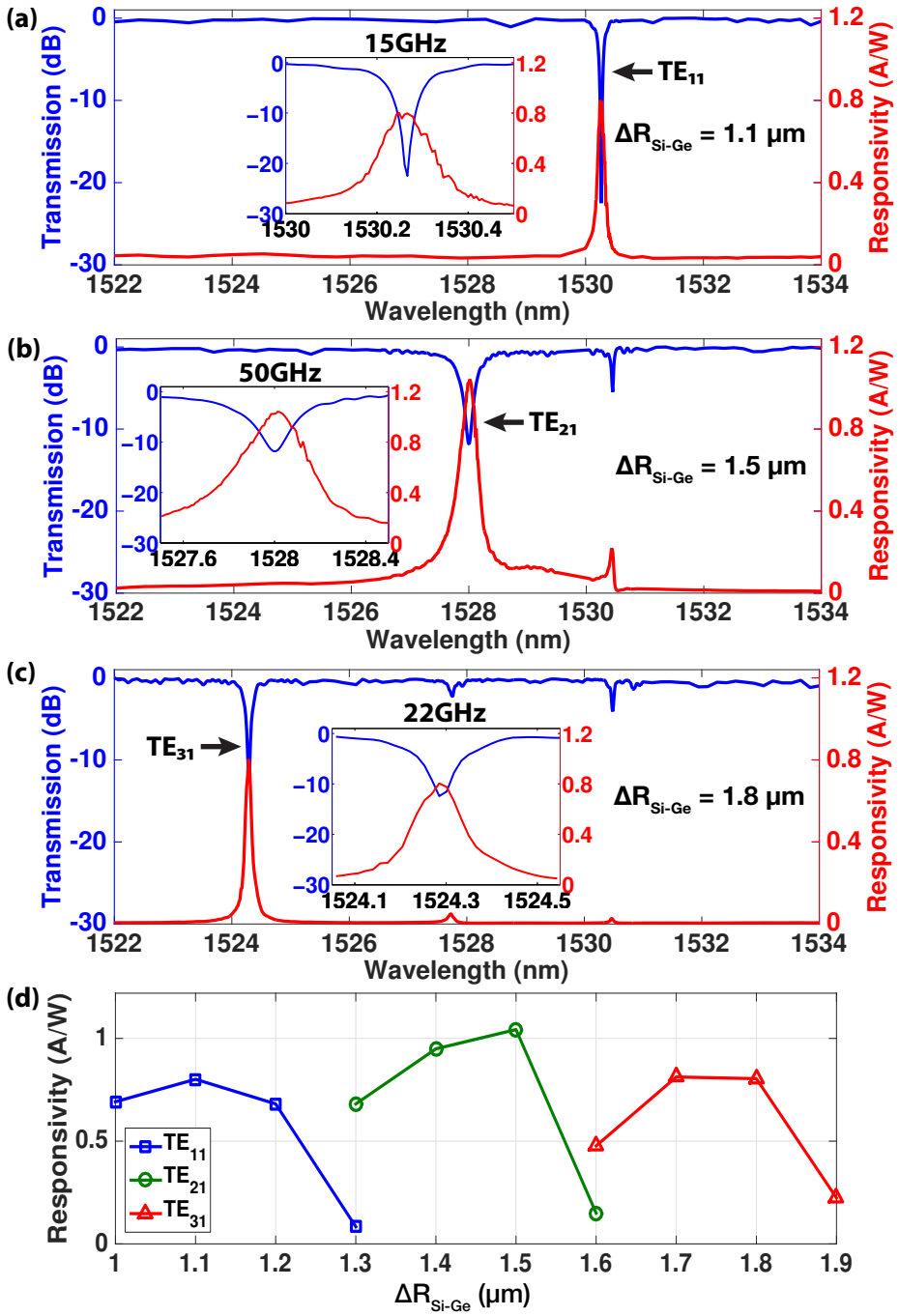

Fig. 3.9: (a-c) Transmission spectra and responsivities for resonant detectors with ΔR_{Si-Ge} of 1.1, 1.5 and 1.8μm at a bus-to-resonator gap of 100-nm for wavelength around 1528-nm. Inset: zoom-ins around resonances, showing filter bandwidths of 15, 50 and 22GHz, respectively. (e) Responsivities of devices with different ΔR_{Si-Ge} for modes TE_{11}, TE_{21} and TE_{31} with the same 100-nm gap around wavelength 1528nm.

responsivity curves for different modes with a 100-nm bus-to-resonator gap are shown in Fig. 3.9(a-c). When the wavelength of the input laser matches a resonance of the cavity, the light will be trapped and absorbed by the cavity. The light absorbed by the intrinsic germanium is then converted to photocurrents, shown as photocurrent peaks in Fig. 3.9(a-c). A responsivity as high as 1.04A/W is achieved for the device with ΔR_{Si-Ge} = 1.5μm and gap = 100nm around the wavelength 1528nm. Different optical full-width-half-maximum (FWHM) bandwidths (15, 50 and 22GHz) were observed for resonant modes with different radial orders, determined by the total Q-factors of the resonant cavities (Fig. 3.9(a-c) insets). Fig. 3.9(d) shows the responsivities of different modes for various ΔR_{Si-Ge} sizes with a 100-nm bus-to-resonator gap around the wavelength 1528nm. Peak responsivities for different modes (e.g. 1.1μm for TE_{11}, 1.5μm for TE_{21} and 1.7μm for TE_{31}) are observed, corresponding to nearly matched Q-factor points of corresponding modes. With resonant nature, the devices demonstrated here can also act as a wavelength-selective photodetector, combining wavelength filtering and signal detecting functions. Furthermore, the structure can be optimized with a pulley coupling scheme [68] to allow for a selective coupling to a chosen mode while maintaining a relatively large coupling coefficient to the cavity. The selective coupling will suppress excitations of unwanted modes and extend the free-spectral-range (FSR) of the device.

The measurement results shown in Fig. 3.9 focus on wavelengths around 1530nm. For other wavelengths, to optimize responsivities of the resonant detector, the external Q-factor should match the intrinsic Q-factor. Though the loss associated with the i-Ge absorption decreases rapidly with the increase of wavelength, the intrinsic Q-factor of the resonator increases slowly as a result of mode expansions for longer wavelengths. This property, in turn, makes it possible for a single device to maintain relatively high responsivities for both short (<1520nm) and long wavelengths (>1580nm) with a fixed bus-to-resonator gap.

Fig. 3.10(a-c) show the responsivities for different resonant wavelengths and coupling gaps for ΔR_{Si-Ge} sizes of 1.1, 1.4 and 1.7μm. For the device with a ΔR_{Si-Ge} of 1.4μm and a coupling gap of 100nm, a responsivity as high as 0.8A/W was achieved for short wavelength (∼1480nm) while maintaining a relatively high responsivity of

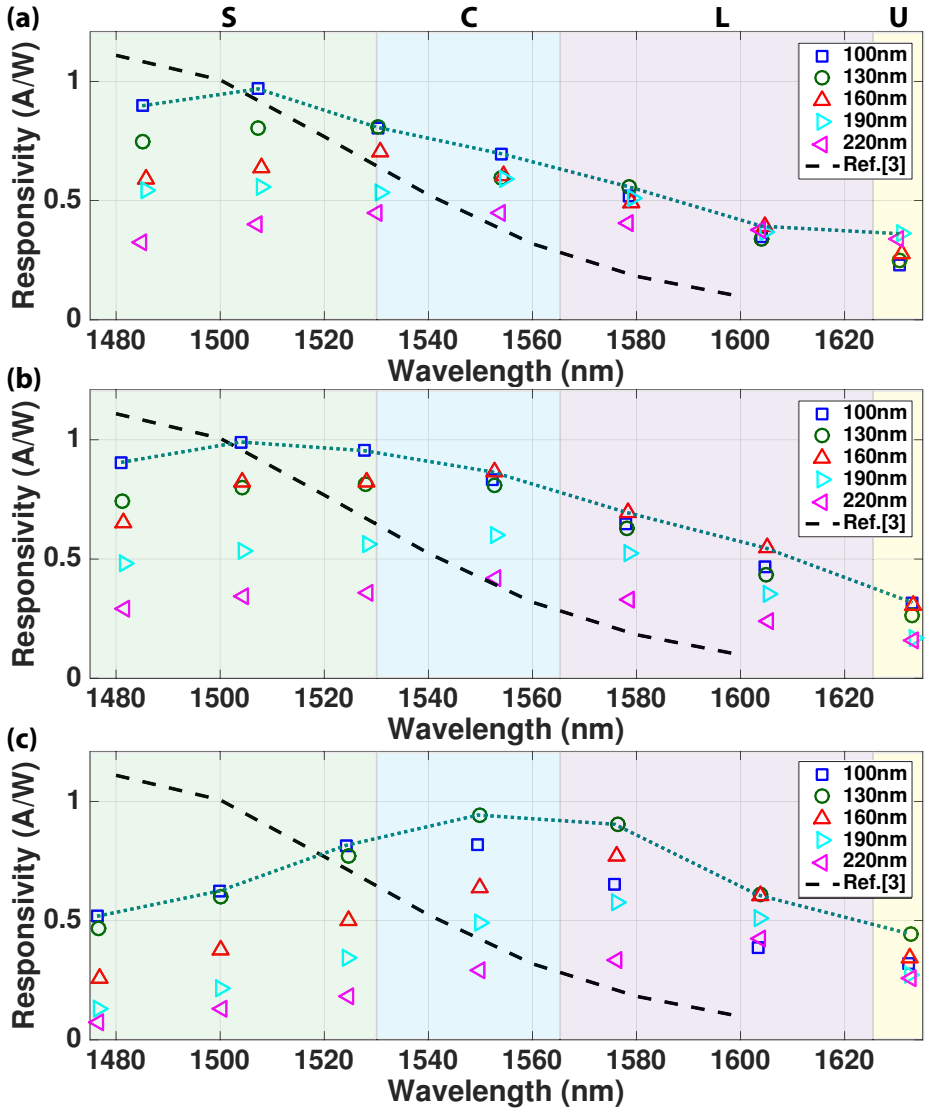

Fig. 3.10: Responsivities of the resonant detectors for different wavelengths and coupling gaps with (a) TE_{11}, $\Delta R_{Si-Ge} = 1.1\mu m$. (b) TE_{21}, $\Delta R_{Si-Ge} = 1.4\mu m$. (c) TE_{31}, $\Delta R_{Si-Ge} = 1.7\mu m$. Responsivity curve (black dashed line) of the evanescent-coupled waveguide detector fabricated on the same wafer is also displayed here for comparison. Figures are shaded to mark different optical communication bands - S (1460-1530nm), C (1530-1565nm), L (1565-1625nm) and U (1625-1675nm).

0.3A/W for wavelengths up to 1630nm. The results agree with our expectation that a broad wavelength range detection within a single device can be achieved. With optimized coupling gap, a responsivity as high as 0.45A/W was obtained for a wavelength around 1630nm for the device with a ΔR_{Si-Ge} of 1.7μm and a coupling gap of

130nm. Responsivities of evanescent-coupled waveguide detector from Ref. [14] are also displayed in Fig. 3.10(a-c) for comparison. We observe a more than four times increase in the responsivities for wavelengths longer than 1580nm by using resonant germanium-on-silicon detectors.

3.3.3 High Speed Testing

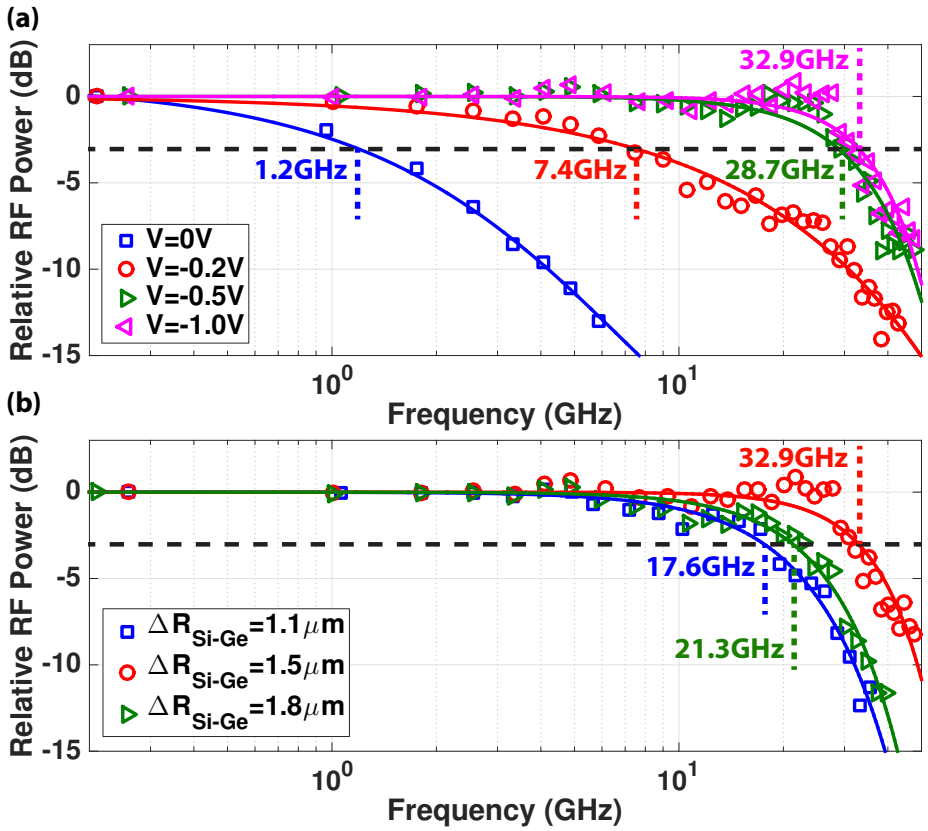

Fig. 3.11: (a) Measured bandwidths with different bias voltages for device of $\Delta R_{Si-Ge} = 1.5\mu$m and gap = 100nm, showing 3dB bandwidth of 32.9GHz for -1V bias voltage. (b) Measured bandwidths of devices with gap=100nm and ΔR_{Si-Ge} sizes of 1.1, 1.5 and 1.8µm at -1V bias voltage, showing bandwidths of 17.6, 32.9 and 21.3GHz respectively.

One of the most important applications of silicon photonics is its ability to transfer a significant amount of data at the same time. Therefore, a high-speed receiver, or detector, is a crucial building block in the system. For the device discussed before, it has a 4.5-µm radius, and the germanium has a thickness of 0.8µm. Its compact size makes it possible to handle high-speed data detection. We investigated the opto-

electric bandwidth to determine the effects of photon lifetime, transit time and RC bandwidth. The opto-electric bandwidth of the detector was measured using the heterodyne laser technique [14]. Fig. 3.11(a) shows measured bandwidths of the device with a ΔR_{Si-Ge} of 1.5μm and a coupling gap of 100nm for an input wavelength around 1528nm under different bias voltages. The bandwidth of the detector is improved from 1.2GHz under zero bias to 32.9GHz under -1V or more bias voltages. Bandwidths for devices with a 100-nm gap and different ΔR_{Si-Ge} sizes are shown in Fig. 3.11(b). For devices with $\Delta R_{Si-Ge} = 1.1$μm and 1.8μm, the measured bandwidths are 17.6 and 21.3GHz respectively, which are limited by the optical bandwidths or the photon lifetime of the cavities (15GHz for $\Delta R_{Si-Ge} = 1.1$μm and 22GHz for $\Delta R_{Si-Ge} = 1.8$μm). However, for the device with $\Delta R_{Si-Ge} = 1.5$μm, the bandwidth is measured to be 32.9GHz, less than the 50GHz optical bandwidth (Fig. 3.9(c) inset) of the device. The difference can be explained by the transit time limitation of the germanium material.

3.4 Applications in Multicasting System

In the previous sections, resonant Ge-on-Si detectors were investigated for full power absorption of input light based on Q-matching. While full power absorption is necessary for applications where a detector acts as a termination for photonic circuits, partial-power selection, as discussed in Chap. 2, is crucial for an optical multicast system. In this section, we will investigate the possibility of using resonant Ge-on-Si detectors for optical multicast applications.

The coupled-mode-theory model for a single 1st-order resonant detector is shown in Fig. 3.12. τ_1 stands for the decay time constant of the cavity due to coupling to the bus waveguide. τ_r represents the decay time constant of the cavity due to loss in the cavity. To simplify the analysis, we ignore the loss contribution of silicon material and assume that the τ_r is only from germanium absorption. The ω_0 represents the cavity resonant frequency; a_1 is the energy amplitude of the cavity, which is normalized so that $|a_1|^2$ stands for the total energy stored in the cavity; and S is the wave amplitude, which is normalized so that $|S|^2$ represents the power. The system can, therefore, be

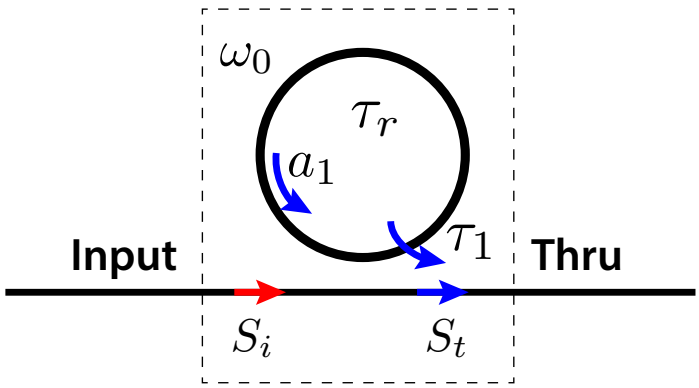

Fig. 3.12: The coupled-mode-theory model for 1st-order resonant detector. τ_1 – decay time constant due to coupling to bus waveguide; τ_r – decay time constant due to loss in the cavity; S_i – input wave amplitude; S_t – thru port wave amplitude; and ω_0 – resonant frequency.

described as

$$\frac{\mathrm{d}}{\mathrm{d}t}a_1 = (j\omega_0 - \frac{1}{\tau_1} - \frac{1}{\tau_r})a_1 - j\sqrt{\frac{2}{\tau_1}}S_i \tag{3.5}$$

$$S_t = S_i - j\sqrt{\frac{2}{\tau_1}}a_1 \tag{3.6}$$

The thru port response can be calculated as

$$T = |\frac{S_t}{S_i}|^2 = \frac{(\omega_0 - \omega)^2 + (1/\tau_1 - 1/\tau_r)^2}{(\omega_0 - \omega)^2 + (1/\tau_1 + 1/\tau_r)^2} \tag{3.7}$$

By comparing the coupled-mode-theory model of a resonant detector to that of a first-order filter (described by Eqn. 2.1 and 2.2), we observe that the transmission response of resonant detector can be achieved by replacing τ_2 (representing the coupling to the drop port) with τ_r in Eqn. 2.3. Under this circumstance, since the drop port is removed, $1-T$ becomes the power absorbed in the resonant cavity. With the assumption that τ_r only accounts for the germanium absorption loss, $1-T$, therefore, represents power absorbed by germanium in the cavity. τ_1 is a measure of the coupling between the cavity and the bus waveguide, which can be freely adjusted by changing the coupling gap size. τ_r, as shown before in Fig. 3.7, can be varied by changing the radius difference between germanium and silicon (ΔR_{Si-Ge}). Therefore, the even-dropping conditions shown in Eqn. 2.6 and 2.7 derived in previous chapters can also apply to the resonant detector case with a simple replacement of τ_2 with τ_r.

Therefore, the conditions for even-power distributions using resonant detectors are

$$\tau_1^{i+1} \cdot \tau_r^{i+1} = \tau_1^i \cdot \tau_r^i \tag{3.8}$$

$$|\frac{1}{\tau_1^{i+1}} + \frac{1}{\tau_r^{i+1}}| = |\frac{1}{\tau_r^i} - \frac{1}{\tau_1^i}| \tag{3.9}$$

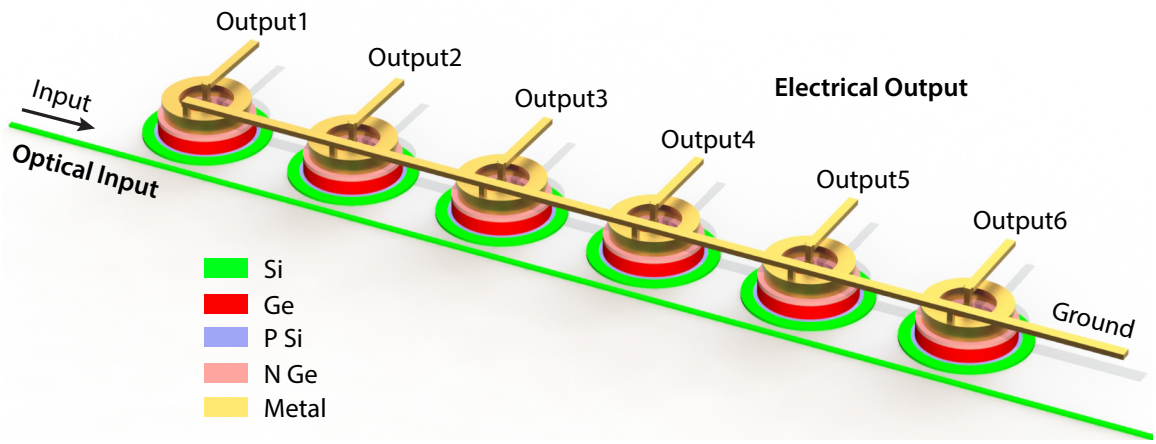

Fig. 3.13: An example architecture of a resonant-detector based multicast system. All the detectors share the same resonant wavelength.

An example architecture of resonant-detector-based multicast system is shown in Fig. 3.13. All the detectors share the same resonant wavelength. Each of them represents a specific destination. Through partially coupling the input light into individual detectors, the input optical signal can be divided equally to each destination and converted to electrical outputs for readout.

However, to implement the resonant detector-based multicast system in real practice, several problems remain to be addressed. First is the measurement of the absorption coefficient of the germanium. This parameter is critical for the estimation of the internal Q-factor of the cavity. Second is the modeling of the internal loss of the resonator. In our model we limited the loss to be only the absorption of the germanium. However, in a fabricated device, intrinsic silicon, doped silicon, doped germanium, and metals could all contribute to the loss in the cavity. A relatively accurate representation of the total loss is required to achieve a multicast function. The third problem is the resonance variations of multiple resonators due to fabrication variations and different mode overlaps with germanium. The variations can be easily compensated by introducing a nearby heater for a thermal tuning of the resonance.

3.5 Conclusion

To summarize, we designed and demonstrated the first resonant germanium-on-silicon detector with evanescent coupling from a silicon bus waveguide on an integrated silicon photonics platform. The compact size (63.6μm^2), low dark current ($\sim$2.03nA), high-responsivity ($\sim$1.04A/W), and high-bandwidth (32.9GHz) of the photodetector enable simultaneous wavelength filtering and power detection, suitable to handle a large data traffic in a WDM network. Moreover, with the resonant nature of the device, the responsivities for wavelength longer than 1580nm are four times better than that of a straight detector fabricated using the same germanium recipe. The detection wavelength range is further extended to a wavelength of 1630nm with >0.45A/W responsivity, making it possible to handle the S-, C- and L-band power detection using the same device. In addition, its potential applications in an optical multicast system were also investigated, leading to a new solution to further simplification of current optical networks.

CHAPTER 4

Microcavity Laser Sources

In this chapter, a robust on-chip Al_2O_3 microcavity design and its application in on-chip laser study are presented. First, the passive microcavity cross-section was investigated using a focus-ion-beam cutting. The resonant cavity modes were then analyzed using a finite-difference bend mode solver for both transverse-electric (TE) and transverse-magnetic (TM) polarizations. Based on the analysis, a set of devices with variations on cavity radius, coupling gap, and film thickness were fabricated. The intrinsic Q-factors for those cavities were extracted and compared with the simulated results. Furthermore, rare-earth-ion dopants such as thulium and ytterbium were introduced to the developed Al_2O_3 microcavities and optically pumped on-chip microcavity lasers at 1.1μm (Yb), and 1.8μm (Tm) wavelengths were demonstrated.

4.1 Microcavity Simulation and Fabrication Flow

In the platform developed in our group, we use silicon nitride (Si_3N_4) and rare-earth-ion-doped Al_2O_3 (Al_2O_3:RE^{3+}) materials to build up laser cavities. The initial demonstration [10] of a standing wave cavity utilized Si_3N_4 as both the guiding and perturbation material for the on-chip mirror implementation while the Al_2O_3:RE^{3+} acted purely as a gain material. However, the gain medium, after the deposition process, would not be localized, which could be detrimental to other nearby active silicon photonic components. Therefore, further generations of laser cavities developed in our group [69] started utilizing thick SiO_2 cladding and deep trenches for gain material isolation from nearby components during the gain medium deposition process. The usage of deep trenches leads to potential applications of using the trench side-wall for mode confinement because of the index difference between the cladding material (SiO_2∼1.44) and the gain medium (Al_2O_3:RE^{3+}∼1.65). By creating a traveling wave microcavity, we can achieve modes with high quality factors (Q-factors) for different wavelength ranges. This chapter will cover details on the on-chip microcavity laser design, ranging from the fabrication flow to laser demonstrations using rare-earth-ions dopants such as thulium and ytterbium.

Fig. 4.1(a) and (b) show schematics of a segmented-nitride inversed-ridge (SNIR) waveguide-based cavity and a trench-based microcavity. The former utilizes the segmented nitride pieces below the Al_2O_3 material to form an inversed-ridge waveguide while the latter confines a resonant mode by a thick SiO_2 wall. Examples of the resonant modes of the SNIR waveguide-based cavity and the trench-based microcavity are shown in Fig. 4.1(c) and (d). We observe that the SNIR waveguide mode is weakly guided by the bottom nitride pieces. Due to a lack of index contrast along the lateral direction, this structure will suffer a large radiation loss when turned at a small radius. The corresponding radiation Q-factors for different bend radii are shown in Fig. 4.1(e). In order to achieve a radiation loss limited Q of 10^7, a radius of ∼8.5mm is required. In contrast, the Q-factors for trench-based cavities with different cavity radii are shown in Fig. 4.1(f). To achieve a Q of 10^7, a radius of only ∼60μm is needed, a 100× decrease compared to a SNIR waveguide-based cavity.

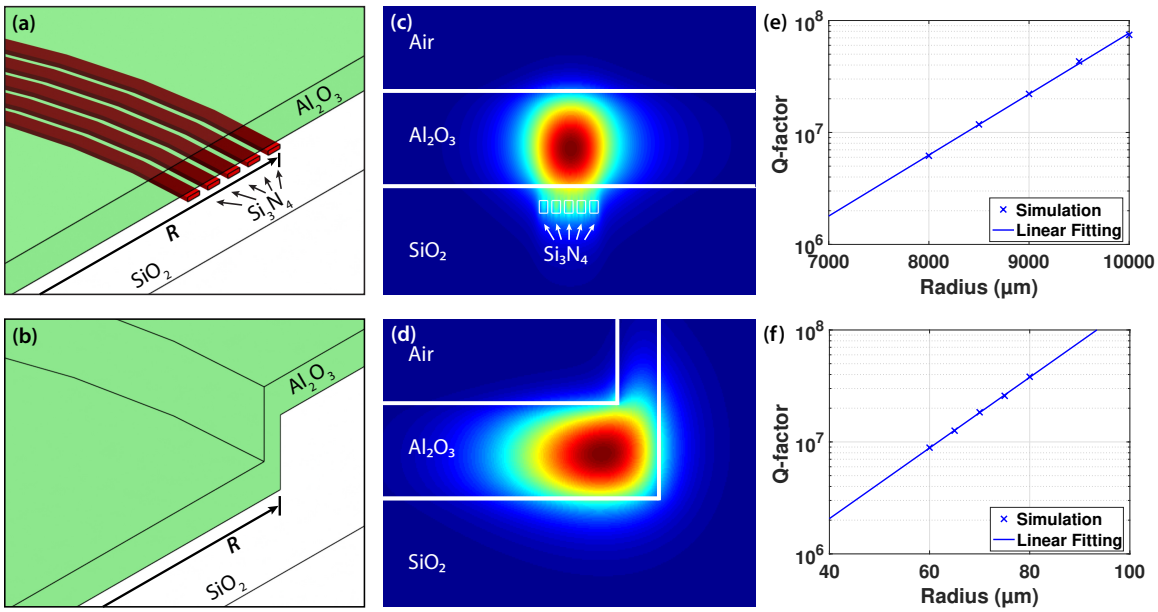

Fig. 4.1: Cross-sections of the (a) segmented-nitride inversed-ridge (SNIR) waveguide-based cavity and (b) trench-based microcavity. Simulated bend modes for (c) SNIR waveguide-based cavity and (d) trench-based microcavity. Quality factors of (e) SNIR waveguide cavities and (f) trench-based cavities with different cavity radii.

However, the above simulations of the trench-based microcavities have several assumptions. As shown in Fig. 4.1(d), the film thickness inside the trench is assumed to be uniform, and the film on the trench wall is assumed to be half of that in the trench. While the cross-sectional model used here is not an exact representation of the real fabricated device, it serves as a guide for the Al_2O_2 cavity design.

The fabrication process to implement the microcavity is shown in Fig. 4.2. We start with a ∼4μm-thick thermal oxide layer on top of a silicon wafer and then deposit a 200-nm-thick PECVD Si_3N_4 film (Nitride1). The Nitride1 is then patterned to form waveguides. After this, a layer of PECVD SiO_2 is deposited and chemical-mechanical planarized (CMPed) to leave a 100nm-thick oxide on top of Nitride1. On top of this oxide layer, another layer of 200-nm-thick PECVD Si_3N_4 (Nitride2) is deposited and patterned, which is followed by a thick (∼5μm) oxide deposition and planarization. The chip is then etched to form deep trenches using Nitride2 as an etch-stop layer and coated with a 100-nm oxide layer. The above steps are done in the CNSE foundry process. The finished chip is then deposited with a thin layer of $Al_2O_3/Al_2O_3{:}RE^{3+}$

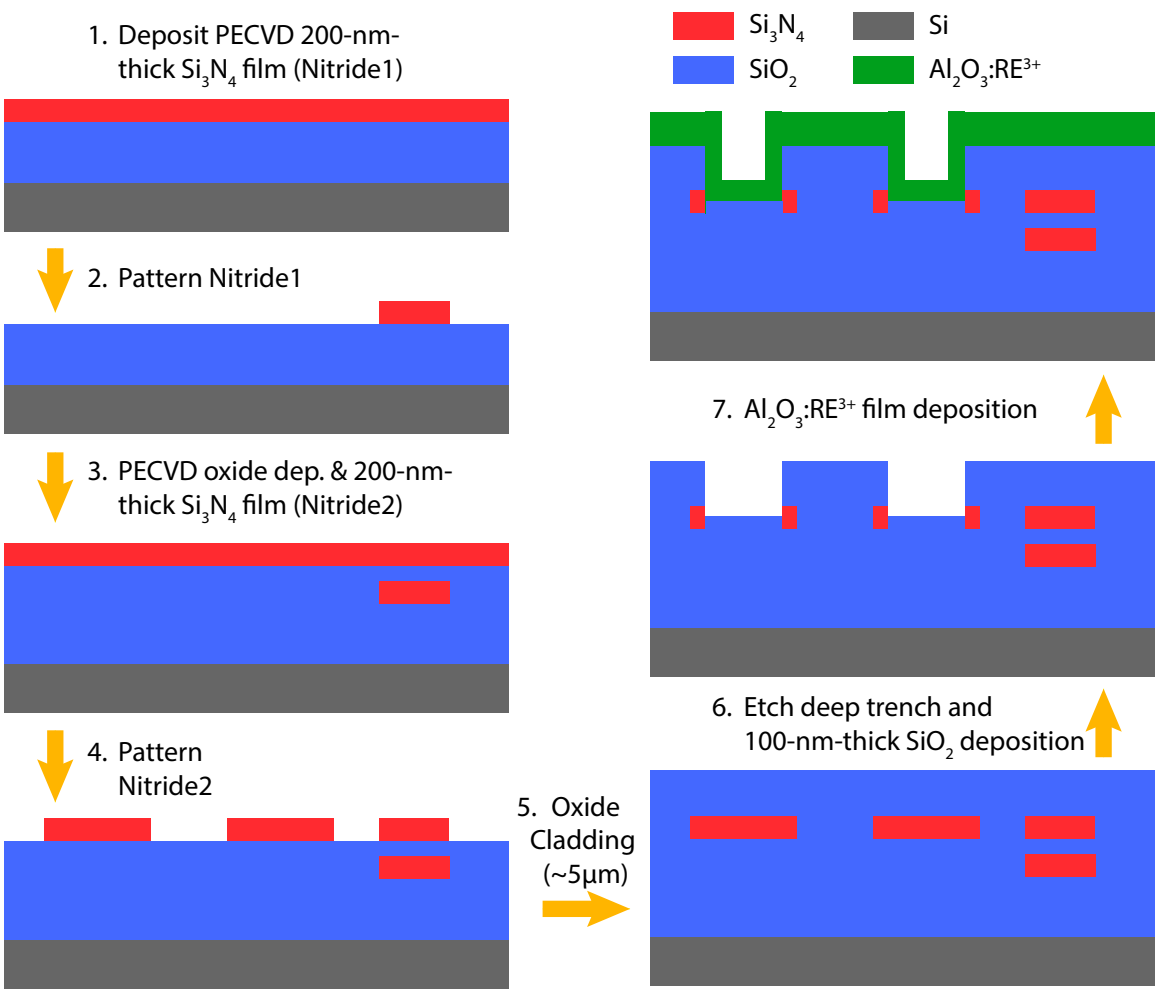

Fig. 4.2: The fabrication flow of on-chip Al_2O_3 microcavities. Step 1-6 are done in CNSE foundry process and step 7 is done in MIT clean rooms.

for passive/laser cavity formations in clean rooms at MIT.

Fig. 4.3(a) shows the sample holder used in the AJA sputtering system. For each deposition, a piece of a silicon wafer with a thick oxide layer on top is used as a witness sample for thickness reference purpose. Samples with microcavity devices are arranged on both sides of the witness sample. To achieve a film with a particular thickness, we calculate the deposition time needed based on the film deposition rate of the machine. Fig. 4.3(b) shows the measured deposited film thicknesses on the witness sample for different distance offsets from the center of the sample holder from one of the depositions performed in the same machine. We observed that the deposition thickness follows a parabolic curve approximately, with a thickness difference of

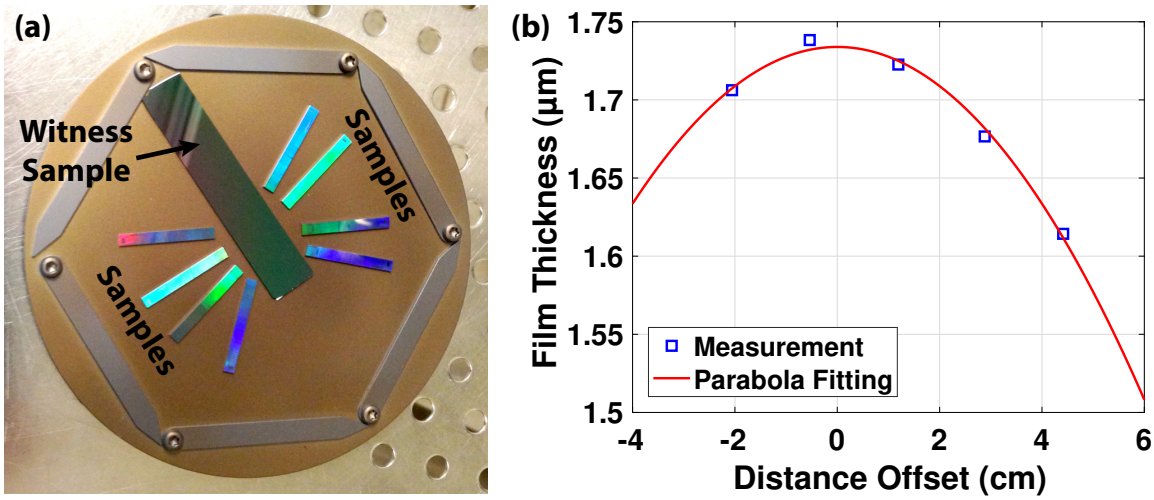

Fig. 4.3: (a) The sample holder used in the AJA sputtering system. (b) Measured thickness variations on the witness sample for different distance offsets from the center of the sample holder from one of the depositions performed in the same machine. The film thickness measurement was taken by Nanxi Li.

around 8% for a 4cm distance offset. The dependence of film thickness on the device location on the sample holder needs to accounted for when calculating the deposition time.

4.2 Passive Microcavity

The gain media used in our process (e.g. Al_2O_3:Er^{3+}, Al_2O_3:Yb^{3+}, and Al_2O_3:Tm^{3+}) all have a relatively low gain on the scale of a few dB per centimeter. Therefore, in order to achieve lasing from those materials, the passive loss of the designed laser cavity needs to be minimized. As we can see from the cross-section in Fig. 4.2, the materials involved in the microcavity laser structures are Si_3N_4, SiO_2, Si, and Al_2O_3. Among them, silicon is the substrate material which is separated from the optical modes by the thick SiO_2 layer, and SiO_2 is lossless over a broad wavelength range of 0.5 to 2.5μm. Therefore, the contributions of these two materials to the passive cavity loss are ignored. The rest of the section will focus on investigating the Si_3N_4 and Al_2O_3 materials to implement a high-Q passive cavity.

4.2.1 Silicon Nitride Loss Test

We first analyze the nitride material loss using a 100-μm-radius Si_3N_4 microring structure shown in Fig. 4.4(a). The width of the bus waveguide (w_1) is selected to be 1.2μm while the width of the microring is chosen to be 1.5μm for single-mode operation in a wavelength range from 1.5μm to 1.6μm. The thickness of the Si_3N_4 layer is 200nm. We select a radius size of 100μm so as to limit the contribution of radiation loss to the measured loss. The radiation Q-factors of a 1.5μm-wide Si_3N_4 cavity for different radii are shown in Fig. 4.4(b). We observe that the radiation loss limits the intrinsic quality factor to 10^8 for 1500nm and 10^6 for 1600nm, respectively. Therefore, if the measured Q-factors are below the simulated ones, they can be treated as closer representations of the Si_3N_4 material loss.

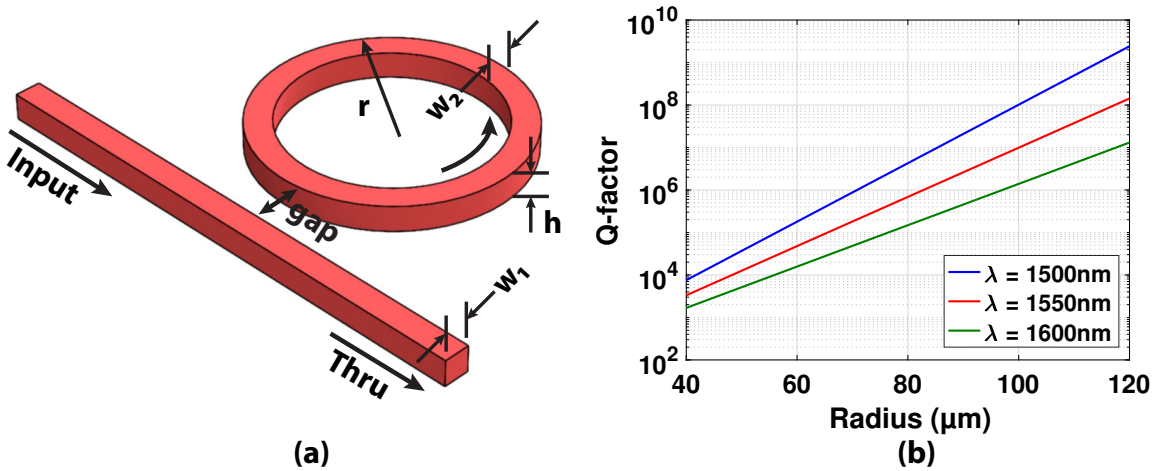

Fig. 4.4: (a) A test structure to analyze the loss of microring-based Si_3N_4 cavities. (b) Radiation loss-limited intrinsic quality factors for different radii of silicon nitride microrings.

Through fitting the transmission spectra of the test structures with different coupling gaps, the loss numbers of the silicon nitride cavities can be extracted. Fig. 4.5(a) shows the measured intrinsic Q-factor in two fabricated wafers (William II and Valerie II) and two different layers of Si_3N_4 (Nitride1 and Nitride2). While Nitride1 and Nitride2 have different loss characteristics, the losses of the same nitride type measured from two separate wafers are mostly the same. For Nitride2, it is also used as an etch-stop layer in our fabrication layer stack and is not optimized for low loss. Therefore, it shows a relatively larger loss than that of Nitride1. We also observe

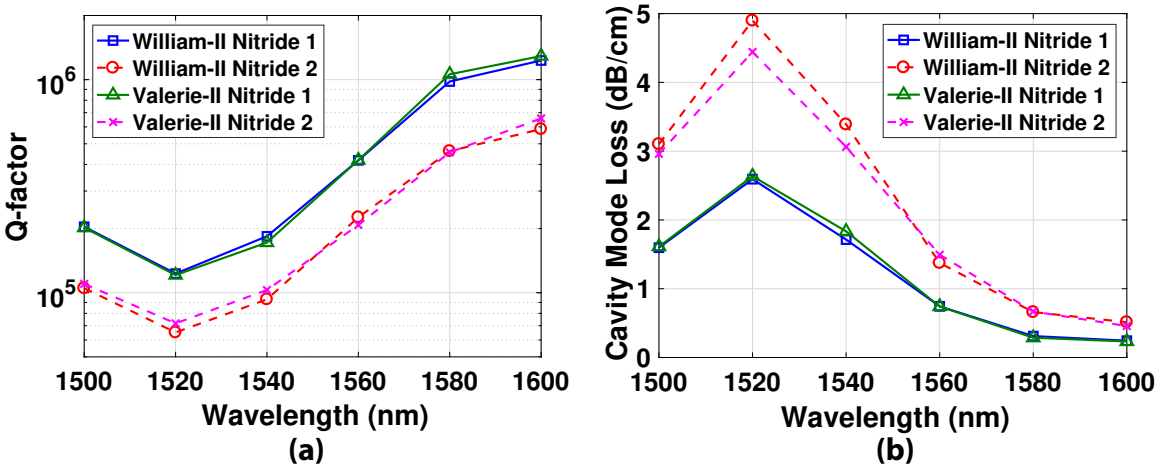

Fig. 4.5: Measured Si_3N_4 losses in two fabricated wafers (William II and Valerie II) and two layers of Si_3N_4 (Nitride1 and Nitride2).

that both nitride layers show absorption peaks around 1520nm, corresponding to the characteristic of silicon nitride material absorption. The loss of the material decreases for longer wavelengths. We also observe that the measured Q-factor for the Nitride1 layer at 1600nm is around 10^6, which is likely limited by the radiation loss of the 100-µm bend radius as shown Fig. 4.4(b).

The measured Q-factor and the propagation loss of the measured mode are linked using the following equations:

$$\alpha = \frac{\lambda_0}{2RQ \cdot FSR(\lambda)} \tag{4.1}$$

$$\alpha_{dB} = 20\alpha \log_{10}(e) \tag{4.2}$$

where R is the cavity radius, λ_0 stands for the resonant wavelength, and $FSR(\lambda)$ represents the free-spectral-range of the microcavity in the same unit as wavelength. The calculated cavity mode losses of the 1.5µm-width nitride waveguide are shown in Fig. 4.5(b). The loss number of Nitride2 is around 2dB/cm while that of Nitride1 is around 1dB/cm at the wavelength of 1550nm. Therefore, both of them are suitable to be used as waveguiding materials and the properties of the modes guided by both layers will be discussed in device designs of the waveguide-coupled Al_2O_3 microcavity.

4.2.2 Passive Al_2O_3 Cavity Measurement

For the Al_2O_3 deposited on the device, we also measured the film loss using Metricon equipment in our lab. The film loss measured is below the equipment accuracy ($<$ 0.2dB/cm) for a wide range of wavelength from 0.65 to 1.64μm, proving the high-quality of the Al_2O_3 material used in the cavity design.

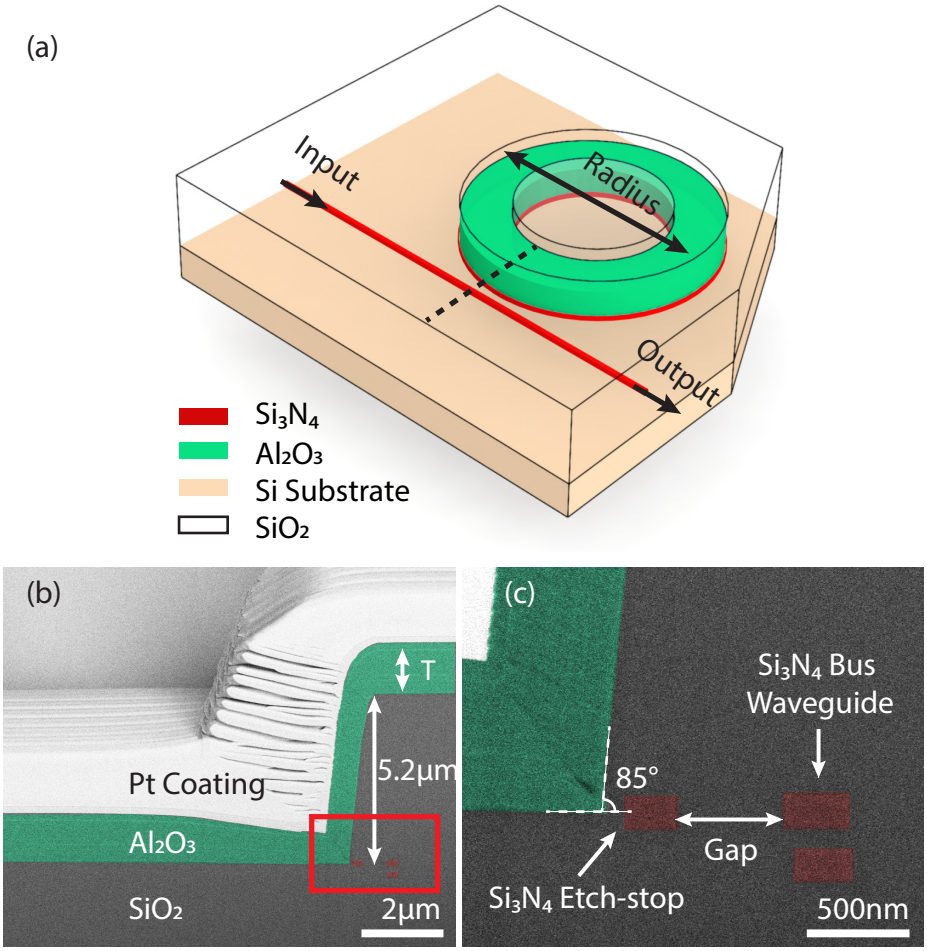

Fig. 4.6: (a) A schematic of the waveguide-coupled trench-based microcavity. (b) A cross-sectional scanning-electron-micrograph (SEM) image along the dotted line in (a). Pt coating is used as a protection layer during the focused-ion-beam (FIB) cutting of the cross section and is not a part of the cavity design. (c) A zoom-in view of the cross-section (marked by red solid rectangle in (b)).

With the developed low-loss material, we utilize a trench-based design to form an on-chip microcavity, as shown in step 7 in Fig. 4.2. For the deposition process, Al_2O_3 will be deposited both inside the trench and on the sidewall. Due to the rotation of

the sample holder and material reflow from high energy ions in the sputtering system, the film thickness on the trench wall is expected to be thinner than that inside the trench.

A schematic of the waveguide-coupled trench-based microcavity is shown in Fig. 4.6(a). To obtain an accurate profile of the resulting microcavity structure, we first deposited a protection layer of platinum (Pt) on the microcavity sample and then cut it along the black dotted line indicated in Fig. 4.6(a) using a focused-ion-beam (FIB). The resulting cross-sectional scanning-electron-micrograph (SEM) image of the microcavity is shown in Fig. 4.6(b). The trench has a depth of around 5.2μm and a trench angle of ∼85°. The image was taken with a sample tilt of 52° to the horizontal plane. Taking the tilt angle into account, we calculated the ratio between the Al_2O_3 film thickness on the side wall and the total deposited film thickness (measured away from the edge of the trench, defined as T in Fig. 4.6) to be 0.44. A zoom-in view of the area enclosed in the red box in Fig. 4.6(b) is shown in Fig. 4.6(c). The bus waveguide is composed of two waveguides of two Si_3N_4 layers. The width of the bus waveguide can be varied to phase-match to the resonant mode inside the cavity. We also notice that a small Si_3N_4 (Nitride2) piece (∼250nm) exists near the SiO_2 trench as a result of the deep trench etching process.

Table 4.1: Approximate material indices used in simulations

Material	Al_2O_3	Si_3N_4	SiO_2
Refractive Index	1.65	1.96	1.44

With the cross section information extracted from Fig. 4.6(b) and (c), we first simulate the mode profiles in the microcavities. The refractive indices used for the materials involved are listed in Table. 4.1. Though for a broad range of wavelength, these materials have a non-negligible dispersion. The parameters used here are still good estimations for simulation purposes. We then calculated the mode profiles for different configurations of the microcavity design. The TE-like mode profiles are shown in Fig. 4.7 for various wavelengths, radii, and film thicknesses. We observe that the cavity designs can support confined modes near the edge of the trench wall. Although the finite film thickness on the trench wall acts as a channel for the resonant

mode to leak out, it is thinner than the total deposited film thickness, making it possible to prevent the resonant mode from leaking out.

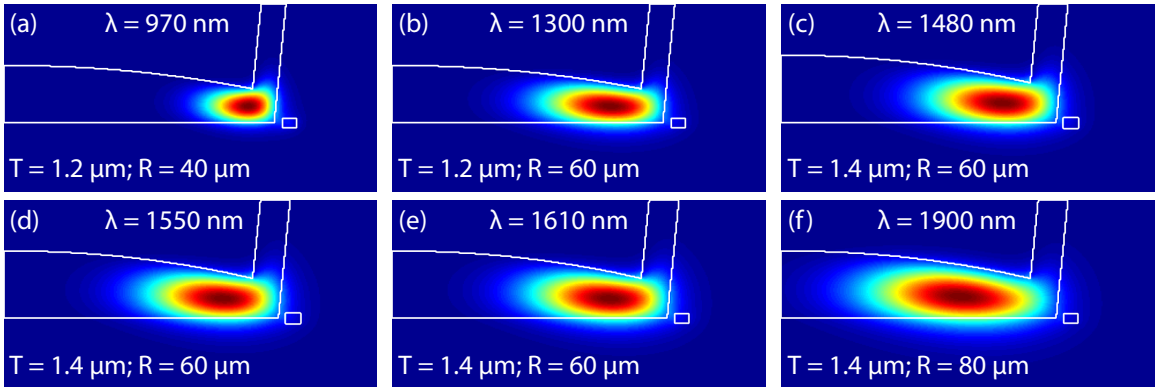

Fig. 4.7: TE-like mode intensity profiles of microcavities with (a) T = 1.2μm, R = 40μm, and λ = 970nm; (b) T = 1.2μm, R = 60μm, and λ = 1300nm; (c) T = 1.4μm, R = 60μm, and λ = 1480nm; (d) T = 1.4μm, R = 60μm, and λ = 1550nm; (e) T = 1.4μm, R = 60μm, and λ = 1610nm; (f) T = 1.4μm, R = 80μm, and λ = 1900nm.

To further characterize the microcavity, we characterized the refractive index of the Al_2O_3 material using the same Metricon tool for a wide range of wavelength. The refractive indices of Al_2O_3 are shown in Fig. 4.8(a). The Al_2O_3 index at a wavelength of 1.60μm is around 1.65, higher than SiO_2. The index contrast allows the microcavity to support resonant modes with different polarizations. Examples of E_x-field of a TE-like mode and E_y-field of a TM-like mode formed inside this type of resonators are shown in Fig. 4.8(b) and (c) respectively. To characterize the modes supported in the resonator, it is crucial to know its effective index. For bend modes in microcavities, their mode profiles will vary slowly with the change of the cavity radius. Here in Fig. 4.8(d) and (e), we show the effective indices for TE- and TM-like modes of a 100μm-radius cavity for different wavelengths and thicknesses, where the effective indices are defined as

$$n_{eff} = \frac{m\lambda}{2\pi R} \tag{4.3}$$

where m is the order of the mode, λ denotes the resonant wavelength, and R is defined as the outer radius of the cavity. This definition serves as an approximation that provides a close representation of a resonant mode of a relatively large-radius cavity. However, even for small radii, it can still serve as a good design reference.

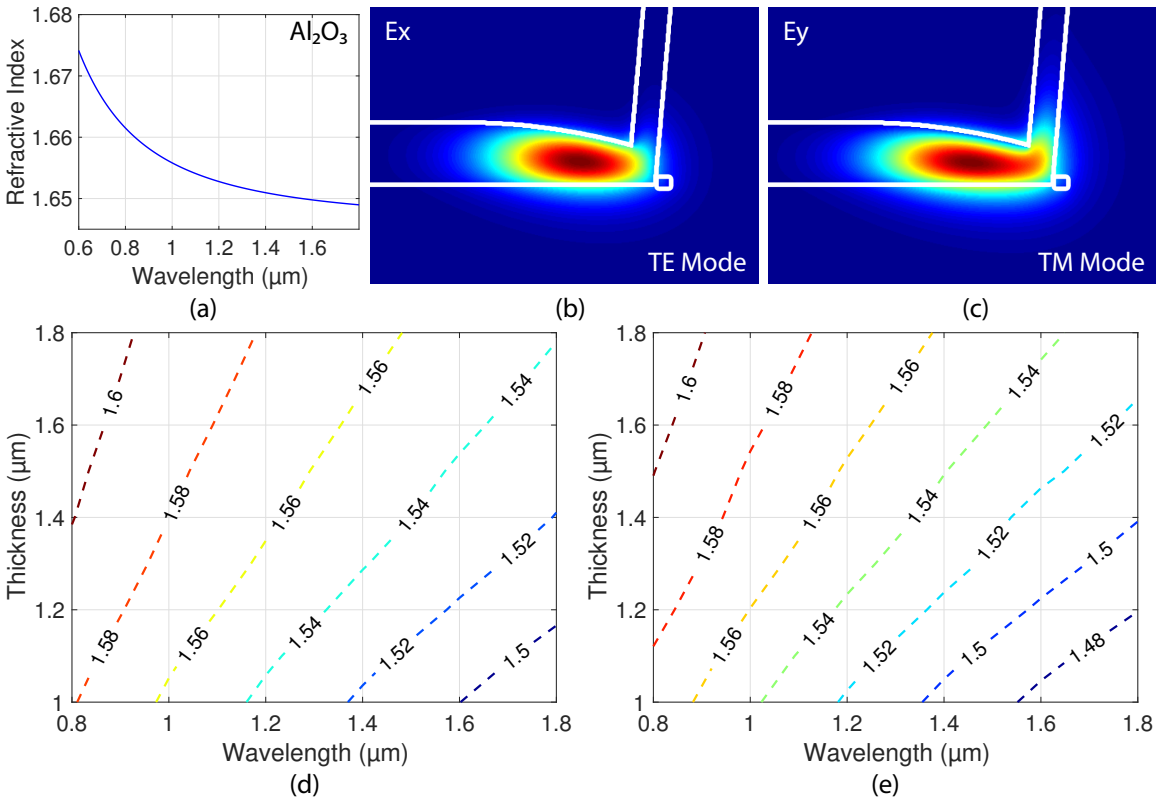

Fig. 4.8: (a) Measured refractive indices of the Al_2O_3 material for different wavelengths. (b) Ex-field of the TE-like mode of the trench-based Al_2O_3 cavity. (c) Ey-field of the TM-like mode of the trench-based Al_2O_3 cavity. (d) Effective indices of the TE-like mode for different wavelengths and film thicknesses. (e) Effective indices of the TM-like mode for different wavelengths and film thicknesses.

In order to make the trench-based Al_2O_3 microcavity an efficient platform for lasing applications, the cavity modes for both pump and signal wavelengths need to have large intensity overlaps with the gain medium. In order to quantify this critical parameter, we use the same confinement factor definition as in Ref. [69]:

$$\gamma_{s/p} = \frac{\int_A I_{s/p} \mathrm{d}A}{\int_\infty I_{s/p} \mathrm{d}A} \approx \frac{\sum_{active(ij)} I_{ij}^{(s/p)}}{\sum_{ij} I_{ij}^{(s/p)}} \tag{4.4}$$

where the subscript s and p represent signal and pump wavelength, respectively. Fig. 4.9 shows the confinement factors of TE- and TM-like modes of different thicknesses and radii for both 980 and 1550nm. We observe that a thicker film, in general, provides a high confinement factor, and is therefore more favorable for laser implementations. However, to achieve a microcavity laser, high confinement factors alone

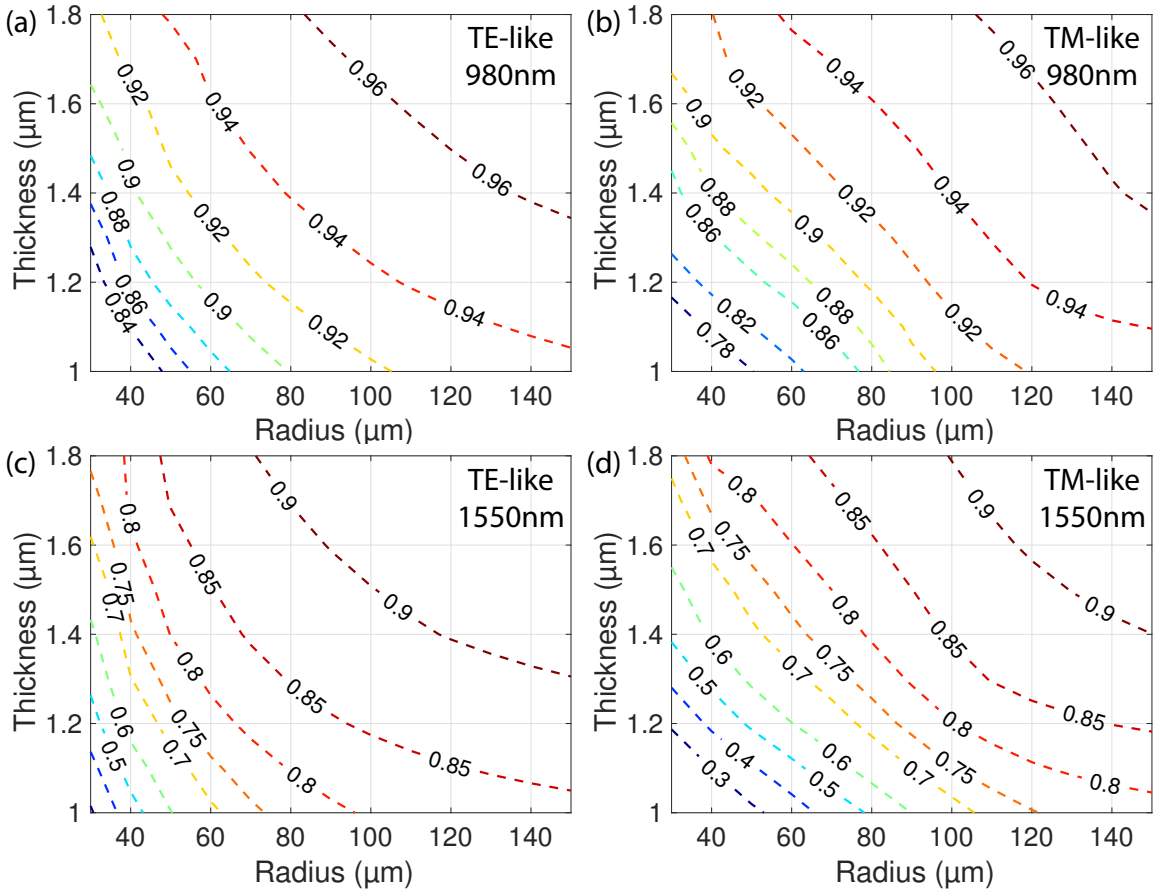

Fig. 4.9: (a) Simulated confinement factors of TE-like mode for different cavity radii and deposited Al_2O_3 film thicknesses at 980nm wavelength. (b) Simulated confinement factors of TM-like mode for different cavity radii and deposited Al_2O_3 film thicknesses at 980nm wavelength. (c) Simulated confinement factors of TE-like mode for different cavity radii and deposited Al_2O_3 film thicknesses at 1550nm wavelength. (d) Simulated confinement factors of TM-like mode for different cavity radii and deposited Al_2O_3 film thicknesses at 1550nm wavelength.

for both signal and pump modes are not enough. Other factors such as the passive loss of the cavity, pump and signal modes coupling to an external waveguide, and signal/pump mode overlap are also crucial for a successful laser demonstration.

Since the trench-based Al_2O_3 microcavity design does not have an inner boundary, multiple higher order modes could also be supported. Therefore, the input light from the bus waveguide is able to excite multiple modes within the cavity at the same time. To efficiently couple the pump light into a particular mode, the bus waveguide needs to be approximately phase-matched to the desired mode. In our design, we use

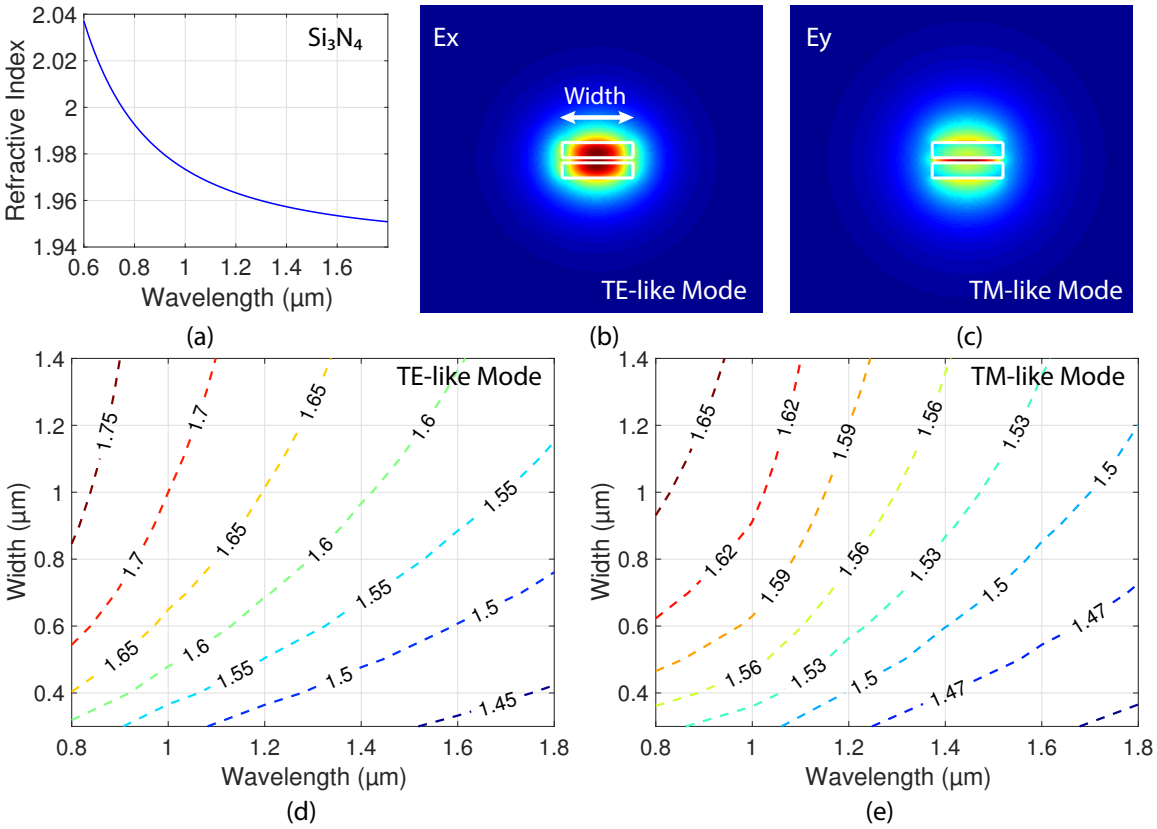

Fig. 4.10: (a) Measured refractive indices of the PECVD Si_3N_4 for different wavelengths. (b) Ex-field of the TE-like mode of the double-nitride waveguide. (c) Ey-field of the TM-like mode of the double-nitride waveguide. (d) Effective indices of the TE-like mode for different wavelengths and waveguide widths. (e) Effective indices of the TM-like mode for different wavelengths and waveguide widths.

both layers of thin silicon nitride (Nitride1 and Nitride2) for waveguide formation. The usage of both layers can provide a highly confined mode to enable a small bend radius for waveguide routing while avoiding the increase of defects in deposited thick nitride films. The measured refractive indices of the PECVD nitride for different wavelengths are shown in Fig. 4.10(a). Typical TE-like and TM-like modes supported by the double-layer nitride waveguide are shown in Fig. 4.10(b) and (c). We also plotted the effective indices for both modes for different wavelengths and waveguide widths in Fig. 4.10(d) and (e), respectively. By matching the effective indices shown in Fig. 4.10(d) and (e) of the bus waveguide with the effective indices shown in Fig. 4.8(d) and (e) of the resonant mode for a particular polarization, wavelength, and film thickness, we are able to select a suitable bus waveguide width to allow an

efficient coupling to the desired mode.

Since the rare-earth-ion-doped glass has a relatively lower gain than III-V materials, in order make a laser out of the microcavity design, achieving a high intrinsic Q-factor microcavity becomes the first priority. To analyze the loss within the cavity, we fabricated a set of devices with variations on bus waveguide width, coupling gap size, bending radius and Al_2O_3 film thickness. We measured the devices with high-resolution (0.1pm) tunable lasers around 980, 1300, 1480, 1550, and 1610nm wavelengths. The input light polarization is controlled with an external polarization controller. For the inverse-taper waveguide coupler used to couple the light of a fiber to the chip or from the chip to a fiber, a transverse magnetic (TM) polarized light couples better than that of the transverse electric (TE) polarization. The power level difference provides us with an effective way to distinguish the two polarizations. For each wavelength, a set of devices with different coupling gaps were fabricated cover the regime where the microcavity is under-coupled. The transmission spectra are then fitted to the coupled-mode-theory model [70].

We first measured a set of devices with a film thickness of 1.16μm. Examples of the measured transmission spectra of a TE-polarized input to a 150μm-radius cavity at wavelengths of 1480 and 1610nm are shown in Fig. 4.11(a) and (b). We demonstrate that the cavity can support a mode with Q-factor $> 1\times10^6$. Intrinsic Q-factors for different radii and wavelengths with TE-polarized input are summarized in Fig. 4.11(c). Guided lines are calculated from a finite-difference bend mode solver under the assumption that only radiation loss exists in the cavity. The measured Q-factors match the simulated ones for small radii where radiation loss is the dominating loss mechanism in the cavity. We also observe that the intrinsic Q-factors increase slowly with the expansion of cavity size for regions where the radiation loss is negligible. The increase can be explained by the overlap between the resonant mode and the trench wall roughness of the cavity. Increasing radius shifts the resonant modes of the cavity inward, leading to less overlap with the trench wall roughness. Therefore, the intrinsic Q-factors continue to increase for large radii. We also investigated TM-polarized modes in the cavity. The transmission spectra examples of a TM-polarized input to a 150μm-radius cavity at wavelengths of 1480 and 1610nm

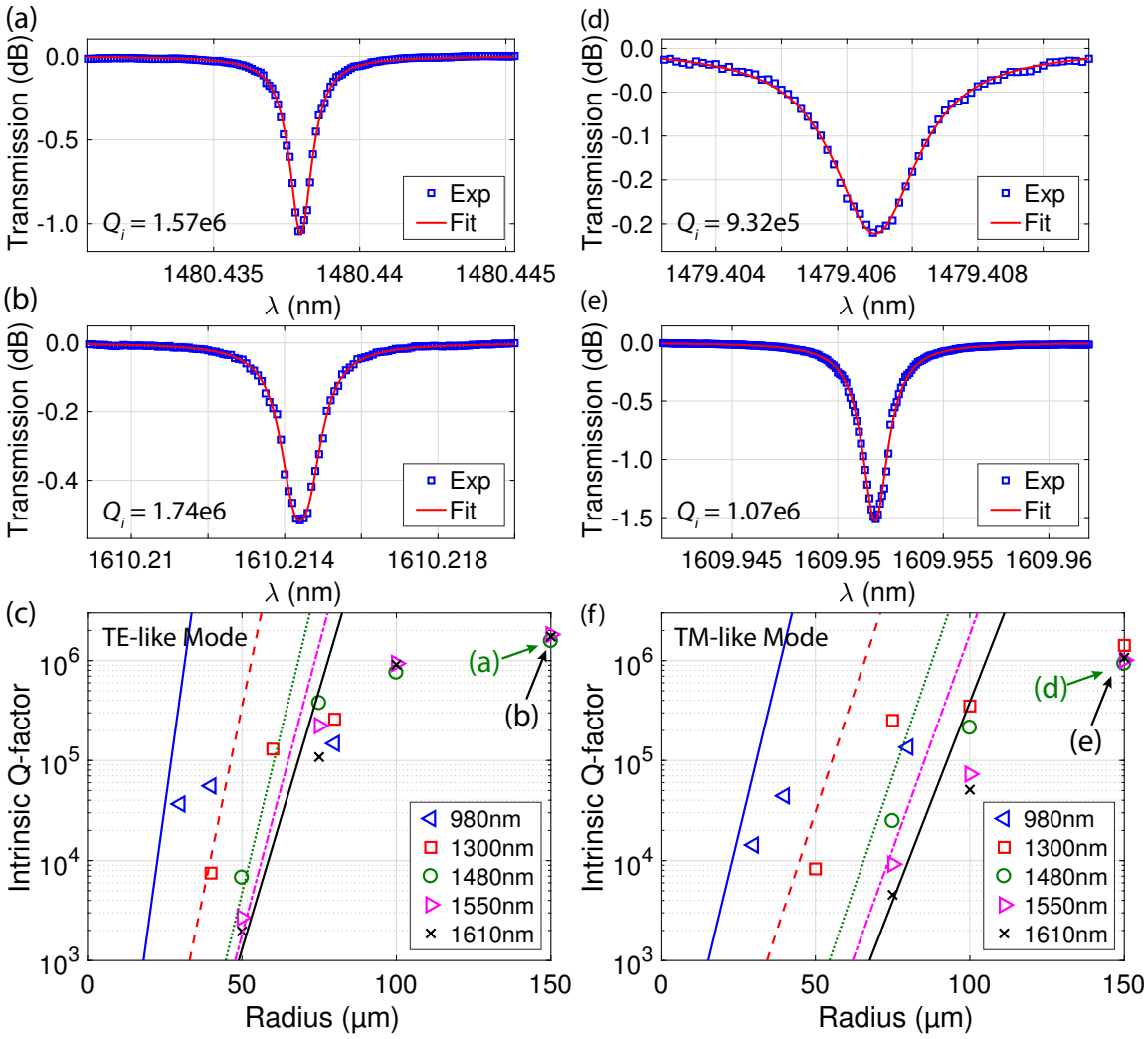

Fig. 4.11: Data shown in the figure were measured with 1.16μm-thick Al_2O_3 film. (a) An example transmission spectrum of a 150μm-radius cavity at 1480nm wavelength with TE-polarized input. (b) An example transmission spectrum of a 150μm-radius cavity at 1610nm wavelength with TE-polarized input. (c) Measured intrinsic Q-factors for different radii and wavelength ranges of TE-polarized inputs (Guide lines are calculated from a finite-difference modesolver.). (d) An example transmission spectrum of a 150μm-radius cavity at 1480nm wavelength with TM-polarized input. (e) An example transmission spectrum of a 150μm-radius cavity at 1610nm wavelength with TM-polarized input. (f) Measured intrinsic Q-factors for different radii and wavelength ranges of TM-polarized inputs (Guided lines are calculated from a finite-difference modesolver.).

are shown in Fig. 4.11(d) and (e). Similarly, intrinsic Q-factors for different radii and wavelengths with TM-polarized input are summarized in Fig. 4.11(f). We observe that TM-like cavity modes show relatively lower Q-factors than those of TE-like

modes. This can be explained by the lower confinement and larger mode overlap with the trench sidewall for the TM-like modes.

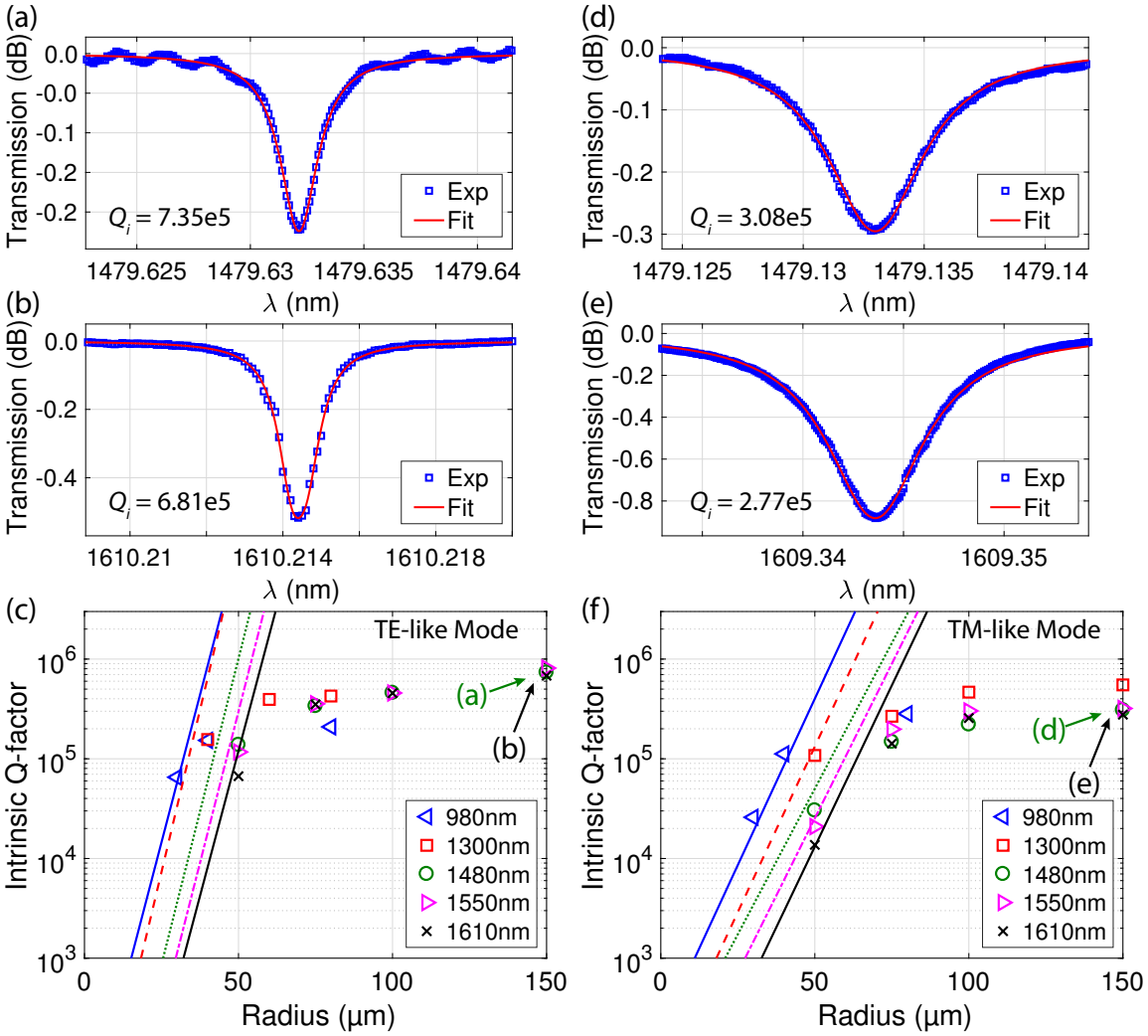

Fig. 4.12: Data shown in the figure were measured with 1.58μm-thick Al_2O_3 film. (a) An example transmission spectrum of a 150μm-radius cavity at 1480nm wavelength with TE-polarized input. (b) An example transmission spectrum of a 150μm-radius cavity at 1610nm wavelength with TE-polarized input. (c) Measured intrinsic Q-factors for different radii and wavelength ranges of TE-polarized inputs (Guide lines are calculated from a finite-difference modesolver.). (d) An example transmission spectrum of a 150μm-radius cavity at 1480nm wavelength with TM-polarized input. (e) An example transmission spectrum of a 150μm-radius cavity at 1610nm wavelength with TM-polarized input. (f) Measured intrinsic Q-factors for different radii and wavelength ranges of TM-polarized inputs (Guided lines are calculated from a finite-difference modesolver.).

We also fabricated another set of devices with a Al_2O_3 film thickness of 1.58μm.

Examples of the measured transmission spectra of TE- and TM-polarized inputs of a 150μm-radius cavity for wavelength 1480 and 1610nm are shown in Fig. 4.12(a-b) and (d-e), respectively. Compared to the Q-factors of the same device but with a thinner film, a thicker film provides a relatively lower intrinsic Q-factor for 150μm-radius devices. The difference is caused by a increased mode overlap with the trench sidewall roughness as a result of mode size expansion. Summaries of the intrinsic Q-factors of TE- and TM-like modes for different radii and wavelengths for the 1.58μm-thick film are shown in Fig. 4.12(c) and (f). We observe that for a small-radius device such as the 50μm-radius device where the intrinsic Q-factor is limited by radiation loss, the thick film provides better intrinsic Q-factors than that of the thin film because of the increase in mode confinement as the film gets thicker. Therefore, to achieve a compact on-chip laser, thicker Al_2O_3 film is preferred.

4.2.3 Discussion

For our current design and fabrication technique, we have achieved a maximum Q-factor around 2×10^6 for devices with a 150μm radius. However, making this micro-cavity design more compact while maintaining a Q-factor on the scale of 1×10^6 scale requires more optimization of the trench wall roughness. For our current fabrication process, the deep trench is fabricated using dry etching with a relatively low-resolution mask. To make the trench wall smoother, a short-time HF wet etch of the device would be helpful.

Another key structural parameter that can be improved is the trench wall angle. In our fabrication, the trench wall angle is estimated to be around 85°. For a small radius device, the resonant mode is pushed toward the trench wall, and the film deposited on the trench wall starts acting as a leaking channel. Through optimizing the trench wall angle toward 90°, a more confined mode for a small-radius device can be achieved, making it possible to further reduce the cavity footprint while maintaining a relatively high intrinsic Q-factor.

4.2.4 Conclusion

To summarize, we demonstrated a simple way to create an on-chip Al_2O_3 microcavity with power input from a nitride waveguide co-fabricated in the same process. The properties of both the microcavity and the nitride bus waveguide were analyzed. We achieved a maximum Q-factor on the scale of $\sim 10^6$ for this type of cavity, making it possible for further development of on-chip microcavity lasers.

4.3 Thulium Laser

Thulium lasers are of significant interest because of their high efficiencies, high output powers and eye-safe emission at wavelengths ranging from 1.7 to 2.2 µm. Important applications of thulium lasers include gas sensing, free space communications, biomedicine, lidar and nonlinear mid-infrared generation [71, 72]. Thus far, 2µm thulium lasers have been developed on a variety of photonic platforms, including bulk crystals [73, 74, 75], glass fibers [76, 77, 78, 79], planar and channel waveguides [80, 81, 82, 83, 84, 85, 86], and whispering-gallery microresonators [87, 88, 89].

Silicon is currently under intensive development as a platform for low cost, energy efficient, and high speed integrated photonic microsystems, especially for the traditional communications wavelength bands around 1.3 and 1.5 µm wavelengths. Recently, however, intensive research has been applied towards extending the operational range of silicon photonic systems beyond 1.5µm for communications, sensing, and advanced metrology applications. In particular, there is a focus on an emerging 2-µm silicon photonics window, motivated in part by the development of low-loss photonic crystal fibers, extended-range silicon detectors, and thulium fiber amplifiers [90, 91, 92].

Since silicon itself is a poor light emitter, compact, efficient and monolithic silicon-based light sources operating near 2µm are desirable. However, despite their high performance in other platforms, and the realization of 1.5-µm erbium- and other rare-earth-doped glass lasers on silicon [93, 10, 11], silicon-integrated thulium lasers are to-date minimally explored. While thulium microlasers have been demonstrated on silicon chips [94, 95], their design required an off-chip fiber for pump coupling and laser emission. However, to implement thulium microlasers within silicon photonic

microsystems, they must be co-integrated with on-chip waveguides and fabricated using silicon-compatible methods.

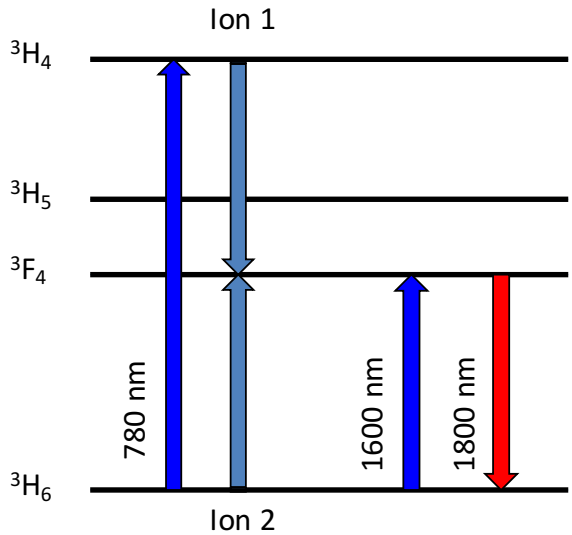

Fig. 4.13: Energy levels of Tm^{3+}.

With the high-Q Al_2O_3 microcavity developed in Sec. 4.2, we first utilize this cavity for on-chip thulium designs. The energy level of Tm^{3+} is shown in Fig. 4.13 [96]. We notice that Tm^{3+} can be pumped at two wavelength regions. One is using a 780nm wavelength pump, taking advantage of the "two-for-one" pumping scheme for high efficiency lasing. Another one is using a 1600nm wavelength pump, achieving a highly efficient pump with in-band absorption and emission while maintaining a large mode overlap between pump mode and lasing mode.

4.3.1 Al_2O_3:Tm^{3+} Deposition

To deposit Al_2O_3:Tm^{3+}, we use an AJA sputtering system with two radio frequency (RF) magnetron sputtering guns. A schematic of the deposition system is shown in Fig. 4.14. The aluminum sputtering gun is operated at a power of 200W, and the deposition pressure is 3mTorr. Two gases – argon and oxygen, are used in the system. The flow rate of argon is kept at 11 sccm, and the oxygen flow rate is manually adjusted from 1.0 to 1.5 sccm to keep the oxygen flow-bias voltage curve at the "knee" point of the hysteresis curve as discussed in Ref. [97]. For oxygen flow that is lower than the "knee" point, the aluminum target will be poisoned, and both

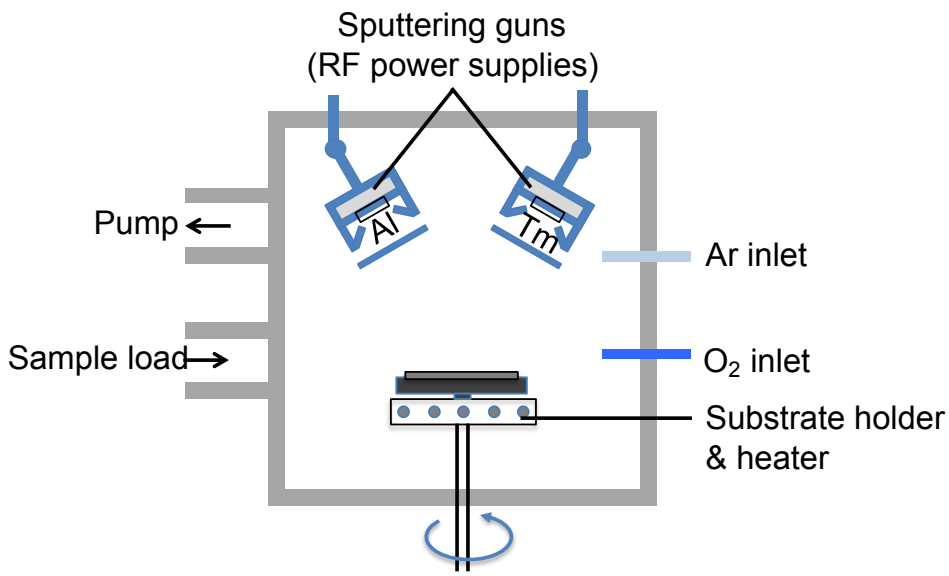

Fig. 4.14: A schematic of the Al_2O_3:Tm^{3+} deposition system (figure created by Prof. Bradley).

the bias voltage and deposition rate will drop sharply.

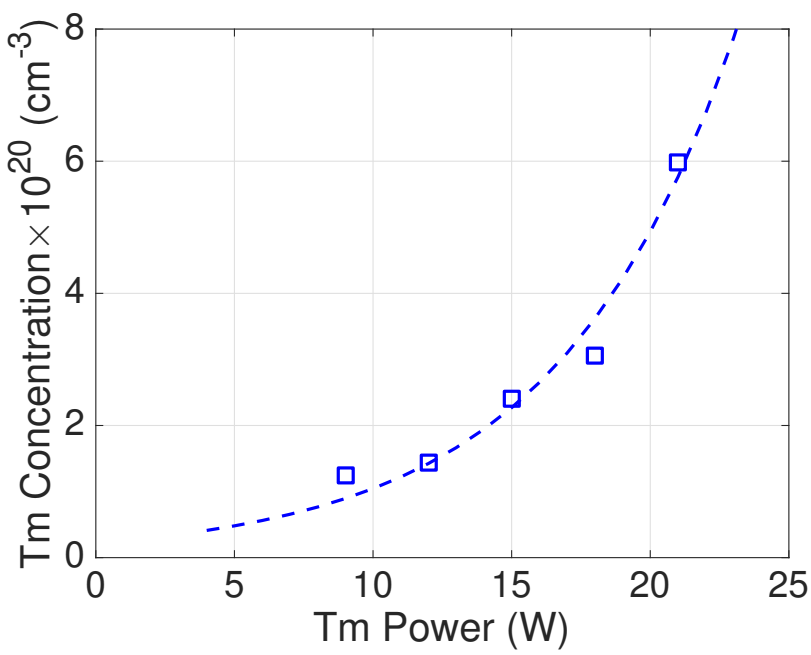

Fig. 4.15: Thulium concentration vs. sputtering power measured by Rutherford backscattering spectrometry (measurement date provided by Prof. Bradley).

To get a high-quality film and calibrate the concentration of the thulium in the Al_2O_3, we kept the substrate temperature at 500°C and determined the thulium

concentrations in the films through Rutherford backscattering spectrometry (RBS). The relation between the thulium concentration in the film and the thulium sputtering power is shown in Fig. 4.15. By adjusting the sputtering power from 9 to 21W, we can vary the thulium concentration in the range of 1 to 6 $\times 10^{20}$cm^{-3}.

4.3.2 Thulium Amplified Spontaneous Emission Spectrum

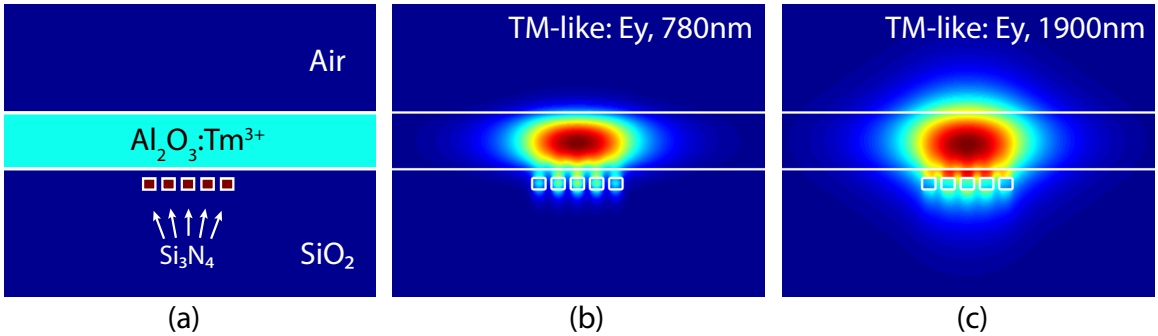

Fig. 4.16: (a) A cross-section of a segmented-nitride inversed-ridge waveguide used for the ASE measurement. (b) Ey component of the fundamental TM-like mode of the waveguide at 780nm wavelength. (c) Ey component of the fundamental TM-like mode of the waveguide at 1900nm wavelength.

In order to achieve an on-chip thulium laser, we first check whether amplified spontaneous emission (ASE) can be observed in a Al_2O_3:Tm^{3+} film. We utilized a structure that was designed as a waveguide loss reference for segmented-nitride inversed-ridge waveguide-based DFB and DBR lasers [98] and deposited a 1.1µm-thick Al_2O_3:Tm^{3+} with a concentration of 2×10^{20}cm^{-3}. The cross-section of the structure is shown in Fig. 4.16(a). Segmented Si_3N_4 pieces with a 200nm thickness were used to create a lateral confinement of guided modes. The TM-like modes of the structure for both 780nm and 1900nm wavelength are shown in Fig. 4.16(b) and (c). Both modes are relatively confined and have large intensity overlaps with the gain medium (Al_2O_3:Tm^{3+}).

Thulium, as mentioned before, can be optically pumped by either 780nm or 1600nm to induce electron transition between energy levels and emit photons for wavelengths around 1800nm. Therefore, when the waveguide structure shown in Fig. 4.16 is pumped at 780nm, it could generate ASE at the other end of the waveguide. The

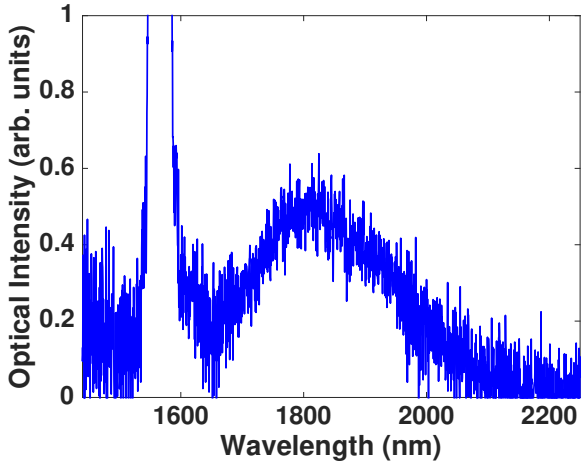

Fig. 4.17: Amplified Spontaneous Emission (ASE) spectrum of segmented-nitride-based channel waveguide pumped at 780nm. The peak around 1560nm is due to 2nd-order grating effect from 780nm pump laser.

measured ASE spectrum is shown in Fig. 4.17. The large peak around 1560nm is due to the second-order grating effect of the optical spectrum analyzer (OSA) from the 780nm pump laser. We observe that thulium has a broad range of ASE from 1.7 to 2.0μm, making it possible to achieve an optically pumped on-chip laser for that range.

4.3.3 Thulium Film Absorption

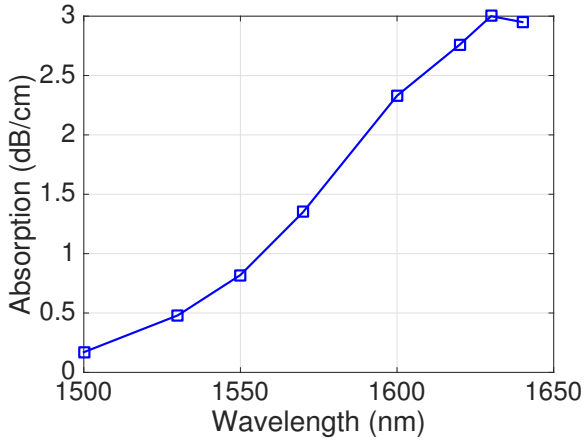

Fig. 4.18: Absorption spectrum in an Al_2O_3:Tm^{3+} film around 1.6μm, showing peak absorption > 1.6μm (data provided by E. Salih Magden).

We also measured the thulium-doped film absorption for a wavelength range from 1.50

to 1.65μm where we can use a tunable laser to analyze the wavelength dependence. The measurement was performed on a chip with a 1.1μm-thick thulium-doped Al_2O_3 layer using the Metricon prism coupling system in our lab at MIT. The optical loss of the thulium-doped film is shown in Fig. 4.18 (measurement performed by Salih). We observe that the absorption of thulium starts around 1.55μm and has a peak around 1.63μm. The broad range absorption of thulium provides us with the possibility to pump thulium laser structures with a wide wavelength range.

4.3.4 Microcavity Designs and Transmission Spectrum

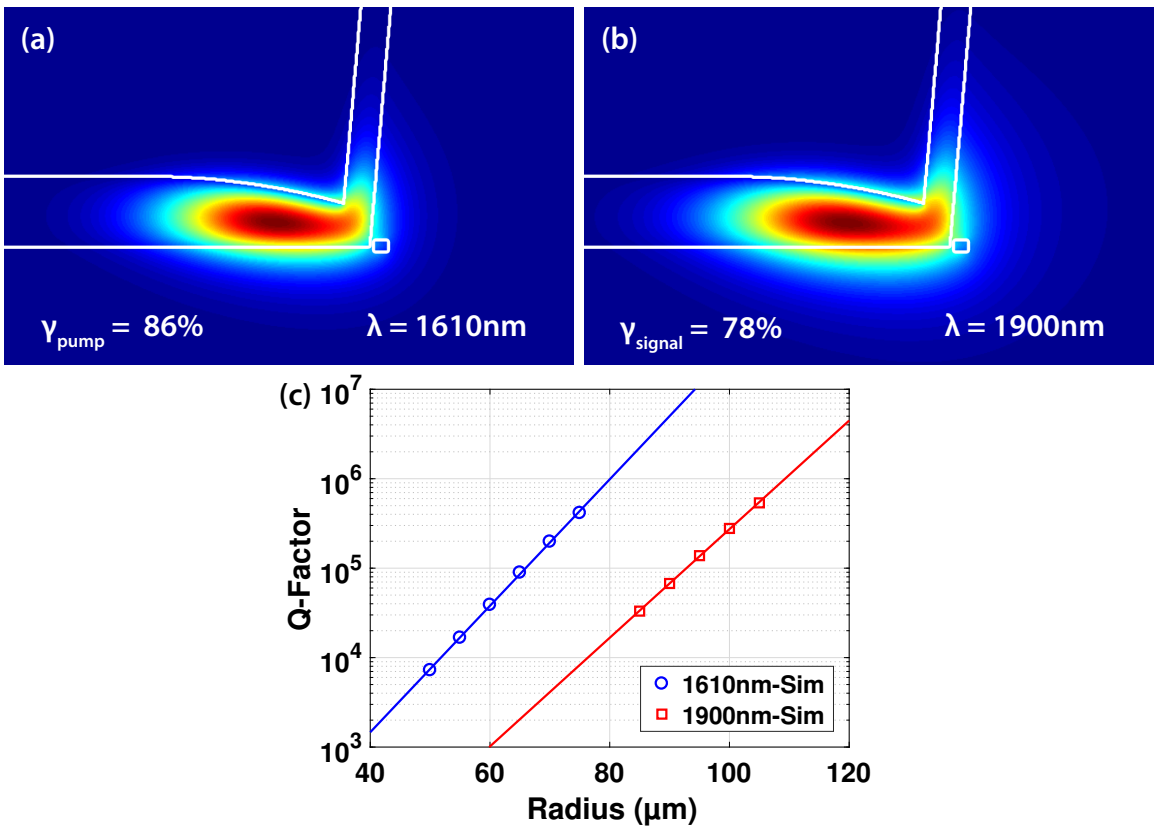

Fig. 4.19: (a) The Ey component of a TM-like trench-based mode for 1610nm with a bend radius of 100μm and a film thickness of 1.5μm, showing a confinement factor of $\gamma_{pump} = 86\%$. (b) The Ey component of a TM-like trench-based mode for 1900nm with a bend radius of 100μm and a film thickness of 1.5μm, showing a confinement factor of $\gamma_{signal} = 78\%$. (c) Calculated radiation-limited Q-factor vs. radius for trench-based modes at both 1610 and 1900nm.

After proving that the Al_2O_3:Tm^{3+} films deposited using the AJA sputtering machine can generate ASEs and can be pumped with both 780 and 1600nm lasers, we

implemented the cavity structure using the trench-based cavity design by changing the cavity dimensions to accommodate both the pump and signal wavelengths. We also selected an Al_2O_3:Tm^{3+} film thickness of 1.5μm to support high-Q modes for both 1.6μm and 1.9μm wavelengths for a relatively small bend radius.

Fig. 4.19(a) and (b) show the calculated TM-like trench-based modes of a 100μm-radius cavity for wavelengths of both the pump (1610nm) and signal (1900nm) wavelengths, respectively. Based on Eqn. 4.4, the confinement factors of the pump (1610nm) and signal (1900nm) modes are calculated to be 86% and 78%, showing relative large overlaps with the gain medium. In order to quantify the similarity between the pump mode and the signal mode, we define the intensity overlap Γ_{sp} as

$$\Gamma_{sp} = \frac{\int_A I_p I_s \mathrm{d}A}{\sqrt{\int_\infty I_p^2 \mathrm{d}A \int_\infty I_s^2 \mathrm{d}A}} \approx \frac{\sum_{active(ij)} I_{ij}^{(p)} I_{ij}^{(s)}}{\sqrt{\sum_{ij} I_{ij}^{2(p)}} \sqrt{\sum_{ij} I_{ij}^{2(s)}}} \tag{4.5}$$

The simulated intensity overlaps between the modes shown in Fig. 4.19(a) and (b) are 93.5%, making it possible to achieve a highly efficient laser. The dependence of radiation limited Q-factors of the trench-based modes (both pump and signal modes) on radius is shown in Fig. 4.19(c). To ensure a sufficient large Q-factor for the signal mode, a radius of 100μm was chosen.

Another crucial parameter in the structure is the bus waveguide width. An efficient laser performance can only be achieved by a Q-matching for the pump wavelength while having a relatively high coupling Q-factor for the lasing wavelength. Therefore, we select a bus waveguide width of ∼915nm to have a proper phase match to the TM-like resonant mode in the cavity for a pump wavelength around 1600nm.

For the thulium concentration, we selected a sputtering power of 15W which, based on the measurement shown in Fig. 4.15, corresponds to a thulium concentration of $2.5\times10^{20}\mathrm{cm}^{-3}$. This concentration is proven later to be high enough to achieve a gain greater than cavity losses and low enough to maintain a low-threshold lasing.

Fig. 4.20 displays a top-view optical microscope image of a fabricated device. We first measure the transmission spectrum of the microcavity structure for mode identification. The transmission spectrum of a microcavity structure with a coupling gap size of 0.9μm over the wavelength range of 1593 to 1615nm is shown in Fig. 4.21(a). We notice that there are three clear resonant modes of different radial orders within

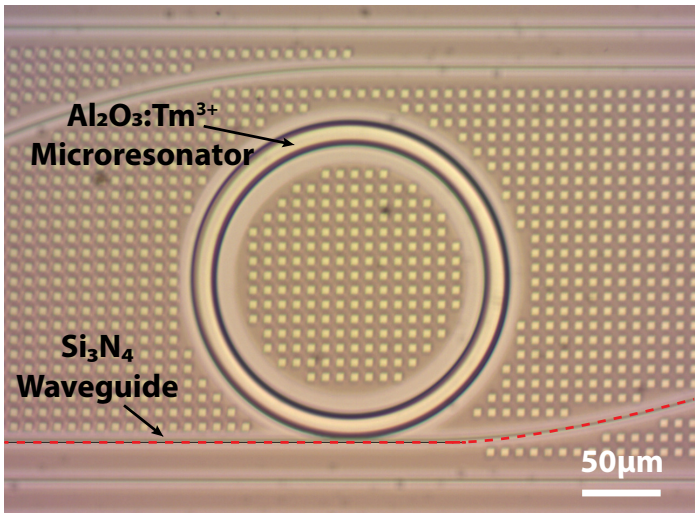

Fig. 4.20: Top-view optical microscope image of a fabricated device, showing the integrated thulium-doped aluminum oxide microresonator and Si_3N_4 bus waveguide (red dashed line).

one free-spectral-range. However, not all the resonances led to low-threshold lasing. Multiple factors affect the lasing behavior, including the quality factor of the microcavity, pump/lasing mode confinement within the gain medium and overlap between pump and lasing mode. In this case, only modes with the same azimuthal order as the one marked with red circle in Fig. 4.21(a) were found to provide lasing behaviors with low thresholds. In Fig. 4.21(b), we show the resonantly absorbed 1608nm pump power vs. microcavity-waveguide gap size. With TM-polarized input light, we observe optimum pump coupling of 95% near a gap size of 0.5μm. However, lasing did not occur for gap sizes <0.7μm. For gap sizes below 0.7μm, the total cavity Q-factor for lasing wavelengths ≥1.8μm becomes too low, leading to a roundtrip net loss or a lasing threshold that is beyond the maximum output power (∼6mW) of the tunable laser utilized in the experiment. We also fabricated another set of devices with undoped Al_2O_3 as a comparison. The measured intrinsic Q-factors of doped and undoped microcavities at wavelengths around 1610nm are 6.8×10^4 and 4.3×10^5, respectively. The former is determined by the rare-earth-ion absorption while the latter is mostly limited by roughness on the trench wall, as discussed in Sec. 4.2.

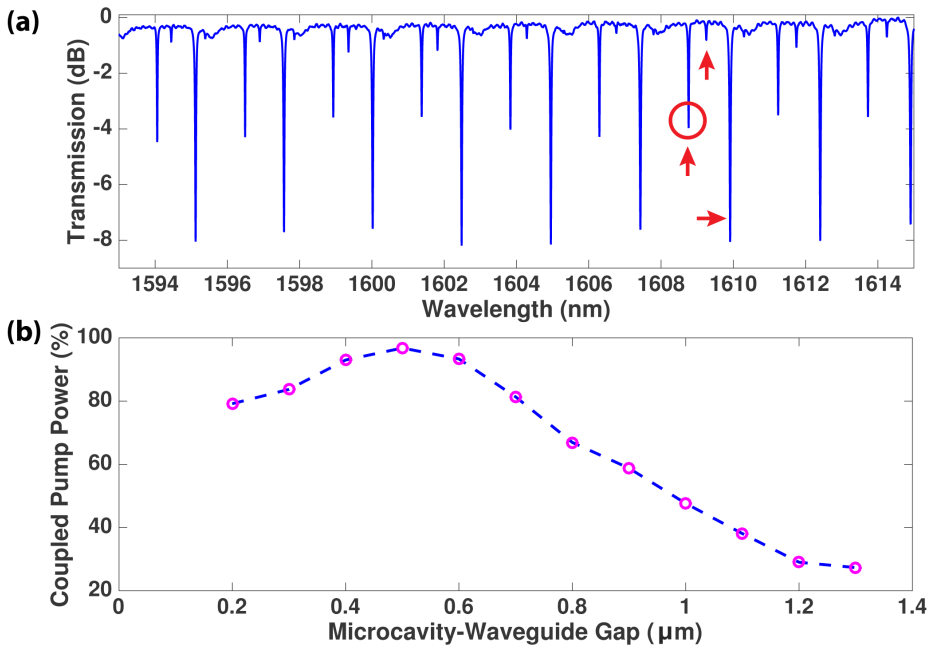

Fig. 4.21: The TM-polarized transmission spectrum for a device with gap 0.9μm over the wavelength range 1593nm to 1615nm, showing three clear resonant modes of different radial orders (marked by red arrows) within one free-spectra-range. The mode that leads to low threshold lasing is marked with a red circle. (b) Coupled pump power for the pump mode circled in (a) in Tm-doped microcavities with a bus waveguide width of 915nm and microcavity-waveguide gap sizes ranging from 0.2μm to 1.3μm. Maximum coupling occurs at a gap near 0.5μm when the internal and external Q-factors of the resonator are matched.

4.3.5 Lasing Spectrum

For the microcavity laser characterization, we utilized the experimental setup shown in Fig. 4.22. We coupled pump light from a narrow linewidth (100kHz), tunable (1500-1625nm) Agilent/Keysight laser to a polarization controller to adjust the input light to TM polarization, and onto the chip via a tapered fiber. Due to the degeneracy of the clockwise (CW) and counter-clockwise (CCW) modes inside the cavity, lasing occurs in both directions. Therefore, we coupled the laser output in the bus waveguide off-chip from both sides using tapered fibers, followed by WDMs to separate the input/residual pump power, and then collected it at optical spectrum analyzers (OSAs) on both sides of the setup. We also measured residual pump power using an optical power meter as a way to track the wavelength difference between the input light and the resonance of the cavity.

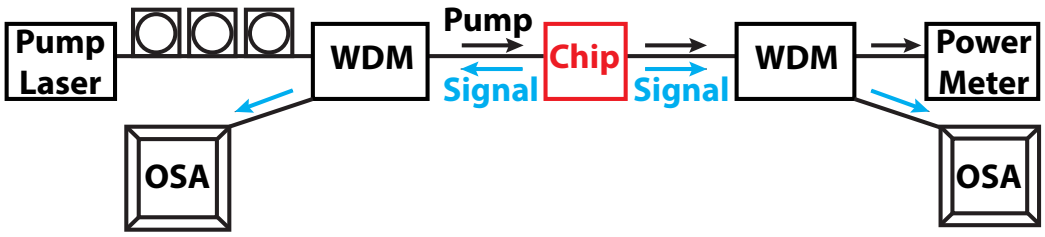

Fig. 4.22: Experimental setup used for Tm-doped microcavity laser measurement. Tunable laser pump light is coupled into the chip through a polarization controller and a 1.6/1.9μm fiber wavelength division multiplexer (WDM). The laser output is measured at the optical spectrum analyzer (OSA) on bth sides of the chip.

We pump the designed laser cavity at the resonant wavelength marked with red circle in Fig. 4.21. Fig. 4.23 shows the lasing spectra of the devices measured from one of the OSAs with microcavity-waveguide gap sizes ranging from 0.7μm to 1.3μm. Multimode lasing and laser modes spanning from 1.8μm to 1.9μm are observed. The devices tend to lase at longer wavelengths for larger gap sizes. This trend can be explained by the interplay of multiple factors, including the gap size and wavelength dependence of the loaded cavity Q-factor; the shape of the thulium emission spectrum with its peak near 1.8μm; and the blue-shifted Tm^{3+} absorption spectrum with respect to the emission spectrum. For smaller gap sizes (and longer wavelengths), the cavity modes have a greater coupling strength and lower Q-factor (higher roundtrip loss), making the microcavity more likely to lase on higher gain modes near 1.8μm. For larger gap sizes, the Q-factor of all cavity modes increases (roundtrip loss decreases). Thus the laser output shifts to longer wavelengths where the Tm^{3+} absorption is lower and population inversion is more easily achieved. This trend indicates that by increasing the gap width beyond 1.3μm, longer wavelength lasing could possibly be achieved. Finally, by adding grating features [99] and asymmetry to the cavity, single-mode or directional lasing [100, 101, 102] can also be achieved.

We also calibrated the setup loss and power coupling efficiency of fiber-to-chip systems. We observed the highest laser output power when resonantly pumping at a wavelength around 1608 nm, near the peak of the thulium ion $^3H_6 \rightarrow ^3F_4$ absorption cross-section. Fig. 4.24(a) shows the total (double-sided) on-chip laser power as a function of on-chip pump power for different pump wavelengths and a gap of 0.9μm.

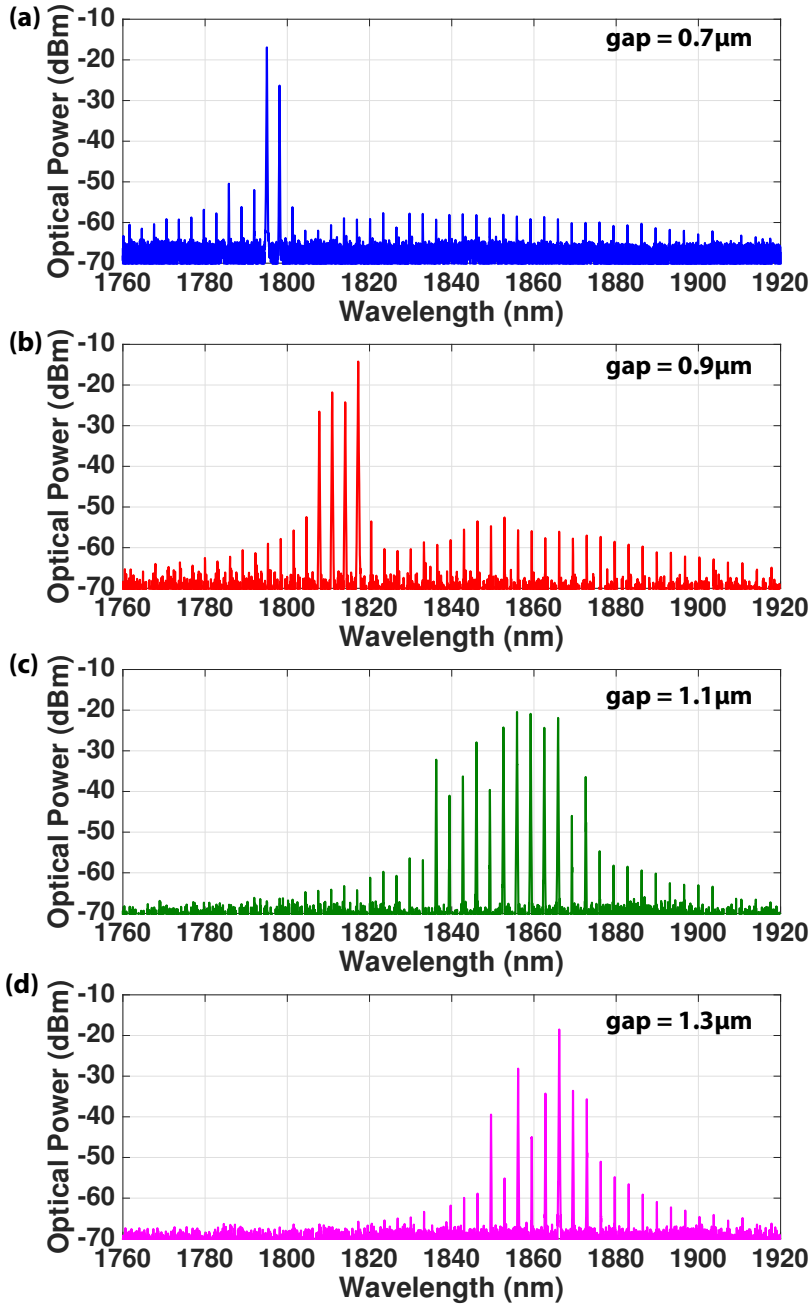

Fig. 4.23: Laser emission spectra measured from one of the OSAs under 1608nm pumping and microcavity-waveguide gaps of (a) 0.7μm, (b) 0.9μm, (c) 1.1μm, and (d) 1.3μm from one side of the chip, showing a shift of lasing signals to longer wavelengths with the increase of microcavity-waveguide gap size.

While similar lasing thresholds were achieved for pump wavelengths from 1594nm to 1614nm, pumping around 1608 nm shows the highest slope efficiency. Fig. 4.24(b) shows the lasing thresholds and double-sided slope efficiencies under 1608-nm pump-

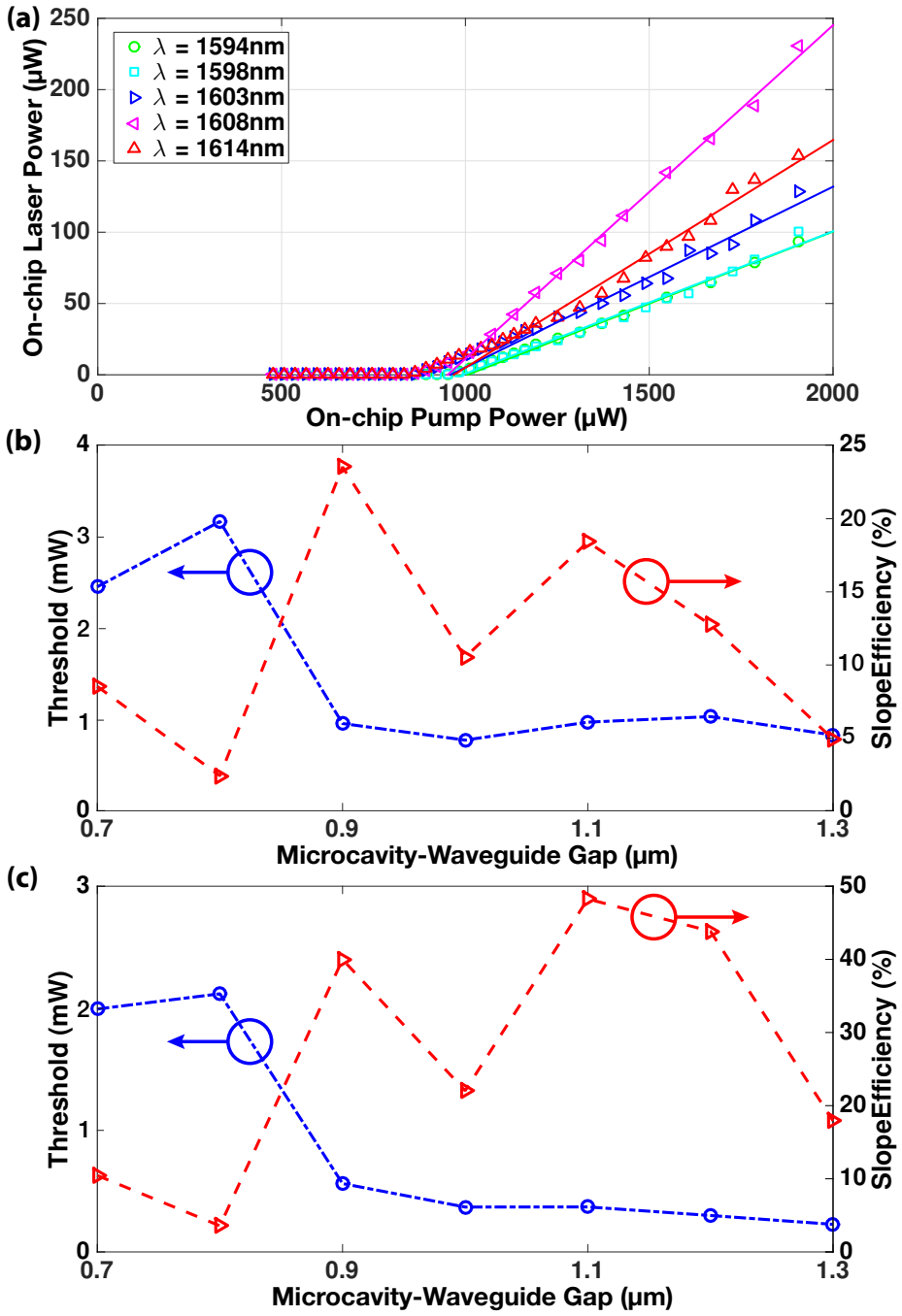

Fig. 4.24: (a) On-chip laser power a function of on-chip pump power for different pump wavelengths for a device with 0.9μm gap size, showing highest-efficiency lasing and output power >200μW when resonantly pumped at 1608nm. (b) Lasing thresholds and slope efficiencies with respect to on-chip pump power for different microcavity-waveguide gap sizes. (c) Lasing thresholds and slope efficiencies with respect to absorbed power for different microcavity-waveguide gap sizes.

ing with respect to microcavity-waveguide gap sizes. A double-sided slope efficiency as high as 23.5% was observed for gap size of 0.9μm and threshold as low as 773μW was achieved with 1.0μm gap size with respect to pump power coupled into the Si_3N_4 bus waveguide. Accounting for the absorbed pump power for different microcavity-waveguide gap sizes shown in Fig. 4.24(c), we determine a maximum double-sided slope efficiency of 48% with respect to the cavity-coupled pump power for the laser device with 1.1μm microcavity-waveguide gap size. We observed a minimum threshold of 226μW vs. absorbed pump power at the largest gap size of 1.3μm, where the total cavity Q-factor is the highest.

4.3.6 Pumping with a 780nm Laser Diode

Thulium can also be pumped around wavelength 780nm to achieve lasing. The efficiency of the laser can possibly be even higher with the "two for one" excitation via Tm^{3+}-Tm^{3+} ion cross-relaxation [73] while the cost of the pump laser can be much lower using low-cost 780-nm pump diodes available in the market. Motivated by these advantages, we also investigated the microcavity laser performance under a 780nm diode pump.

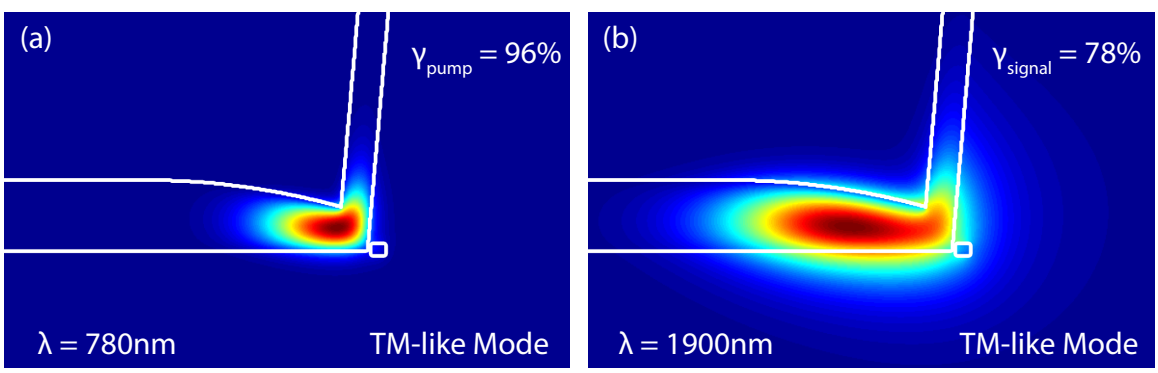

Fig. 4.25: (a) The Ey component of a TM-like trench-based mode for 780nm with a bend radius of 100μm and a film thickness of 1.5μm, showing a confinement factor of $\gamma_{pump} = 96\%$. (b) The Ey component of a TM-like trench-based mode for 1900nm with a bend radius of 100μm and a film thickness of 1.5μm, showing a confinement factor of $\gamma_{pump} = 78\%$.

The biggest disadvantage of pumping the microcavity at 780nm comes from the low intensity mode overlap between the pump (780nm) and signal (1900nm). The profiles of the TM-like modes for both 780 and 1900nm are shown in Fig. 4.25(a) and

(b). While compared to the pump mode at 1610nm shown in Fig. 4.19(a), the size of the pump mode at 780nm becomes much smaller, resulting in an intensity overlap of 59.1% with the lasing mode at 1900nm, much lower than the 93.5% achieved between 1600nm and 1900nm modes. In order to couple 780nm pump power into the microcavity, the bus waveguide width was changed to 335nm to have a better phase-matching between the bus waveguide mode and the microcavity mode at 780nm.

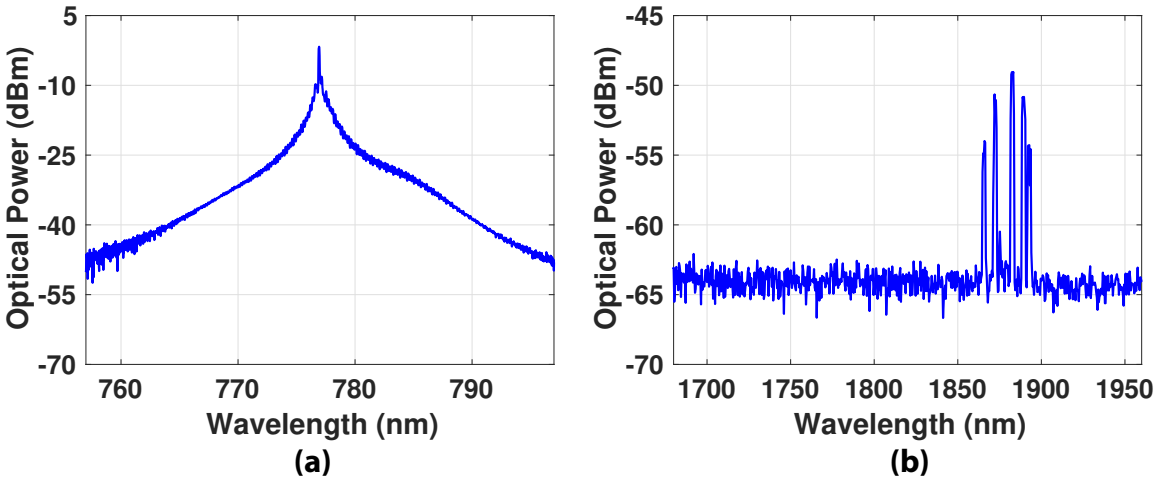

Fig. 4.26: (a) Spectrum of the 780nm pump diode. (b) Lasing signal of trench-based thulium microcavity laser when pumped with 780nm laser diode.

Due to the lack of a convenient tunable laser source, we utilized a power controllable (maximum output power of 200mW) 780nm laser diode as a pump source. The spectrum of the 780nm pump diode is shown in Fig. 4.26(a). We observe that the laser has a relatively wide spectrum with a center wavelength around 778nm. Fig. 4.26(b) shows the spectrum of trench-based thulium microcavity laser obtained from an optical spectrum analyzer when pumped with a 780nm laser diode. We observed lasing signal around 1880nm, proving the possibility of using pump around 780nm to achieve optically pumped thulium lasers.

However, at the stage of this thesis, we do not have a 780nm tunable laser with fine tuning resolution. Therefore, it is difficult to measure the threshold and slope efficiency of the 780nm-pump thulium laser. From the mode simulation, we can roughly estimate that the efficiency of this laser would be lower than that of the 1600nm-pumped one due to the decrease of mode overlap between pump and signal

modes. In this section, we only analyzed the TM-like mode with 1.5μm-thick film for a 100-μm-radius cavity as a proof-of-concept for 780nm-pumped thulium laser. Further optimizations on film thickness, bend radius, and modes with different polarizations could lead to an improved pump-to-signal mode overlap, therefore, improving the efficiency of the design. In addition, a better overlap may also be achieved by using high-order modes supported in the cavity at the pump wavelength.

4.3.7 Conclusion

In this section, we discussed the deposition method of Al_2O_3:Tm^{3+} films and presented several characterization methods of the films. By combining the reliable deposition method with the robust microcavity design, we demonstrated low-threshold and high-efficiency thulium-doped microcavity lasers that are monolithically integrated on a silicon photonic chip. The lasers have thresholds as low as 773 (226)μW and slope efficiencies of up to 23.5% (48%) vs. on-chip (absorbed) pump power. By changing the waveguide-microcavity gap and resonantly pumping at 1608nm, we show multimode lasing in the range of 1.8-1.9μm. In the future, optimizing the Tm^{3+} concentration, coupling strength, and cavity design can lead to even greater efficiencies, emission over a wider wavelength range across the thulium broad gain spectrum (∼1.7-2.2μm), single-mode operation and directionality. In addition, a thulium microcavity laser with 780nm-diode pump was also investigated and demonstrated. These results show integrated thulium lasers to be of interest as highly efficient monolithic light sources for emerging silicon-based photonic microsystems.

4.4 Ytterbium Laser

The CMOS-compatibility of silicon photonics enables low-form-factor and low-cost integrated optical circuits. Due to these advantages silicon photonics is having a large impact on transceiver technology and new applications such as optical interconnects [14, 15], sensors [103, 104] and quantum computation [105] are on the horizon. The combination of biomedical sciences with silicon photonics offers compact and packaged devices at a low cost for sensing applications where large equipment was previously required. In order to achieve a high-sensitivity detection of small biological particles,

both passive high-quality factor (Q-factor) cavities [106] and active laser cavities [107] have been extensively investigated. Active laser cavities are preferred for their narrow linewidths. Previously, microtoroid [107] or microsphere [108] laser cavities have been demonstrated as promising platforms for bio-sensing applications. However, such microcavity configurations require external optical fibers for pump power input and laser output coupling, which limits their CMOS compatibility and integration within silicon photonic systems.

Trench-based microlasers co-integrated with silicon nitride waveguides developed in previous sections can resolve the incompatibility and provide a mechanically stabilized system. The bus waveguide is fabricated near the trench-based cavity for both pump power input and laser output. The coupling area is naturally isolated from the cavity with SiO_2 cladding and the cavity is, by itself, a reservoir to hold and interact with nanoparticles. Reducing the size of the cavity while maintaining lasing behavior will not only enable denser integration using state-of-art foundry processes but also improve the detection sensitivity [104]. Since water is widely used in bio-sensing applications, lasers with longer wavelengths will suffer from a high absorption. Therefore, a compact laser with relatively short wavelength is required.

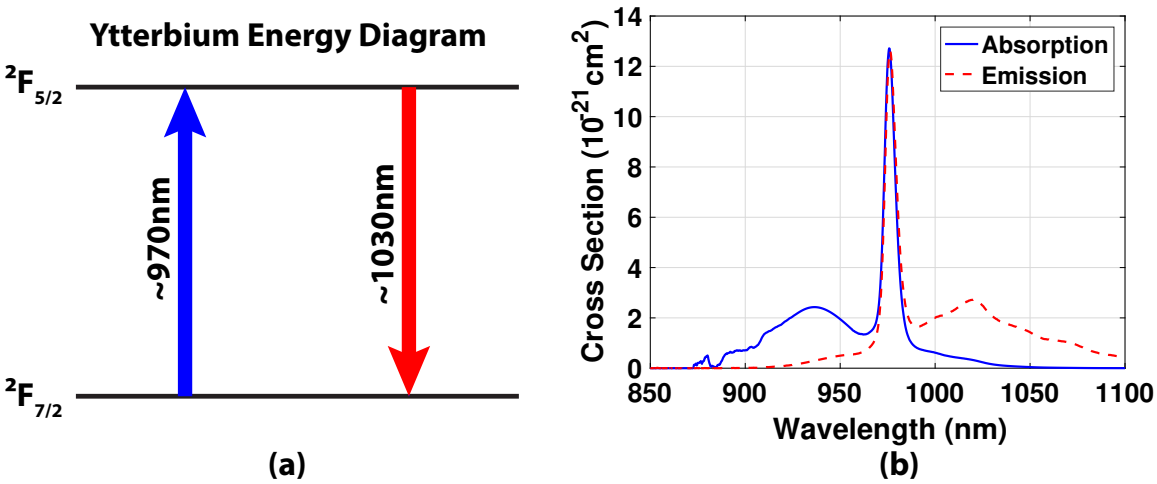

Fig. 4.27: (a) Energy levels of ytterbium ions. (b) Absorption and emission cross-sections of Yb ions in Al_2O_3 host material (data provided by Prof. Jonathan Bradley).

Ytterbium, as a rare-earth-ion dopant is suitable for this application. The energy levels of ytterbium ion (Yb^{3+}) are shown in Fig. 4.27(a). Yb^{3+} can be pumped with a

wavelength around 970nm and generate a laser signal around 1030nm. The measured absorption and emission spectra (data provided by Prof. Jonathan Bradley) of Yb^{3+} in Al_2O_3 host material are shown in Fig. 4.27(b). We notice that ytterbium can be efficiently pumped around 930 or 970nm, where for the latter case, the strong absorption is also accompanied by high emission at the same wavelength. Due to a limited range of the available tunable laser (960 – 990nm), for the rest of this section, we will focus on analyzing the ytterbium laser with a 970nm tunable laser pump.

4.4.1 Mode Profiles and Mode Overlap

Similar designs using trench-based microcavities for laser applications can be extended to ytterbium lasers. The major difference here is the footprint of the structure. Since the ytterbium laser lases around ∼1.1μm, it can be much more compact than a thulium laser. While we have demonstrated an 80-μm radius ytterbium laser using a slightly different design in Ref. [11] (Prof. Jonathan Bradley's work), the minimal size that we can achieve with this type of design is still unknown. For this section, I will focus on the optimization of the radius to make compact yet efficient on-chip ytterbium laser structures.

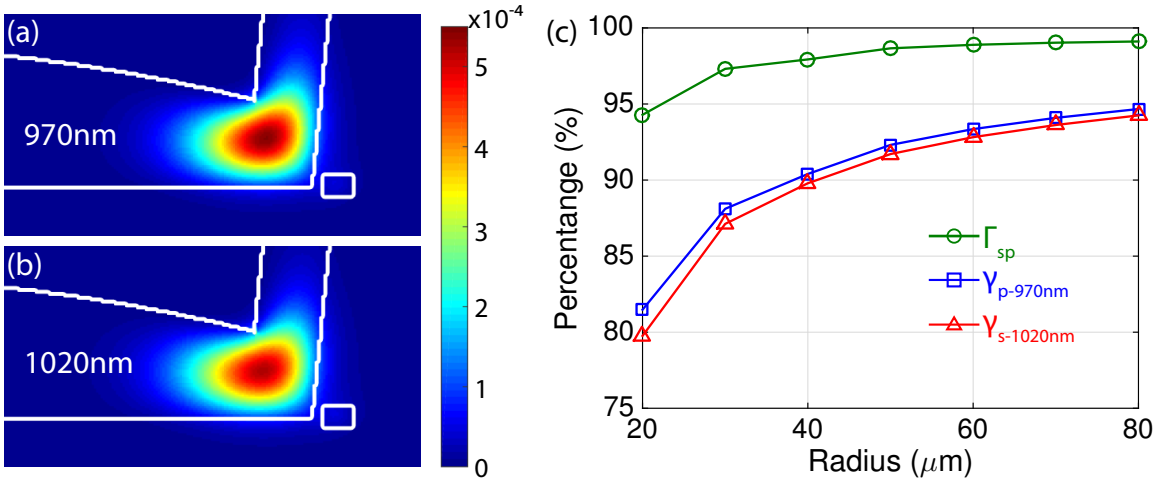

Fig. 4.28: Intensity profiles of resonant modes of the microcavity laser at (a) 970nm and (b) 1020nm for a 40-μm radius cavity size. (c) Confinement factors and intensity overlap between pump and laser modes for radii from 20 to 80μm.

The fundamental resonant modes of a 40-μm-radius and 1.6μm-thickness microcavity for both pump (970nm) and signal (1020nm) wavelengths are shown in Fig. 4.28(a)

and (b). The modes are confined by the trench wall and have similar shapes, indicating a significant intensity overlap between pump and signal modes. To characterize the properties of the modes, we use the same definition for the intensity confinement factor ($\gamma_{s/p}$) in Eqn. 4.4 and intensity overlap (Γ_{sp}) in Eqn. 4.5. The subscript s and p represent signal (∼1020nm) and pump (∼972nm), respectively. Fig. 4.28(c) shows both the confinement factors ($\gamma_{s/p}$) and intensity overlap (Γ_{sp}) of the pump and signal modes. Since the resonant modes are mostly confined in the Al_2O_3:Yb^{3+} layer, the confinement factors are generally very high (e.g. $> 90\%$ for radius $> 40\mu$m). Besides, the signal and pump modes are both confined by the trench wall and have similar mode profiles, making it easier to achieve high intensity-overlap between them. Therefore, with a sufficiently high Q-factor, lasing can be achieved easily within the microcavity.

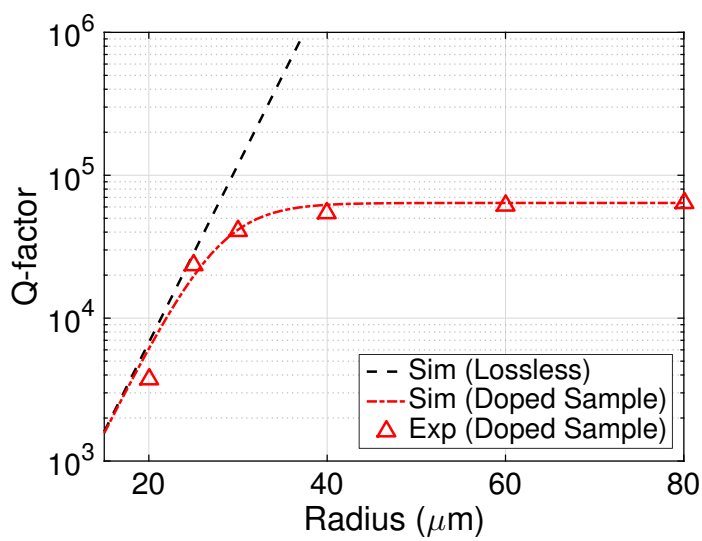

Fig. 4.29: Microcavity Q-factors for radii from 20 to 80μm for a wavelength of ∼970nm.

To analyze Q-factor dependence on microcavity radius, we fabricated microcavities with different radii (20, 25, 30, 40, 60, and 80 μm). Calculated and experimentally measured Q-factors for the Yb-doped Al_2O_3 microcavities are shown in Fig. 4.29. If only radiation loss is included in the model (black dashed line), a 40-μm radius device could offer an intrinsic Q-factor on the order of 1×10^6. However, for the doped sample, the intrinsic Q-factor of the cavity is reduced to 6×10^4 due to Yb^{3+} absorption. For smaller radius devices, the intrinsic Q-factors are closely matched

to radiation loss-limited Q-factors. Different from the Q-factor vs. radius curves discussed in Sec. 4.2, the material loss of Al_2O_3, scattering loss of the trench wall roughness are much smaller than the absorption loss of the dopants, resulting in a good match between the measurement and simulation where the dopant absorption is included.

4.4.2 Experimental Results

The experimental setup for measuring the Yb microlaser is shown in Fig. 4.30. A tunable pump laser is coupled onto the chip via a tapered fiber. The polarization of the pump laser is adjusted with a three-paddle polarization controller. The laser signals are then coupled off the chip and get separated from pump power using wavelength division multiplexers (WDMs). After the separation, the signals are collected by the optical spectrum analyzers (OSAs) on both sides of the chip. The residual pump light is coupled into a power meter for microcavity resonance identification.

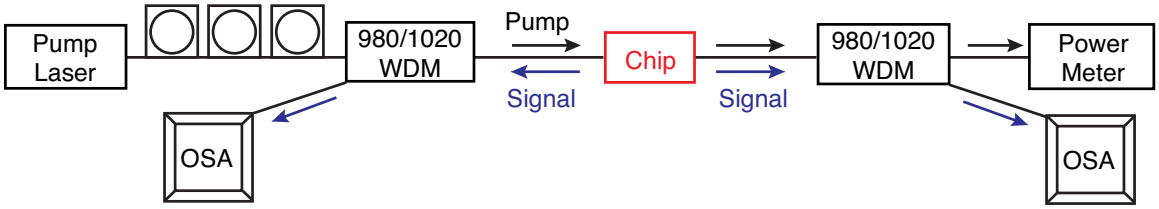

Fig. 4.30: Experimental setup for measuring the Yb microlaser.

The tunable pump laser used in the experiment has a maximum output power of ∼3.5mW. Lasing is observed for devices with a radius $\geq$ 40 μm, where the intrinsic loss of the cavity is relatively small compared to the pump absorption loss due to Yb^{3+} ions, which translates into a net gain at signal wavelengths. The laser output spectra of the 40μm-radius microcavities with different gap sizes are shown in Fig. 4.31(a) with a pump wavelength ∼972 nm. Multimode lasing behaviors are observed for devices with 400, 500, and 600nm gap sizes. The on-chip laser power versus on-chip pump is displayed in Fig. 4.31(b). A lasing threshold of 720μW (600nm gap) and a double-side slope efficiency of 1.9% (400-nm gap) were demonstrated.

The devices shown in this section have a film thickness of 1.60μm, which is, in fact, not the optimized thickness for a bend radius of 40μm. With more optimiza-

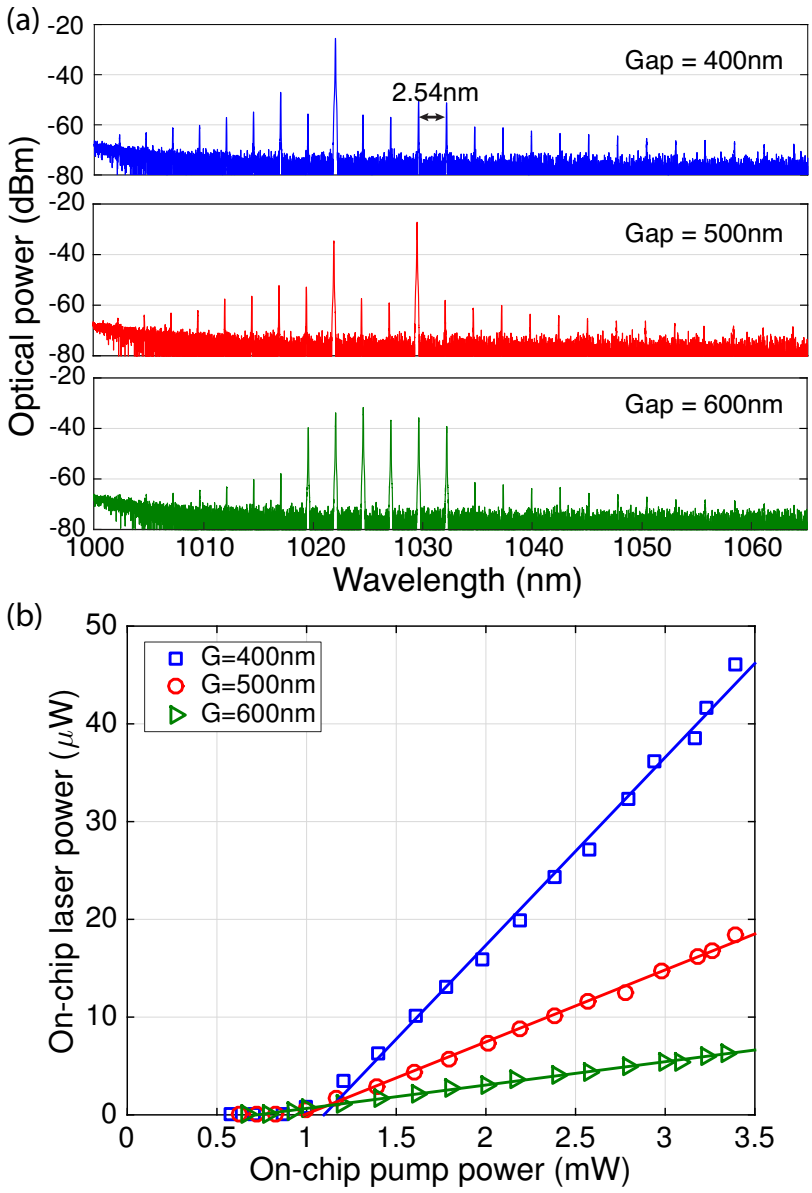

Fig. 4.31: (a) Spectrum of the output laser for gap sizes of 400, 500, and 600nm. (b) On-chip laser power versus on-chip pump power for gap sizes of 400, 500 and 600nm.

tion on film thickness and trench-wall roughness, it is possible that devices with a radius of 30μm radius could also lase. But the concept introduced in this section is useful for future study on this type of devices. In addition, high-index materials such as titanium dioxide (TiO_2) and tellurium dioxide (TeO_2) as the host materials for rare-earth-ions can potentially allow a higher intrinsic Q-factor at an even smaller radius and therefore achieve lasing with a smaller device footprint using the

same trench-based microcavity design. While other microcavity lasers have limited compatibility with a CMOS process, trench-based microlasers provide seamless integration with readily available silicon photonic device libraries such as high-speed detectors, modulators and full integration with state-of-art CMOS driving circuits, making the trench-based method discussed here a viable method for future lab-on-chip biosensing applications.

4.4.3 Conclusion

In this section, we demonstrated a CMOS-compatible 40μm-radius trench-based ytterbium laser on a silicon chip. The laser shows a slope efficiency of ∼1.9% and a sub-milliwatt threshold. Silicon compatibility and compact size make it possible to integrate such lasers within advanced silicon photonic systems.

CHAPTER 5

Wafer-Scale Robust High-Q Microcavity Design

The adiabatic microring resonator was first proposed by Prof. Michael R. Watts in Ref. [109]. In this chapter, a further analysis of the adiabatic microring resonator is presented. First, the fabrication tolerance of the adiabatic microring resonator was investigated in both theory and simulation. Based on the simulation, devices were fabricated on a 300mm wafer and tested in wafer-scale. Detailed wafer-scale variation parameters were extracted, showing reduced sensitivity to wafer-scale variations for adiabatic microring resonators. In addition, rigorous 3D finite-difference time-domain simulations were performed on this structure to analyze the intrinsic Q-factor with the insertion of contacts, demonstrating that the adiabatic microring resonator can be widely used as a replacement to conventional microring resonators.

5.1 Introduction to Adiabatic Microring Resonator

Microdisk resonators (shown in Fig. 5.1(a)) have been extensively used for applications requiring electrical or mechanical contact since interior contacts can be naturally implemented [7]. However, microrings (shown in Fig. 5.1(b)) are generally preferred for high-performance applications due to their broad, uncorrupted free spectral ranges (FSRs) that can, for example, accommodate more frequency channels in an optical communication line. For a wafer-scale fabrication, the variations across the wafer will induce variations in resonant wavelengths or frequencies of the cavity, making it hard to fabricate two identical cavities even on the same wafer. Therefore, to make a resonator working for a particular wavelength, apart from the accurate information of the material indices and rigorous simulations, the resonator needs to be both efficiently tunable and wafer-scale fabrication-tolerant to lower the power budget for wavelength alignment while maintaining a single-mode operation.

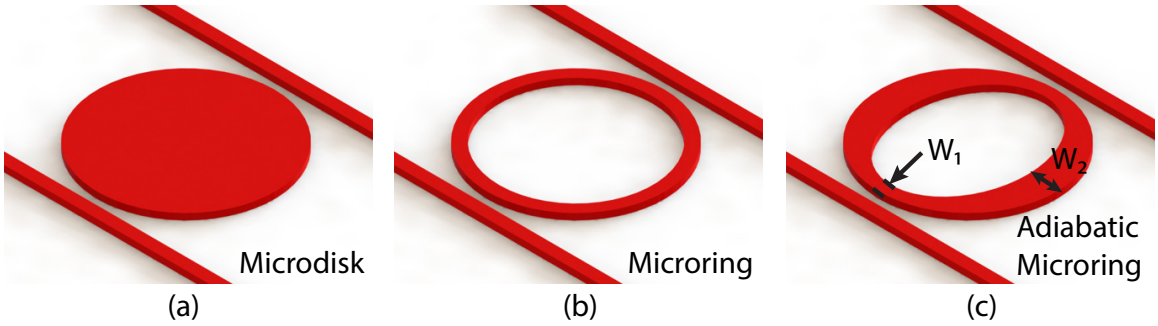

Fig. 5.1: Schematics of (a) a microdisk resonator, (b) a microring resonator, and (c) an adiabatic microring resonator.

The adiabatic microring resonator (shown in Fig. 5.1(c)) proposed by Prof. Michael R. Watts in Ref. [109] provided a new approach to accommodating the previous requirements. The efficient tunability comes from the fact that lossless electrical or mechanical contacts can be inserted into the cavity directly [50]. The single-mode operation is enabled by the adiabatic change from a conventional single-mode ring mode to a disk mode without any excitation of high-order modes in the cavity. The wafer-scale variation sensitivity can also be reduced by transferring a highly sensitive microring-like mode to a robust microdisk-like mode.

5.2 Reduced Wafer-Scale Variation Sensitivity – Simulation

For a wafer-scale fabrication process, there are several sources of variations that can contribute to resonant wavelength variations of the fabricated cavities. For a microdisk structure shown in Fig. 5.1(a), the change of resonant wavelength comes from variations of the microdisk radius and the thickness of the layer. For a microring structure shown in Fig. 5.1(b), there is another degree of freedom that the width of the microring can also change. Since the height variations of the layer are defined by the wafer provider, we would not be able to adjust it. We will focus on reducing the lateral sensitivity in our design.

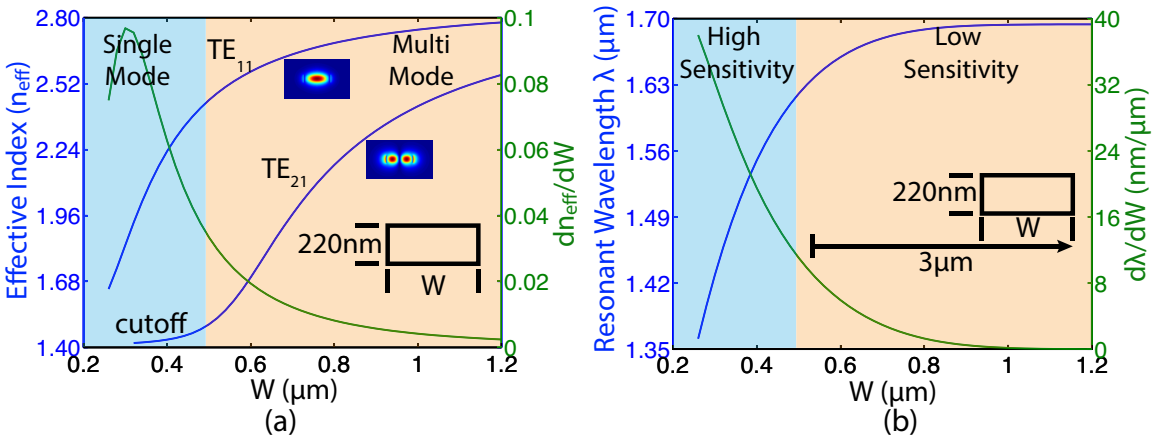

Fig. 5.2: (a) The effective indices of the eigenmodes (TE_{11} and TE_{21}) for 200-nm-thick silicon waveguides with different widths (shown as blue lines). The slope of the TE_{11} curve is also plotted (shown as green line). (b) Resonant wavelengths of te fundamental TE-mode of a 3μm-radius silicon microcavity with different waveguide widths (shown as blue line). The slope is also plotted (shown as green line).

Fig. 5.2(a) shows the effective indices of fundamental TE modes (TE_{11}) of straight 200-nm-thick silicon waveguides with different widths (W). We can see that the effective index curve has a larger slope in the single-mode region than that of the multi-mode region where high order modes such as TE_{21} and TE_{31} can be supported. The difference in the slopes indicates that a microring resonator with a wide waveguide will have a lower sensitivity to fabrication variations in width. We also simulated the resonant wavelengths of 3μm-radius ring resonators with different waveguide widths. The resonant wavelength sensitivities to the width ($d\lambda/dW$) are much lower for a

1μm-wide resonator than for a 0.4μm-wide one.

To analyze the fabrication tolerance of the adiabatic microring resonator, we assume Gaussian distributions for variations of both width and outer radius of the cavity with a mean value of zero and a 5nm standard deviation. The width for the adiabatic ring resonator is slowly changed inside the cavity. Therefore, it is difficult to use a 2D mode solver to calculate the resonant wavelength directly. Instead, as an approximation, the resonant mode inside the cavity is represented with an effective index n_{eff} which is defined as:

$$n_{eff} = \frac{m\lambda}{2\pi R} \tag{5.1}$$

where m is the mode order and λ is the resonant wavelength. Since we are mostly interested in wavelength around 1.55μm, the mode order ms in the following analysis are calculated around wavelength 1.55μm. The total optical path length for a single round-trip along the cavity can be represented as

$$L_{eff} = \frac{\int_0^{2\pi} n_{eff}(\theta, W) \cdot 2\pi R \mathrm{d}\theta}{2\pi} \tag{5.2}$$

where on resonance, L_{eff} needs to be a multiple of wavelength in length. We choose to analyze the resonant wavelength that is close to and lower than 1.55μm. With this constraint, we are able to calculate the mode order value m_0 for the unperturbed case.

In Eqn. 5.1, n_{eff} is a function of wavelength (λ), waveguide width (W) and outer radius (R). Among them, n_{eff} is weakly dependent on outer radius. With the introduction of the variation on width (ΔW) and radius (ΔR), the resonant wavelength variations of microrings can then be calculated as

$$\Delta\lambda(W, R) = 2\pi[\frac{\partial n_{eff}}{\partial W}\Delta W \cdot R + \frac{\partial n_{eff}}{\partial R}\Delta R \cdot R + n_{eff} \cdot \Delta R]/[m_0 - 2\pi R\frac{\partial n_{eff}}{\partial \lambda}] \tag{5.3}$$

The total wavelength shifts caused by fabrication variations to a adiabatic microring resonator can be calculated by integrating $\Delta\lambda$ along the resonator where the waveguide width is changing gradually.

With the assumed Gaussian perturbations on width and radius, we calculated the standard deviations of the adiabatic microring resonator with different W_2 widths (defined in Fig. 5.1). Fig. 5.3(a) shows the calculated standard deviation as a function of W_2. The standard deviation of the resonant wavelength is reduced from 5nm

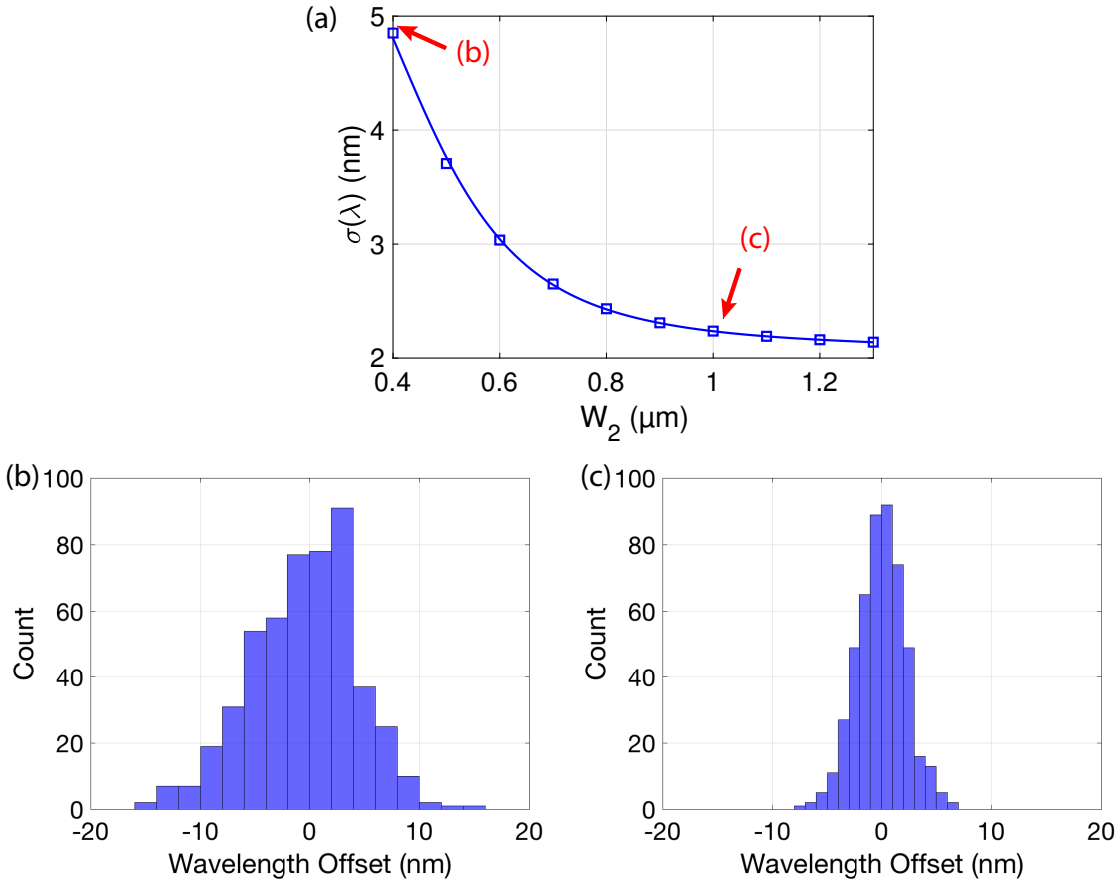

Fig. 5.3: (a) Standard deviations of simulated adiabatic microring resonators with different W_2 sizes. We assume Gaussian distributions of variations on radius and width of the adiabatic microring resonators with a mean value of zero and a standard deviation of 5nm. (b) Histogram of the wavelength offset distribution for $W_2 = 0.4\mu m$. (c) Histogram of the wavelength offset distribution for $W_2 = 1.0\mu m$.

to 2.1nm when W_2 is increased from 400nm to 1.3μm. We also plot the histogram of the simulated wavelength offsets for $W_2 = 0.4$ and 1.0μm in Fig. 5.3(b) and (c) respectively. The wavelength offsets have a much narrower distribution for the wider W_2 than the narrower one, proving the effectiveness of the adiabatic microring resonator in improving the fabrication tolerance of optical microcavities.

5.3 Reduced Wafer-Scale Variation Sensitivity – Experiment

We also fabricated a set of devices on a 300-mm wafer and tested resonant devices in wafer-scale. The fabricated 300-mm wafer is shown in Fig. 5.4(a) with single reticle size of 32mm by 26mm. To separate the contribution of each component, microdisk

resonator resonators with 10-μm designed radius (shown in Fig. 5.4(b)), which have only thickness and radius variations, were first measured. Fig. 5.4(c) and (e) show the typical transmission spectra of the disk resonators for input polarization states of TE and TM, respectively. Several high-order modes show up in each FSR. Fig. 5.4(d) and (f) show the histograms of selected TE and TM resonant wavelengths (indicated by dotted red circles) measured across the wafer, where standard deviations are 1.97nm (246GHz) and 4.37nm (545GHz) for TE and TM modes respectively. By analyzing the relation between TE and TM resonance shifts [36], the standard deviations of thickness (T) and radius (R) of the disk resonators were calculated to be 1.351nm (σ_T) and 3.735nm (σ_R).

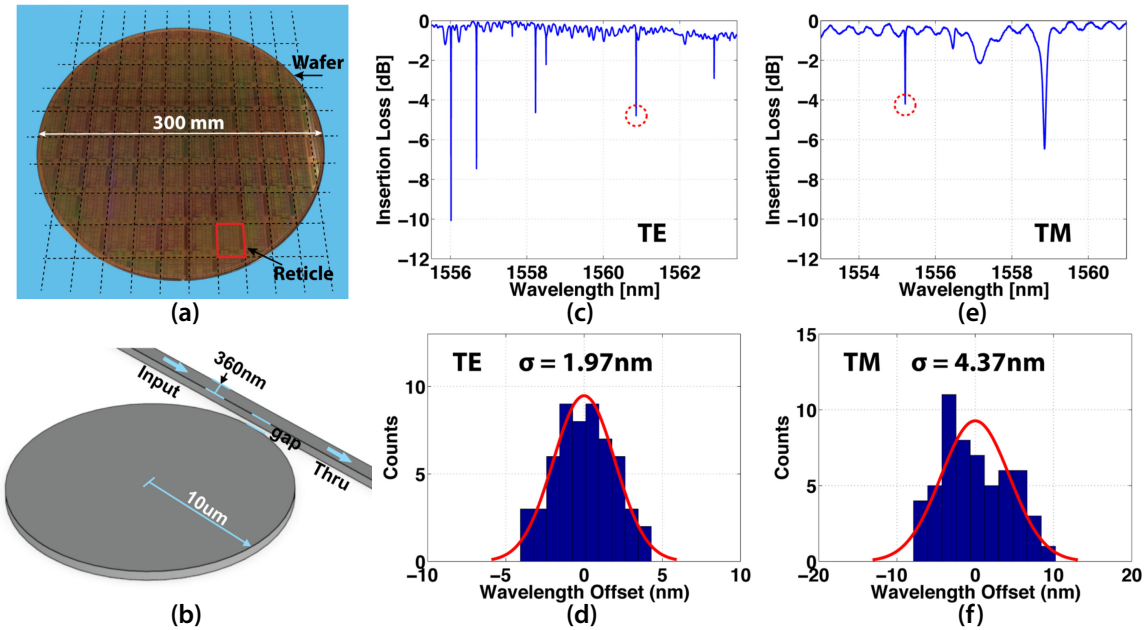

Fig. 5.4: (a) Fabricated 300mm wafer with a single reticle marked with a red rectangle. (b) A schematic of a 10μm-radius microdisk resonator coupled to a 360nm-wide bus waveguide. (c) An example of the transmission spectrum of the microdisk resonator with TE input. (d) Histogram of wavelengths of the selected resonant mode (marked by the red dotted circle in (c)) across the wafer. (e) An example of the transmission spectrum of the microdisk resonator with TM input. (f) Histogram of wavelengths of the selected resonant mode (marked by red dotted circle in (e)) across the wafer.

With the thickness and radius variations extracted from microdisk measurements, microring structures were then measured across the wafer to find the width varia-

tion induced by lithographical imperfections. Assuming independent distributions of thickness, radius and width, the overall resonant wavelength shift of a microring resonator is then given by

$$\Delta\lambda = \frac{\partial\lambda}{\partial T}\cdot\Delta T + \frac{\partial\lambda}{\partial R}\cdot\Delta R + \frac{\partial\lambda}{\partial W}\cdot\Delta W \tag{5.4}$$

where $\Delta\lambda$ is the total resonant wavelength shift, ΔT, ΔR and ΔW are the thickness, radius and width changes. The standard deviation of resonant wavelength λ is then given by

$$\sigma(\lambda) = \sqrt{(\frac{\partial\lambda}{\partial T}\sigma_T)^2 + (\frac{\partial\lambda}{\partial R}\sigma_R)^2 + (\frac{\partial\lambda}{\partial W}\sigma_W)^2} \tag{5.5}$$

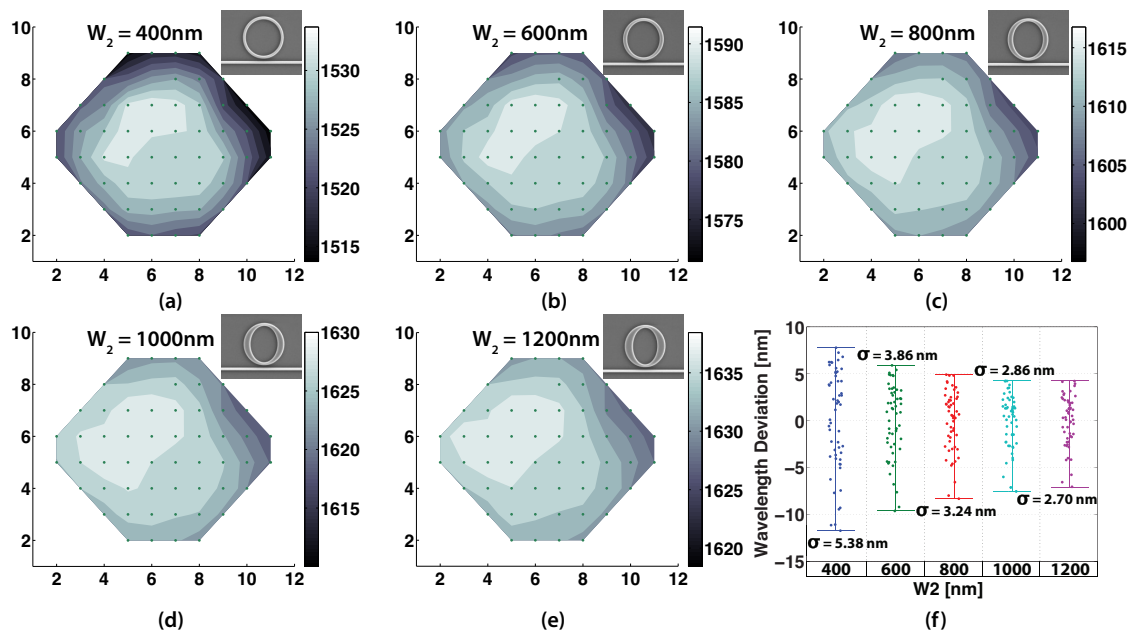

Fig. 5.5: Wavelength distribution across the wafer for (a) W_2 = 400nm. (b) W_2 = 600nm. (c) W_2 = 800nm. (d) W_2 = 1000nm. (e) W_2 = 1200nm. The dots represent the position of the measured chips and the unit of the colorbar is nm. The insets are the SEMs of corresponding adiabatic microring resonators with different W_2 sizes. (f) Resonant wavelengths variations cross the wafer for various W_2 sizes.

For a 3μm-radius ring with a waveguide width of 400nm and a height of 220nm, the resonant wavelength change due to thickness, radius and width variations are 1.367 nm/nm ($\partial\lambda/\partial T$), 0.291 nm/nm ($\partial\lambda/\partial R$) and 0.894 nm/nm ($\partial\lambda/\partial W$), respectively. The standard deviation of resonant wavelengths (frequencies) of conventional microring resonators is measured to be 5.38nm (671GHz) (shown in Fig. 5.5(f)). According

to Eqn. 5.5, the width variation σ_W is 5.520nm, outweighing the effects of the other two degrees of freedom.

Resonant wavelengths of adiabatic microring resonators with different W_2 sizes were then measured in 54 dies across the 300mm wafer, and their distributions are shown in Fig. 5.5(a)-(e). The color bars used in those images cover a 20-nm wavelength range. We can see that the resonant wavelength distributions become more uniform with the increase of W_2 size. The resonant wavelength standard deviations of adiabatic microring resonators decrease from 5.38nm (671GHz) to 2.70nm (337GHz) with the increase of W_2 from 400nm to 1200nm, a factor of two improvement compared to standard microrings, as shown in Fig. 5.5(f). This improved fabrication tolerance is essential to the wafer-scale production of microring-based photonic structures such as multiplexers/demultiplexers for wavelength division multiplexing and optoelectronics modulators.

5.4 High-Q Cavity with Contacts

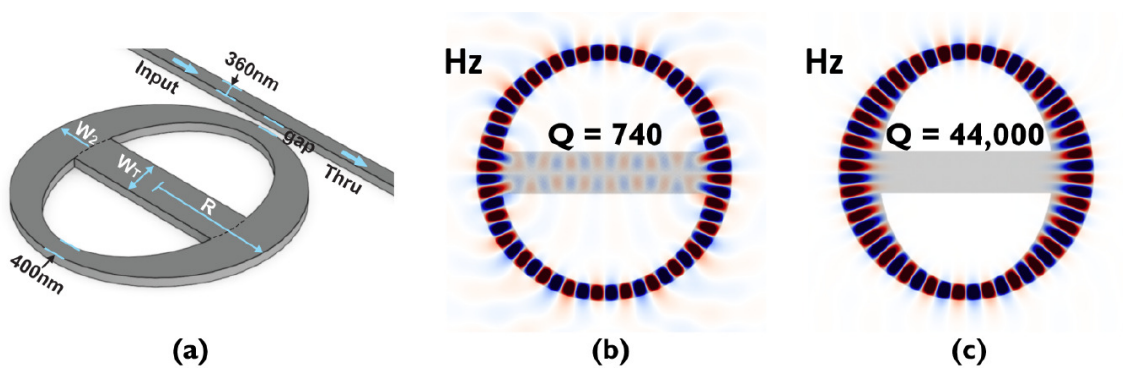

Fig. 5.6: (a) A schematic of the adiabatic ring resonator. The bus waveguide width is 360nm. The thickness of the structure is 220nm. Properties such as the wider part of the adiabatic microring resonators (W_2) and tether width (W_T) are marked. Mode profiles of 3μm-radius adiabatic microring resonators with (b) $W_2 = 0.6$μm and $W_T = 1$μm and (c) $W_2 = 1$μm and $W_T = 1$μm. The colors of the modes are saturated to show the radiation loss.

Fig. 5.6(a) shows the schematic of an adiabatic microring resonator coupled to a bus waveguide. Light is coupled from a 360nm-wide bus waveguide to the adiabatic microring resonator whose width is gradually, or adiabatically, widened from 400nm at the coupling point to W_2 in a 90° bend. The adiabatic transition avoids the excitation

of high-order modes so that a clear FSR can be achieved. The silicon contact with width W_T is introduced at the widest part of the adiabatic microring resonator where little optical field sees the silicon contact to avoid scattering loss. Fig. 5.6(b) and (c) show the simulated modes (Hz field) of adiabatic microring resonators with a narrower W_2 (0.6μm) and a wider W_2 (1.0μm) using a 3D-FDTD simulation in the presence of the silicon contact. We can see that the optical mode in the one with the narrower contact region (W_2 = 0.6μm), which more resembles a conventional microring, suffers larger scattering loss than that in the optimized adiabatic microring resonator (Fig. 5.6(c)).

Fig. 5.7 (a) and (b) show the scanning-electron-micrograph (SEM) images of the fabricated adiabatic microring resonators with 2 and 3μm radii. The corresponding transmission spectra around the resonances of the fabricated devices are shown in Fig. 5.7(c) and (d), showing clean FSRs and Q-factors as high as 7,000 for 2μm radius and 27,000 for 3μm radius devices experimentally.

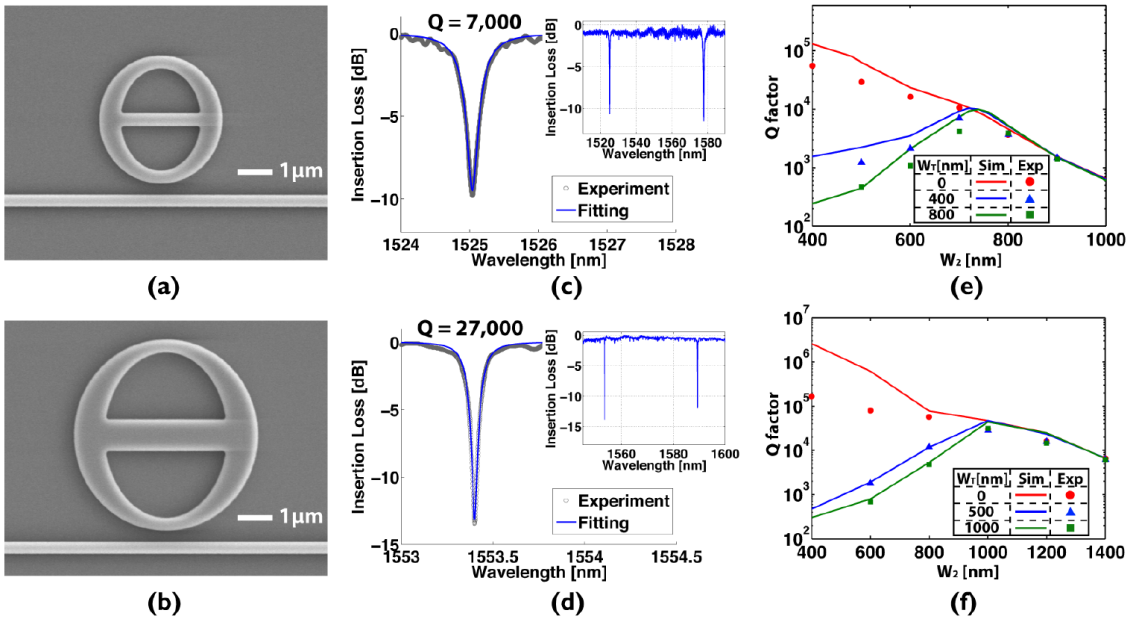

Fig. 5.7: Top-view scanning-electron-microscope (SEM) images of the adiabatic microring resonator structure with (a) 2μm-radius, W_2 = 0.7μm and W_T = 0.4μm and (b) 3μm-radius, W_2 = 1μm and W_T = 1μm. Transmission spectrum of devices with (c) 2μm radius and (d) 3μm radius. Insets are wide spectra across one whole FSR. Intrisic Q-factors for (e) 2μm and (f) 3μm-radius resonators with different W_2 and W_T sizes.

For devices of this type, a widened contact region (W_2) avoids scattering loss from the silicon contact; however, if W_2 becomes too large, the transition is too abrupt to be taken as adiabatic. As a result, high-order modes will be excited in the microcavity, causing excessive losses. Therefore, there exists an optimal waveguide width, W_2, at the point of contact that corresponds to the lowest radiation loss. The Q-factors of the adiabatic microring resonators at different waveguide widths W_2, were calculated using rigorous 3D FDTD simulations, shown by the solid lines in Fig. 5.7(e) and (f). The highest Q-factors (9,950, 44,000) were achieved for a waveguide width W_2 of 740nm for a 2μm-radius adiabatic microring resonator, and a W_2 of 1000nm for a 3μm-radius one. To validate the simulation results, resonators with different waveguide widths W_2, contact widths W_T, and radii R were fabricated and measured to extract the Q-factors, as shown by dots in Fig. 5.7(e) and (f). The experimental data agree well with the simulations; in particular, the optimized W_2 sizes were accurately predicted by the simulation. High Q-factors (7,000, 27,000) were experimentally demonstrated in 2μm and 3μm-radius resonators in the presence of silicon contacts. Note that the experiments show much lower Q-factors compared to simulations in the resonators without contacts (solid red lines and dots in Fig. 5.7(e) and (f)) in the low loss region ($Q > 10^5$). The difference comes from the material absorption and surface roughness induced losses, which were not taken into account in the simulation.

5.5 Conclusion

To summarize, adiabatic microring resonators have been designed and demonstrated, revealing high quality factors, uncorrupted FSRs, and importantly, reduced susceptibilities to wafer-scale fabrication-induced resonant frequency deviations. The combination of enhanced resonant frequency uniformity and the ability to contact adiabatic microring resonators for tuning and/or modulation without affecting the FSR provides substantial reasons to consider the use of adiabatic microring resonators as a replacement for standard microring resonators in nearly all communication applications.

CHAPTER 6

Conclusions

In this chapter, the main results of this thesis are summarized. An outlook for future microcavity-based devices is also discussed.

In this thesis, microcavities, as essential building blocks for silicon photonics, were analyzed in optical signal routing, photodetection, and lasing applications. Several specific objectives, including developing a WDM-compatible multicast network, extending the detection range of germanium material and demonstrating easy-to-fabricate rare-earth-ion-based on-chip lasers have been achieved. In addition, high-Q and wafer-scale fabrication-tolerant microcavity designs have been analyzed and shown in devices fabricated in a CMOS foundry.

The concept of partial-drop was first introduced by introducing asymmetry into conventional microring-based filters and analyzed using the coupled-mode-theory. Based on the developed theory, a new architecture of WDM-compatible optical multicasting system was proposed and developed. Uniform responses and error-free data communication operations across all the drop ports were achieved. Furthermore, a similar concept was introduced to second-order filters to address the problem of slow roll-off speed associated with the first-order filter followed by a system-level demonstration. In addition, with rigorous theoretical analysis, a microring-based optical multicasting system was extended to even high-order designs, providing a reliable path toward datacom- or telecom-grade applications.

On the detector side, to further increase the wavelength detection range of a Ge-based structure without compromising performance, a resonant germanium-on-silicon detector was proposed. By exploiting the large absorption difference between silicon and germanium, a resonant mode that is mostly guided in silicon but with a loss dominated by germanium was implemented. The resonant detector was then fabricated in a CMOS foundry by introducing a vertical p-i-n junction within the cavity. Dark current of nA-scale, photoresponsivity of 1A/W at 1530nm, and optoelectric bandwidth of 32GHz were demonstrated with a device radius of 4.5μm. Moreover, the design has a lower cavity loss dependence on wavelength, enabling a responsivity of 0.45A/W at wavelength 1630nm, more than four times higher than a straight waveguide type detector fabricated on the same wafer. The design concept used for Ge-on-Si photodetectors can also be used in other systems to extend the working wavelength ranges of absorptive materials.

For the laser development, an on-chip Al_2O_3 microcavity design was first intro-

duced. The microcavity was fabricated by deep SiO_2 etching for trench formation followed by Al_2O_3 film deposition. The cross-section of the passive cavity was then investigated using a focus-ion-beam cutting near the trench wall. The resonant cavity modes were studied with a rigorous finite-difference bend mode solver for both TE and TM polarizations. Based on the analysis, a set of devices with different variations were fabricated and analyzed experimentally. Furthermore, using the microcavity model together with experimental analysis, rare-earth-ion dopants such as thulium and ytterbium were co-sputtered with Al_2O_3. Optically pumped on-chip microcavity lasers at 1.1μm (Yb) and 1.8μm (Tm) wavelengths were demonstrated. Further improvement and extension of this type of device will focus on trench roughness smoothing, lasing mode selection and different rare-earth-ion dopants to enable applications for various wavelengths.

To move toward wafer-scale microcavity fabrication, at the final part of the thesis, a high-Q wafer-scale fabrication tolerant microcavity was demonstrated. This design was first proposed by Prof. Watts in Ref. [109]. Fabrication tolerance analysis was first performed in both theory and simulation. A set of devices were then fabricated on a 300mm wafer and tested in wafer-scale, showing a reduced sensitivity to fabrication variations. In addition, Q-factors of cavity design under contact insertion was also investigated. The adiabatic microring resonators were found to exhibit higher Q-factors. The combination of enhanced resonant frequency uniformity and the ability to insert contact for tuning and modulation without inducing additional losses, provide substantial reasons to consider the use of adiabatic microring resonators as a replacement for standard microring resonators in nearly all communication applications.

Appendices

A Quality Factor Definition and Related Calculations

The quality factor (Q-factor) is an important dimensionless property of a cavity-based structure. However, the existence of multiple definitions with different assumptions can sometimes result in a confusion, leading to an error in calculating the exact Q-factor. Common mistakes include multiplying or dividing the real Q-factor by a factor of 2 or π. Therefore, I feel it necessary to add this appendix to clarify the definition and usage of this important parameter.

For a resonant mode with an angular frequency of ω_0 in a cavity, assuming it decays slowly with an exponential decay, it will behave like a mode with a complex frequency of $\omega_c = \omega_0 - i\gamma/2$. This way, the mode field will decay with $e^{-\gamma t/2}$ while the energy within the cavity will decay with $e^{-\gamma t}$. The decay time constant τ can be represented as

$$\tau = \frac{2}{\gamma} \tag{A.1}$$

The dimensionless Q-factor of the cavity is defined as

$$Q = \frac{\omega_0}{\gamma} = \frac{\omega_0 \tau}{2} \tag{A.2}$$

Eqn. A.2 serves as the official definition of the Q-factor. There are several other ways to interpret the meaning of Q-factor. We will cover them in the following discussion.

(1) $1/Q$ as a dimensionless decay rate

Similar to the Q-factor definition used in circuits, $1/Q$ is defined as

$$\frac{1}{Q} = \frac{P}{\omega_0 U} \tag{A.3}$$

where P is the power consumption and U is the electromagnetic energy localized in the cavity. For a standalone cavity, the power consumption is the time derivative of the total stored energy in the cavity. U can be represented as

$$U = U_0 \exp(-\gamma t) \tag{A.4}$$

Therefore

$$P = -\frac{\partial U}{\partial t} = \gamma U_0 \exp(-\gamma t) \tag{A.5}$$

Combining Eqn. A.4 and A.5 together with Eqn. A.3, we will arrive at the same equation as Eqn. A.2.

(2) Q as a dimensionless lifetime

Q-factor can also represent the number of optical periods that elapse before the energy decays to $e^{-2\pi}$ of its original value. From Eqn. A.4, we can extract the needed time is $2\pi/\gamma$ and the corresponding number of optical periods $(2\pi/\gamma)/(2\pi/\omega_0) = \omega_0/\gamma$. This also agree with original Q-factor definition in Eqn. A.2.

(3) $1/Q$ as the fractional bandwidth of the resonance

We cannot measure the fractional bandwidth of the resonance without coupling external EM-waves into the cavity. For the device configuration of this definition, the external coupling Q-factor is matched to the intrinsic Q-factor. Therefore, using the Q definition in Eqn. A.2, the transmission response can be represented as

$$T = \frac{(\omega_0 - \omega)^2}{(\omega - \omega_0)^2 + (\omega_0/2Q_t)^2} \tag{A.6}$$

where Q_t is the total Q-factor (half of intrinsic Q-factor). The full-width-half-maximum (FWHM) bandwidth of the response is calculated to be $1/Q_t$. Therefore, $1/Q$ can also act as the fractional bandwidth of the resonance.

To fully represent a microcavity, more parameters such as mode effective index n_{eff}, group index n_g, device radius R, free-spectral-range (FSR), and field decay contant (α or α_{dB}) need to be involved. The relations among those parameters will be discussed next for future design reference.

For a resonator, the general equation for resonance is

$$m \cdot 2\pi c = n_{eff,\omega_0} \cdot 2\pi R \cdot \omega_0 \tag{A.7}$$

where m is an integer, representing the mode order, and ω_0 stands for the resonant frequency. The mode effective index is dependent on the frequency. The equation corresponding to the mode with $m+1$ order is

$$(m+1) \cdot 2\pi c = n_{eff,\omega_1} \cdot 2\pi R \cdot \omega_1 \tag{A.8}$$

Combining Eqn. A.7 and A.8, we can calculate the free-spectral-range (FSR) as

$$FSR(\omega) = \Delta\omega = \frac{c}{R \cdot n_g} \tag{A.9}$$

$$FSR(\lambda) = \Delta\lambda = \frac{\lambda_0^2}{2\pi R \cdot n_g} \tag{A.10}$$

The mode field in the cavity is decaying as $e^{-t/\tau}$ and the energy inside the cavity is decaying as $e^{-2t/\tau}$. The power flow speed is the group velocity v_g. Thus time t can be represented as $t = L/v_g$ where L is the total propagation length. In this case, time and space are linked to each other. For a propagation length of L, the energy decay can also be expressed as $e^{-2\alpha L}$. Therefore, we have

$$e^{\frac{2L}{v_g \tau}} = e^{-2\alpha L} \tag{A.11}$$

$$\alpha = \frac{1}{v_g \tau} \tag{A.12}$$

Given $Q = \omega_0 \tau/2$, the relation between Q and α is then

$$Q = \frac{\omega_0 n_g}{2c\alpha} = \frac{\lambda_0}{2R\alpha \cdot FSR(\lambda)} \tag{A.13}$$

However, in this calculation, n_g and R are separated for different calculation purposes. This indicates that there will be some deviations in calculations of Q or α using this method for small-radius ring resonators. The α can be calculated using loss per length in dB scale (α_{dB}) as shown below:

$$\alpha_{dB} = 20\alpha \log_{10}(e) \tag{A.14}$$

where e is the natural logarithm and $\log_{10}(e) = 0.4343$.

In addition, the conversion between coupling coefficient and coupling Q-factor is also very useful. κ^2 is defined as the fraction of power coupled into a cavity. As calculated in Ref. [33], $\kappa^2 v_g (2\pi R)^{-1} = 2/\tau_e = \omega/Q_e$. Therefore, the coupling Q-factor can be represented as

$$Q_e = \frac{\omega_0 \cdot \lambda^2}{\kappa^2 \cdot FSR(\lambda) \cdot c_0} \tag{A.15}$$

$$= \frac{2\pi\lambda}{\kappa^2 \cdot FSR(\lambda)} \tag{A.16}$$

B Quality Factors Extraction

In the appendix, MATLAB scripts to facilitate the Q-factor extraction of measured microcavity transmission spectrum included. The fitting scripts are based on theory provided in Ref. [70].

For a system where a bus waveguide can couple power into a nearby microcavity, the typical response would be a Lorentzian-type transmission based on coupled-mode-theory. An example of the transmission spectrum is shown in Fig. .1(a). While for a high-Q cavity, the counter-clockwise (CCW) and clockwise(CW) modes could have a non-negligible mutual coupling, resulting in clear double resonances as shown in Fig. .1(b).

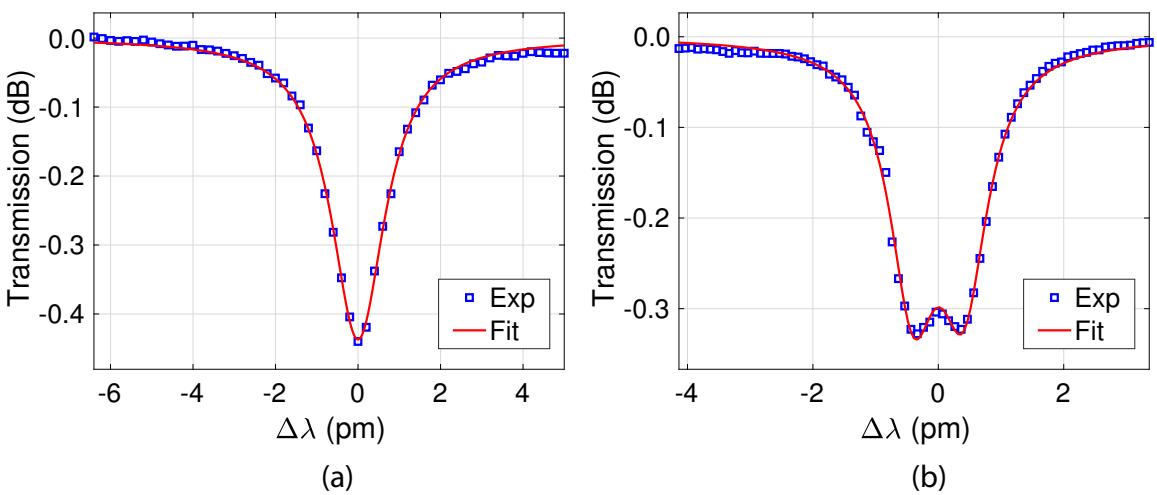

Fig. .1: (a) Typical single-dip transmission response and fitted curve. (b) Typical double-dip transmission response and fitted curve.

Throughout the thesis, Q-factor extraction from fitting to transmission spectrum is one of the key components in characterizing resonant-based devices. Therefore, an efficient tool for Q-factor extraction is necessary.

The MATLAB function to fit to a transmission spectrum with only one resonance is attached below.

```
function [y] = lorFitSingleLog(param,x)
% % Q is defined as Re(w)/(-2Im(w))
% % Q and tau are linked through Q = Re(w)*tau/2
```

```
% % the Lorentzian function is derived from
% % B.E. Little, S.T. Chu, H.A. Haus, J. Foresi, J.P. Laine, J. Lightwave Technol. ...
    15, 998-1005 (1998).
% % param = [Qi Qe lam0(nm) C]
% % x is wavelength in nm
% % Qi: intrinsic Q-factor
% % Qe: coupling (extrinsic) Q-factor
% % lam0: resonant wavelength
% % C: power level adjustment

imj = -sqrt(-1); % j
c0 = 2.99792458e17; % nm/s

Qi = param(1); % intrinsic Q
Qe = param(2); % coupling (extrinsic) Q
lam0 = param(3); % nm
C = param(4); % offset of insertion loss
w0 = 2*pi*c0/lam0; % /s
w = 2*pi*c0./x; % /s

dividend = imj*2*(w-w0)/w0+1/Qi-1/Qe;
divisor = imj*2*(w-w0)/w0+1/Qi+1/Qe;

T = (abs(dividend).^2)./(abs(divisor).^2); % transmission calculated from CMT
y = 10*log10(T)+C; % transform into dB scale + level adjustment
```

With this function, a fitting process can be implemented with the least-square curve fitting in MATLAB. Here is an example of the MATLAB script I used for curve fitting:

```
% % this script is used for fitting to Lorentzian response with single resonance
clear all; close all;
inputFileName = 'input.mat'; % input file name

%% load measurement data from Agilent Laser
f1 = load(inputFileName);
wavelength = f1.Data.Graphs.IL(:,1)*1e9; % wavelength in nm
transmission = -f1.Data.Graphs.IL(:,2); % transmission in dBm
transmission = transmission - max(transmission); % move the transmission to zero level

%% plot the directly measured transmission response
figure1 = figure('Color',[1 1 1]);
axes1 = axes('Parent',figure1,...
```

```
'FontSize',20);
box(axes1,'on');
grid(axes1,'on');
hold(axes1,'all');
plot(wavelength, transmission,'LineWidth',2);
xlabel('Wavelength (nm)');
ylabel('Insertion Loss (dB)');

%% select fitting wavelength range (cover the region of the resonance)
[xx1 yy1] = ginput(2);
selectRange = logical((wavelength>xx1(1)) .* (wavelength<xx1(2)));
wavelengthSelect = wavelength(selectRange);
transmissionSelect = transmission(selectRange);

%% plot selected range
figure1 = figure('Color',[1 1 1]);
axes1 = axes('Parent',figure1,...
'FontSize',20);
box(axes1,'on');
grid(axes1,'on');
hold(axes1,'all');
plot(wavelengthSelect, transmissionSelect,'ob');
xlabel('Wavelength (nm)');
ylabel('Insertion Loss (dB)');
xlim([min(wavelengthSelect) max(wavelengthSelect)]);
hold on;

%% fitting part
%% guess value
Qi = 1e6; % intrinsic Q-factor
Qe = 2.9e6; % extrinsic Q-factor
[lam0 ER] = ginput(1); % select the center wavelength, ER for extinction
C = max(transmissionSelect); % power level adjustment (dB)
paramStart = [Qi Qe lam0 C]'; % guess value (fitting starting point)
fprintf('Start:\n Qi = %.3f\n Qe = %.3f\n lam0 = %.6f\n C = %.3f\n', ...
paramStart(1), paramStart(2), paramStart(3), paramStart(4));

%% fitting options
lb = [1e4 1e4 1470 -5];
ub = [1e7 1e8 1490 2];
options = optimset('lsqcurvefit');
options = optimset(options,'TolX',1e-13 ,'TolFun',1e-13);
options.MaxFunEvals = 10000;
options.MaxIter = 10000;

```

```
%% fitting
[paramEndlsq, error] = lsqcurvefit(@lorFitSingleLog, paramStart,...
wavelengthSelect, transmissionSelect, lb, ub, options);
fprintf('End:\n Qi = %.3f\n Qe = %.3f\n lam0 = %.6f\n C = %.3f\n',...
paramEndlsq(1),paramEndlsq(2),paramEndlsq(3),paramEndlsq(4));

%% plot fitted curve
wavelengthFit = min(wavelengthSelect):0.05e-3:max(wavelengthSelect); % 0.5pm ...
    resolution
transmissionFit = lorFitSingleLog(paramEndlsq, wavelengthFit);
plot(wavelengthFit, transmissionFit, '-r', 'LineWidth', 2);

%% save fitting data
fileOutputName = 'output.mat';
save(fileOutputName, 'paramEndlsq', 'wavelengthSelect', 'transmissionSelect',...
'wavelengthFit','transmissionFit');
```

The input file in the example script is assumed to be the file exported from Agilent (now Keysight) laser measurement software. In order to have a better fitting performance, a lower-bound and upper-bound of the fitting parameters involved are provided for a fast convergence.

For the case where the transmission spectrum shows a double-resonance feature. We then use the theory developed in Ref. [70] and write it in the following function:

```
function [y] = lorFitDoubleLogCorrelated(param,x)
% % fit the data with correlated Lorentzian function
% % Q is defined as Re(w)/(-2Im(w))
% % Q and tau are linked through Q = Re(w)*tau/2
% % the correlated function based on Dr. M. Soltani's theis
% % M. Soltani, Novel integrated silicon nanophotonic structures using ultra-high ...
    Q resonators, (2009).
% % param = [Qi1 Qi2 Qe Qb lam0(nm) C]
% % x is wavelength in nm
% % Qi1: intrinsic Q-factor for resonance 1 (CW or CCW mode)
% % Qi2: intrinsic Q-factor for resonance 2 (CCW or CW mode)
% % Qe: coupling (extrinsic) Q-factor
% % Qb: CW to CCW mode coupling Q
% % lam0: resonant wavelength
% % C: power level adjustment
imj = -sqrt(-1); % j
c0 = 2.99792458e17; % nm

```

```
Qi1 = param(1); % intrinsic Q for resonance 1 (CW or CCW mode)
Qi2 = param(2); % intrinsic Q for resonance 2 (CW or CCW mode)
Qe = param(3); % coupling (extrinsic) Q
Qb = param(4); % CW to CCW mode coupling Q
lam0 = param(5); % center wavelength (nm)
C = param(6); % power level adjustment

lam1 = lam0+0.5*lam0/Qb;
lam2 = lam0-0.5*lam0/Qb;
w1 = 2*pi*c0/lam1;
w2 = 2*pi*c0/lam2;
w0 = 0.5*(w1+w2);

w = 2*pi*c0./x;
ΔW = w-w0;

ge = w0/(Qe);
g1 = w1/(Qi1);
g2 = w2/(Qi2);
gb = w0/Qb;

ac = sqrt(ge/2)./((g1+ge)/2+imj*(ΔW+gb/2));
as = sqrt(ge/2)./((g2+ge)/2+imj*(ΔW-gb/2));

t = -1+sqrt(ge/2)*(ac+as); % transmission amplitude
T = abs(t).^2; % transmission calculated from CMT

y = 10*log10(T)+C; % transform into dB scale + level adjustment
```

Similarly, an automated curve fitting MATLAB script is attached here to fit the spectrum with a resonance split.

```
% % this script is used for fitting to Lorentzian response with single resonance
clear all; close all;
inputFileName = 'input.mat'; % input file name

%% load measurement data from Agilent Laser
f1 = load(inputFileName);
wavelength = f1.Data.Graphs.IL(:,1)*1e9; % wavelength in nm
transmission = -f1.Data.Graphs.IL(:,2); % transmission in dBm
transmission = transmission - max(transmission); % move the transmission to zero level

%% plot the directly measured transmission response
figure1 = figure('Color',[1 1 1]);
```

```
axes1 = axes('Parent',figure1,...
'FontSize',20);
box(axes1,'on');
grid(axes1,'on');
hold(axes1,'all');
plot(wavelength, transmission,'LineWidth',2);
xlabel('Wavelength (nm)');
ylabel('Insertion Loss (dB)');

%% select fitting wavelength range (cover the region of the resonance)
[xx1 yy1] = ginput(2);
selectRange = logical((wavelength>xx1(1)) .* (wavelength<xx1(2)));
wavelengthSelect = wavelength(selectRange);
transmissionSelect = transmission(selectRange);

%% plot selected range
figure1 = figure('Color',[1 1 1]);
axes1 = axes('Parent',figure1,...
'FontSize',20);
box(axes1,'on');
grid(axes1,'on');
hold(axes1,'all');
plot(wavelengthSelect, transmissionSelect,'ob');
xlabel('Wavelength (nm)');
ylabel('Insertion Loss (dB)');
xlim([min(wavelengthSelect) max(wavelengthSelect)]);
hold on;

%% fitting part
%% guess value
Qi1 = 1e6; % intrinsic Q-factor for resonance 1
Qi2 = 1e6; % intrinsic Q-factor for resonance 2
Qe = 2.9e6; % extrinsic Q-factor
Qb = 2e5; % CW to CCW mode coupling Q
[lam0 ER] = ginput(1); % select the center wavelength, ER for extinction
C = max(transmissionSelect); % power level adjustment (dB)
paramStart = [Qi1 Qi2 Qe Qb lam0 C]'; % guess value (fitting starting point)
fprintf('Start:\n Qi1 = %.3f\n Qi2 = %.3f\n Qe = %.3f\n Qb = %.3f\n', ...
paramStart(1), paramStart(2), paramStart(3), paramStart(4));
fprintf('lam0 = %.6f\n C = %.3f\n', paramStart(5), paramStart(6));

%% fitting options
lb = [1e4 1e4 1e4 1e4 1470 -5];
ub = [1e7 1e7 1e8 1e7 1490 2];
options = optimset('lsqcurvefit');
```

```
options = optimset(options,'TolX',1e-13 ,'TolFun',1e-13);
options.MaxFunEvals = 10000;
options.MaxIter = 10000;

%% fitting
[paramEndlsq, error] = lsqcurvefit(@lorFitDoubleLogCorrelated, paramStart,...
wavelengthSelect, transmissionSelect, lb, ub, options);
fprintf('End:\n Qi1 = %.3f\n Qi2 = %.3f\n Qe = %.3f\n Qb = %.3f\n', ...
paramStart(1), paramStart(2), paramStart(3), paramStart(4));
fprintf('lam0 = %.6f\n C = %.3f\n', paramStart(5), paramStart(6));

%% plot fitted curve
wavelengthFit = min(wavelengthSelect):0.05e-3:max(wavelengthSelect); % 0.5pm ...
    resolution
transmissionFit = lorFitSingleLog(paramEndlsq, wavelengthFit);
plot(wavelengthFit, transmissionFit, '-r', 'LineWidth', 2);

%% save fitting data
fileOutputName = 'output.mat';
save(fileOutputName, 'paramEndlsq', 'wavelengthSelect', 'transmissionSelect',...
'wavelengthFit','transmissionFit');
```

Here we also show an example of using the functions and scripts provided earlier to characterize the intrinsic Q-factors of a 150µm-radius microcavity that was discussed in Chap. 4. The measured mode has a TM-like polarization and the measurement focused on wavelengths around 1610nm. After taking the transmission spectra of the same device with different coupling gaps, we processed the experimental data. The transmission spectra and fitted curves using the functions provided before are shown in Fig. .2(a-d). $\Delta\lambda$ is defined by subtracting 1610nm from the absolute wavelength. For a large coupling gap, the cavity is in the under-coupled regime where Q_e is greater than Q_i. The parameters extracted from the spectra are plotted in Fig. .3. We observe that the external Q-factor increases exponentially with the increase of coupling gap size while the intrinsic Q-factor stays mostly the same. Therefore, we can conclude that the measured resonance provided an intrinsic Q-factor of $\sim 1 \times 10^6$.

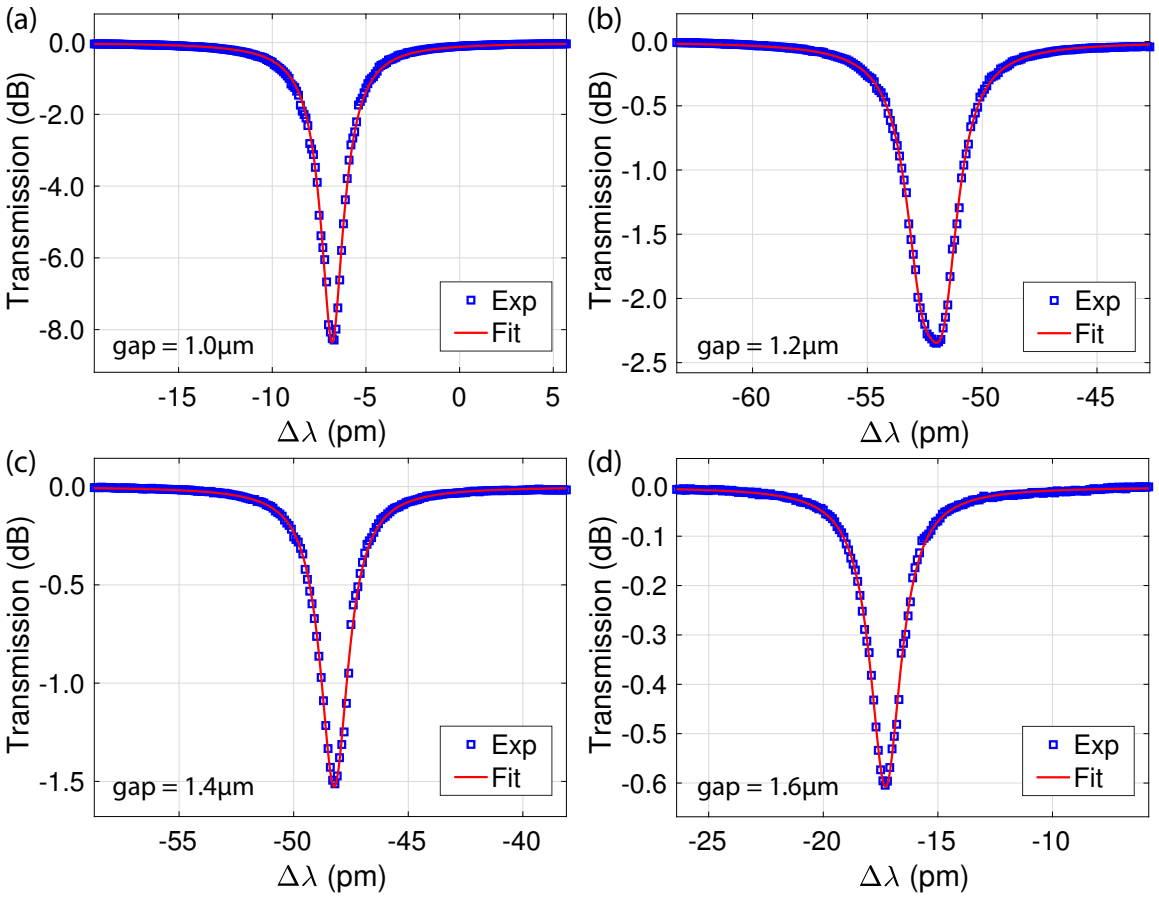

Fig. .2: Transmission spectra and fitting curves for (a) gap = 1.0μm, (b) gap = 1.2μm, (c) gap = 1.4μm and (d) gap = 1.6μm.

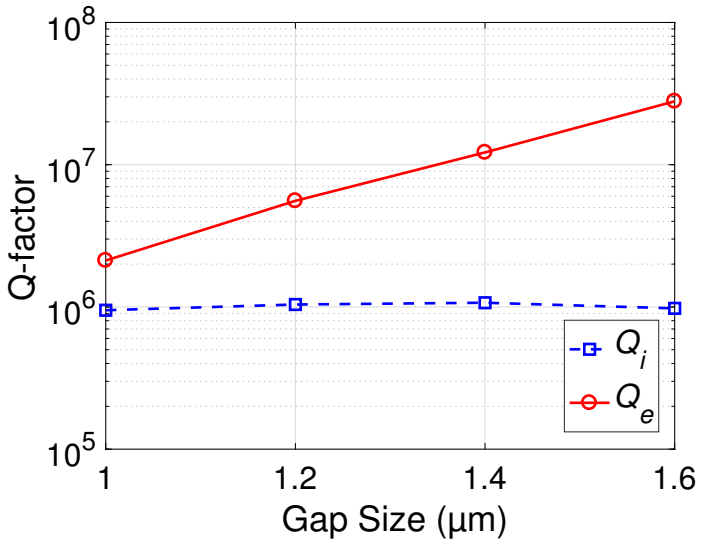

Fig. .3: Q_e and Q_i extracted from measured transmission spectra of microcavity structures with coupling gap sizes from 1.0 to 1.6μm.

C Microcavity Laser Performance Estimation

MATLAB script for microcavity laser performance estimation based on Ref. [110].

```
% microcavity laser theory
% % created based on PRA paper
% B. Min, et al, Erbium-implanted high-Q silica toroidal microcavity laser on a ...
    silicon chip,
% Phys. Rev. A. 70 (2004) 033803. doi:10.1103/PhysRevA.70.033803.
% version 1: 2016-10-01 update
% 1. add ion quenching effect with parameter N_Q to modify tau_Er_NT
% 2. add pump and signal mode mismatch with gamma_sp to modify Giles
% parameter sigma_s_e
% 3. example use 980nm as pump and 1560nm as signal
% 4. parameters are defined with unit cm, s, kg

close all; clear all;
%% Erbium part
N_T = 3.0e20; % average Er3+ concentration cm^{-3}
Q_s_e = 5e6; % signal coupling Q-factor
Q_s_i = 4e5; % signal internal Q-factor
% Q_T_s = 4e5; % total Q factor at signal wavelength (including passive loss + ...
    coupling Q)
n_s = 1.57; % effective index of the signal mode
n_p = 1.57; % effective index of the signal mode
lambda_p = 0.98e-4; % pump wavelength (cm)
lambda_s = 1.56e-4; % signal wavelength (cm)
c0 = 3e10; % cm/s
V_m_p = 2e-8*2*pi*80e-4; % pump mode volumn cm^3
V_m_s = 2e-8*2*pi*80e-4; % signal mode volumn cm^3
Q_p_e = 4e5; % pump coupling Q-factor
Q_p_i = 4e5; % pump internal Q-factor
tau_Er_NT = 7.5e-3; % lifetime of erbium ions (s)
h = 6.626e-30; % planck's constant cm^2*kg/s
N_Q = 5e20; % cm-3 quenching concentration
gamma_sp = 0.7; % modal overlap between pump mode and signal mode

% pump part
Gamma_p = 0.8; % pump mode and gain medium intensity overlap
sigma_p_a = 2e-21; % pump absorption cross-section (cm^2)
sigma_p_e = 0e-21; % pump emission cross-section (cm^2)
% signal part
Gamma_s = 0.8; % signal mode and gain medium intensity overlap
sigma_s_a = 1.77e-21; % signal absorption cross-section (cm^2)
```

```
sigma_s_e = 3.10e-21; % signal emission cross-section (cm^2)

%% life time modification (including ion-quenching)
tau_Er_NT = tau_Er_NT/(1+ (N_T/N_Q)); % lifetime of erbium ions (s)

%% passive cavity signal loss (alpha_s_passive)
Q_T_s = 1/(1/Q_s_e + 1/Q_s_i);
alpha_s_passive = 2*pi*n_s/(lambda_s*Q_T_s);

%% passive cavity pump loss (alpha_p_passive)
Q_T_p = 1/(1/Q_p_e + 1/Q_p_i); % total Q factor at pump wavelength (including ...
    passive loss + coupling Q)
alpha_p_passive = 2*pi*n_p/(lambda_p*Q_T_p);

%% Er ion loss
alpha_Er = n_s/(c0*tau_Er_NT); % Er ion loss

%% Giles parameters
alpha_s = Gamma_s*N_T*sigma_s_a; % signal absorption
alpha_p = Gamma_p*N_T*sigma_p_a; % pump absorption
g_s = gamma_sp*Gamma_s*N_T*sigma_s_e; % signal gain (including the mode mismatch ...
    between pump and signal mode)
g_p = Gamma_p*N_T*sigma_p_e; % pump gain

%% wavelength --> frequency
mu_p = c0/lambda_p; % pump photo frequency (s^-1)
mu_s = c0/lambda_s; % pump photo frequency (s^-1)

%% pump coupling number in CMT theory
kappa_p_square = 2*pi*mu_p/Q_p_e; % pump mode to external

%% signal coupling number in CMT theory
kappa_s_square = 2*pi*mu_s/Q_s_e; % signal mode to external

%% upper population ratio
upperPopulation = (alpha_s + alpha_s_passive)/(alpha_s + g_s);
fprintf('Upper Population is %.4f\n', upperPopulation);

%% threshold calculation
S_th_square_part1 = N_T*h*mu_s*V_m_s * (mu_s*n_s*V_m_s)/(mu_p*n_p*V_m_p) * ...
(c0^2)/(4*n_p^2*kappa_p_square);
S_th_square_part2 = ((alpha_p+alpha_p_passive)*(alpha_s+g_s) - ...
(alpha_p+g_p)*(alpha_s+alpha_s_passive))^2 / (alpha_s+g_s)^2;
S_th_square_part3 = alpha_Er*(alpha_s+alpha_s_passive) / ...
(alpha_p*(alpha_s+g_s) - (alpha_p+g_p)*(alpha_s+alpha_s_passive));
```

```
S_th_square = S_th_square_part1*S_th_square_part2*S_th_square_part3;

% S_th_square_part1
% alpha_p
% alpha_p_passive
% alpha_s_passive
% S_th_square_part2
% S_th_square_part3

fprintf('The threshold power is %.2e mW.\n', S_th_square*0.1);

%% slope efficiency calculation
yetta_part1 = kappa_s_square*(mu_s*n_s*V_m_s)/(mu_p*n_p*V_m_p);
yetta_part2 = (alpha_p*(alpha_s+g_s) - (alpha_p+g_p)*(alpha_s+alpha_s_passive)) ...
/(alpha_s_passive*(alpha_s+g_s));
yetta_part3 = 4*n_p^2*kappa_p_square*(alpha_s+g_s)^2 ...
/c0^2/((alpha_p+alpha_p_passive)*(alpha_s+g_s) - ...
    (alpha_p+g_p)*(alpha_s+alpha_s_passive))^2;
yetta = yetta_part1*yetta_part2*yetta_part3;
% yetta_part1
% yetta_part2
% yetta_part3
fprintf('Slope efficiency is %.4f percent.\n', yetta*100);
```

D Modulator Power Consumption Comparison

While the wavelength filtering, Q-matching and intensity enhancement features of microcavity-based structures are relatively easy to understand, the power consumption reduction property is not clear without investigating specific structures. In the appendix, we will analyze this property by comparing a Mach-Zehnder interferometer based modulator with a microcavity-based one.

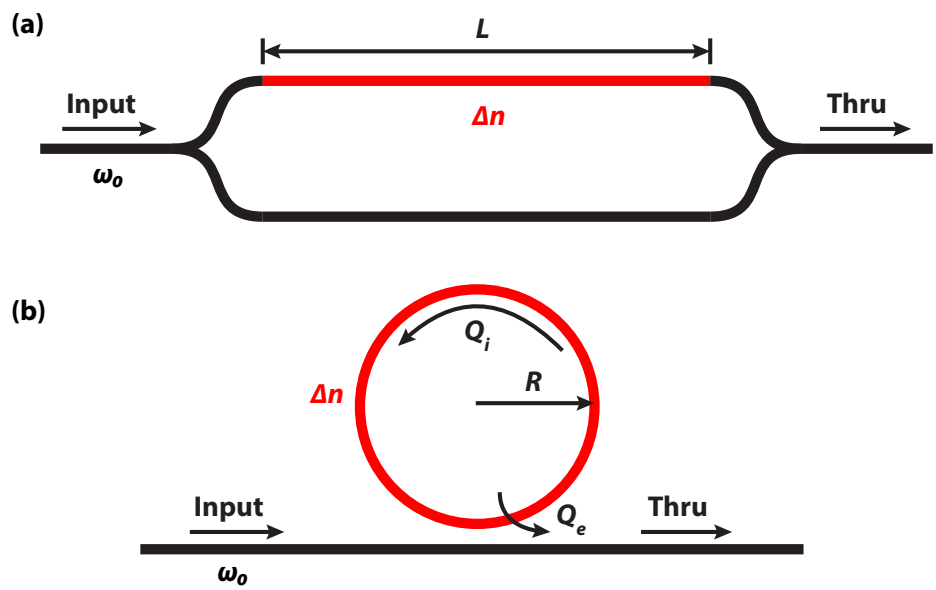

Fig. .4: (a) Mach-Zehnder interferometer-based modulator. (b) Microcavity-based modulator.

Fig. .4(a) shows a schematic of a Mach-Zehnder interferometer based modulator. An input light beam (frequency of ω_0) is split into two arms, and the separated two beams propagate through the arms where the guiding material of one of the arms can change its effective index by Δn. When $\Delta n = 0$, the thru port power of the Mach-Zehnder interferometer is set to half of the input power so as to take advantage of the steep slope of the transmission function to improve modulation extinction. The thru port response can, therefore, be represented as

$$\text{Thru} = \frac{1 + \cos(\pi/2 + 2\pi/\lambda \cdot \Delta n \cdot L)}{2} \tag{D.1}$$

For an index change of $-\Delta n/2$ and $\Delta n/2$, the extinction ratio (ER) can be calculated as

$$\text{ER} = \frac{1 + \cos(\pi/2 - \pi/\lambda \cdot \Delta n \cdot L)}{1 + \cos(\pi/2 + \pi/\lambda \cdot \Delta n \cdot L)} \tag{D.2}$$

We observe that in order to have large effect on the extinction ratio, $\Delta n \cdot L/\lambda$ needs to be on the scale of 1.

For the microcavity-based modulator shown in Fig. .4(b), the model is different. Assuming the microcavity is critical coupled (i.e. $Q_e = Q_i$), the thru port response of the microcavity-based modulator can be represented as

$$\text{Thru} = \frac{(\omega_0 - \omega)^2}{(\omega_0 - \omega)^2 + (\omega_0/Q)^2} \tag{D.3}$$

$$= \frac{(\Delta\lambda/\lambda)^2}{(\Delta\lambda/\lambda)^2 + 1/Q_i^2} \tag{D.4}$$

For a resonance of order m, the resonant wavelength is $m\lambda = n \cdot 2\pi R$. By assuming a weak dependence of the mode effective index on wavelength, we will have $\Delta\lambda = \Delta n \cdot 2\pi R/m$. Therefore, the thru port response can be simplified to

$$\text{Thru} = \frac{(\Delta n/n)^2}{(\Delta n/n)^2 + 1/Q_i^2} \tag{D.5}$$

We notice that in order to have a large effect on the extinction ratio, $Q_i \cdot \Delta n/n$ needs to be on the order of 1.

Similar to the Mach-Zehnder interferometer-based modulator, we set the zero-bias point of microcavity-based modulator to have half of the input power, which corresponds to $\Delta n = \pm n/Q$. This can be achieved by offsetting the input wavelength or applying a DC bias voltage. We choose a starting $\Delta n_0 = -n/Q$ to match to a depletion-based modulator case [3]. The extinction ratio for a index change from $-n/Q - \Delta n/2$ to $-n/Q - \Delta n/2$ is therefore

$$\text{ER} = \frac{(-1/Q_i - \Delta n/n)^2}{(-1/Q_i + \Delta n/n)^2} \cdot \frac{(-1/Q_i + \Delta n/n)^2 + 1/Q_i^2}{(-1/Q_i - \Delta n/n)^2 + 1/Q_i^2} \tag{D.6}$$

As an example, for a microcavity modulator, we assume of Q_i of 8,000, a value that can be achieved using a less than 3µm-radius microdisk cavity. The index is set to 3 for simplicity. The relation between ER and Δn are plotted in Fig. .5(a). To achieve a 6dB-ER modulation, a Δn of 2.015×10^{-4} is required, which is achievable using depletion-based pn-junction structures. Assuming a same Δn of 2.015×10^{-4}, ER as a function of device length of a Mach-Zehnder modulator is shown in Fig. .5(b). A device length (L) of 1.58mm is needed to achieve an ER of 6dB. The increase in device size inevitably adds more to the device capacitance, resulting in a low-speed and high-power consumption performance.

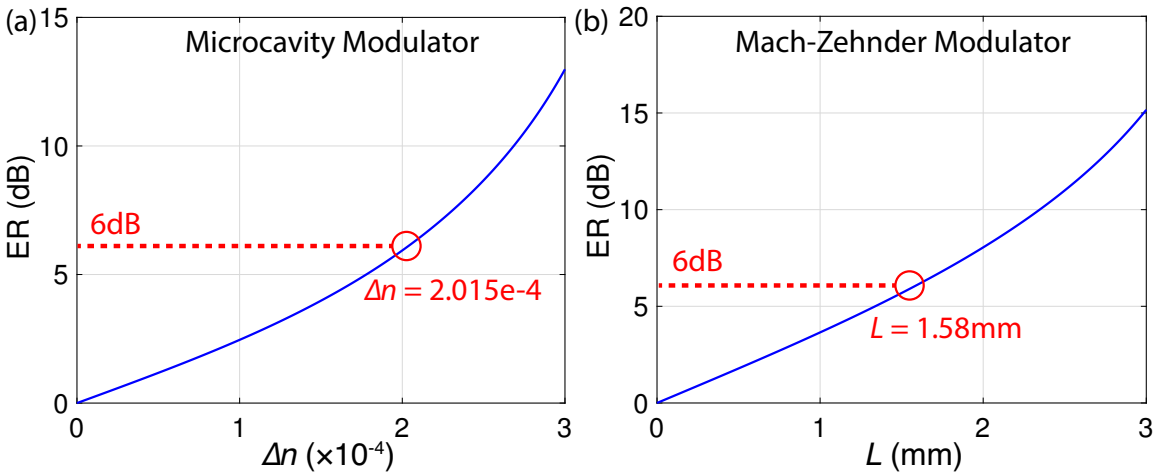

Fig. .5: (a) Extinction ratio vs. Δn for a critical-coupled microcavity-based modulator with Q_i = 8,000. A Δn of 2.015×10^{-4} is needed to for an ER of 6dB. (b) Extinction ratio vs. length for a Mach-Zehnder interferometer-based modulator with a Δn of 2.015×10^{-4}. A device length of 1.58mm is needed to achieve an ER of 6dB.

List of Publications

Peer-Reviewed Journal Articles

1. Z. Su, E. S. Hosseini, E. Timurdogan, J. Sun, M. Moresco, G. Leake, D. D. Coolbaugh, and M. R. Watts, "Resonant-Based Germanium-on-Silicon Photodetector with Evanescent Waveguide Coupling," in preparation for Opt. Lett.

2. Z. Su, N. Li, E. S. Magden, M. Byrd, Purnawirman, T. N. Adam, G. Leake, D. Coolbaugh, J. D. B. Bradley, and M. R. Watts, "Ultra-compact and low-threshold thulium microcavity lasers monolithically integrated on silicon," Opt. Lett. **41**, 5708-5711 (2016).

3. T.-W. Weng, Z. Zhang, Z. Su, Y. Marzouk, A. Melloni, and L. Daniel, "Uncertainty quantification of silicon photonic devices with correlated and non-Gaussian random parameters," Opt. Express **23**, 4242-4254 (2015).

4. Z. Su, M. Cherchi, E. Timurdogan, J. Sun, M. Moresco, G. Leake, D. Coolbaugh, M. R. Watts, "A silicon wavelength selective partial-drop broadcast filter bank," Opt. Lett. **39**, 5459 (2014).

5. J. D. B. Bradley, E. S. Hosseini, Purnawirman, Z. Su, T. N. Adam, G. Leake, D. Coolbaugh, and M. R. Watts, "Monolithic erbium- and ytterbium-doped microring lasers on silicon chips," Opt. Express **22**, 12226-12237 (2014).

6. Z. Su, E. Timurdogan, E. S. Hosseini, J. Sun, G. Leake, D. D. Coolbaugh, and M. R. Watts, "Four-port integrated polarizing beam splitter," Opt. Lett. **39**, 965-968 (2014).

7. J. Sun, E. Timurdogan, A. Yaacobi, Z. Su, E. Hosseini, D. Cole, M. R. Watts, "Large-Scale Silicon Photonic Circuits for Optical Phased Arrays," IEEE J. Sel. Top. Quantum Electron. **20**, 264-278 (2014).

International Conferences

1. Z. Su, J. Bradley, N. Li, E. S. Magden, P. Purnawirman, D. Coleman, N. Fahrenkopf, C. Baiocco, T. Adam, G. Leake, D. Coolbaugh, D. Vermeulen, and M. R. Watts, "Ultra-Compact CMOS-Compatible Ytterbium Microlaser," in Advanced Photonics 2016 (IPR, NOMA, Sensors, Networks, SPPCom, SOF), OSA technical Digest (online) (Optical Society of America, 2016), paper IW1A.3.

2. C. V. Poulton, A. Yaccobi, Z. Su, M. J. Byrd, and M. R. Watts, "Optical Phased Array with Small Spot Size, High Steering Range and Grouped Cascaded Phase Shifters," in Advanced Photonics 2016 (IPR, NOMA, Sensors, Networks, SPPCom, SOF), OSA technical Digest (online) (Optical Society of America, 2016), paper IW1B.2.

3. Z. Su, E. Timurdogan, D. Coleman, N. Fahrenkopf, T. Adam, G. Leake, D. Coolbaugh, D. Caplan, and M. R. Watts, "Second-Order Wavelength-Selective Partial-Drop Multicast Filter Bank," in Advanced Photonics 2016 (IPR, NOMA, Sensors, Networks, SPPCom, SOF), OSA technical Digest (online) (Optical Society of America, 2016), paper ITu1B.7.

4. N. Li, E. Timurdogan, C. Poulton, M. Byrd, E. S. Magden, Z. Su, P. Purnawirman, G. Leake, D. Coolbaugh, D. Vermeulen, and M. Watts, "C-Band Swept Wavelength Erbium-Doped Fiber Laser With a High-Q Tunable Interior-Ridge Silicon Microring Cavity," in Conference on Lasers and Electro-Optics, OSA Technical Digest (2016) (Optical Society of America, 2016), paper SM1G.5.

5. Z. Su, E. Hosseini, E. Timurdogan, J. Sun, M. Moresco, G. Leake, T. N. Adam, D. Coolbaugh, and M. Watts, "Resonant Germanium-on-Silicon Photodetector with Evanescent Waveguide Coupling," in Conference on Lasers and Electro-Optics, OSA Technical Digest (2016) (Optical Society of America, 2016), paper STh4E.4.

6. J. D. B. Bradley, Z. Su, E. S. Magden, N. Li, M. Byrd, Purnawirman, T. N. Adam, G. Leake, D. Coolbaugh, M. R. Watts, "1.8-m thulium microlasers integrated on silicon," Proc. SPIE 9744, Optical Components and Materials XIII,

97440U (February 24, 2016); doi:10.1117/12.2213678.

7. V. Stojanović, K. T. Settaluri, S. Lin, S. Moazeni, E. Timurdogan, C. Sun, M. Moresco, Z. Su, Y.-H. Chen, G. Leake, D. LaTuplipe, C. McDonough, J. Hebding, D. Coolbaugh, M. Watts, "High-density 3D electronic-photonic integration," in Energy Efficient Electronic Systems (E3S), 2015 Fourth Berkeley Symposium on, pp. 1-2, 1-2 Oct. 2015.

8. K. T. Settaluri, S. Lin, S. Moazeni, E. Timurdogan, C. Sun, M. Moresco, Z. Su, Y.-H. Chen, G. Leake, D. LaTuplipe, C. McDonough, J. Hebding, D. Coolbaugh, M. Watts, V. Stojanović, "Demonstration of an optical chip-to-chip link in a 3D integrated electronic-photonic platform," in European Solid-State Circuits Conference (ESSCIRC), ESSCIRC 2015 41st, pp. 156-159, 14-18 Sept. 2015.

9. Z. Su, E. Timurdogan, M. Moresco, G. Leake, D. D. Coolbaugh, and M. R. Watts, "Wavelength Routing and Multicasting Network in Ring-Based Integrated Photonics," in Advanced Photonics 2015, OSA Technical Digest (online) (Optical Society of America, 2015), paper IT4A.3.

10. Z. Su, E. Timurdogan, J. Sun, M. Moresco, G. Leake, D. D. Coolbaugh, and M. R. Watts, "An Interior-Ridge Silicon Microring Switch with Integrated Thermal Tuner," in Advanced Photonics 2015, OSA Technical Digest (online) (Optical Society of America, 2015), paper IM2B.5.

11. E. Timurdogan, Z. Su, K. Settaluri, S. Lin, S. Moazeni, C. Sun, G. Leake, D. D. Coolbaugh, B. R. Moss, M. Moresco, V. Stojanović, M. R. Watts, "An Ultra Low Power 3D Integrated Intra-Chip Silicon Electronic-Photonic Link," in Optical Fiber Communication Conference Post Deadline Papers, OSA Technical Digest (online) (Optical Society of America, 2015), paper Th5B.8.

12. T. Weng, Z. Zhang, Z. Su, and L. Daniel, "Fast Stochastic Simulation of Silicon Waveguide with Non-Gaussian Correlated Process Variations," in Asia Communications and Photonics Conference 2014, OSA Technical Digest (online) (Optical Society of America, 2014), paper AF3B.7.

13. J. Sun, A. Yaacobi, E. Timurdogan, Z. Su, D. Cole, E. S. Hosseini, M. Moresco, G. Leake, D. Coolbaugh, and M. R. Watts, "Large-Scale Integrated Silicon Photonic Circuits for Optical Phased Arrays," in Advanced Photonics for Communications, OSA Technical Digest (online) (Optical Society of America, 2014), paper PT4B.4.

14. Z. Su, E. Timurdogan, E. S. Hosseini, J. Sun, G. Leake, D. Coolbaugh, and M. R. Watts, "Broadband mode-evolution-based four-port polarizing beam splitter," in CLEO: 2014, OSA Technical Digest (online) (Optical Society of America, 2014), paper SF1O.7.

15. M. R. Watts, E. Timurdogan, J. Sun, E. S. Hosseini, C. Sorace-Agaskar, A. Yaacobi, Z. Su, M. Moresco, Purnawirman, J. Bradley, G. Leake, T. Adam, and D. Coolbaugh, "Very Large Scale Silicon Photonics Integration," in CLEO: 2014, OSA Technical Digest (online) (Optical Society of America, 2014), paper SM4O.4.

16. Purnawirman, E. S. Hosseini, M. Moresco, Z. Su, E. Timurdogan, A. Baldycheva, J. Sun, M. R. Watts, T. Adam, G. Leake, and D. Coolbaugh, "Integrated Al2O3:Er3+ DFB Laser for Temperature Control Free Operation with Silicon Nitride Ring Filter," in CLEO: 2014, OSA Technical Digest (online) (Optical Society of America, 2014), paper SM4G.5.

17. E. Timurdogan, Z. Su, J. Sun, M. Moresco, G. Leake, D. Coolbaugh, and M. R. Watts, "A High-Q Tunable Interior-Ridge Microring Filter," in CLEO: 2014, OSA Technical Digest (online) (Optical Society of America, 2014), paper SF2O.3.

18. Z. Su, E. Timurdogan, J. Sun, M. Moresco, G. Leake, D. Coolbaugh, and M. R. Watts, "An on-chip partial drop wavelength selective broadcast network," in CLEO: 2014, OSA Technical Digest (online) (Optical Society of America, 2014), paper SF2O.4.

19. Z. Su, E. S. Hosseini, E. Timurdogan, J. Sun, G. Leake, D. Coolbaugh, and M. R. Watts, "Reduced Wafer-Scale Frequency Variation in Adiabatic Microring

Resonators," in Optical Fiber Communication Conference, OSA Technical Digest (online) (Optical Society of America, 2014), paper Th2A.55.

References

[1] R. Kumar, V. Zyuban, and D. M. Tullsen, "Interconnections in multi-core architectures: understanding mechanisms, overheads and scaling," 32nd International Symposium on Computer Architecture (ISCA'05) pp. 408–419 (2005).

[2] A. Shacham, K. Bergman, and L. P. Carloni, "Photonic networks-on-chip for future generations of chip multiprocessors," IEEE Trans. Comput. **57**, 1246–1260 (2008).

[3] E. Timurdogan, C. M. Sorace-Agaskar, J. Sun, E. S. Hosseini, A. Biberman, and M. R. Watts, "An ultralow power athermal silicon modulator," Nat. Commun. **5**, 4008 (2014).

[4] J. Sun, E. Timurdogan, A. Yaacobi, E. S. Hosseini, and M. R. Watts, "Large-scale nanophotonic phased array," Nature **493**, 195–199 (2013).

[5] J. C. Matthews, A. Politi, A. Stefanov, and J. L. O'Brien, "Manipulation of multiphoton entanglement in waveguide quantum circuits," Nat. Photon. **3**, 346–350 (2009).

[6] M. R. Watts, D. C. Trotter, and R. W. Young, "Ultralow power silicon microdisk modulators and switches," 5th IEEE International Conference on Group IV Photonics pp. 4–6 (2008).

[7] M. R. Watts, W. A. Zortman, D. C. Trotter, R. W. Young, and A. L. Lentine, "Vertical junction silicon microdisk modulators and switches," Opt. Express **19**, 21989–22003 (2011).

[8] Z. Su, E. Timurdogan, J. Sun, M. Moresco, G. Leake, D. Coolbaugh, and M. Watts, "An Interior-Ridge Silicon Microring Switch with Integrated Thermal Tuner," Advanced Photonics, paper IM2B.5 (2015).

[9] C. T. DeRose, D. C. Trotter, W. A. Zortman, A. L. Starbuck, M. Fisher, M. R. Watts, and P. S. Davids, "Ultra compact 45 GHz CMOS compatible Germanium

waveguide photodiode with low dark current," Opt. Express **19**, 24897–24904 (2011).

[10] Purnawirman, J. Sun, T. N. Adam, G. Leake, D. Coolbaugh, J. D. B. Bradley, E. S. Hosseini, and M. R. Watts, "C- and L-band erbium-doped waveguide lasers with wafer-scale silicon nitride cavities," Opt. Lett. **38**, 1760–1762 (2013).

[11] J. Bradley, E. S. Hosseini, Purnawirman, Z. Su, T. N. Adam, G. Leake, D. D. Coolbaugh, and M. R. Watts, "Monolithic erbium-and ytterbium-doped microring lasers on silicon chips," Opt. Express **22**, 12226–12237 (2014).

[12] Y. Zhang, S. Yang, A. E.-J. Lim, G.-Q. Lo, C. Galland, T. Baehr-Jones, and M. Hochberg, "A compact and low loss Y-junction for submicron silicon waveguide," Opt. Express **21**, 1310–1316 (2013).

[13] W. Bogaerts, P. Dumon, D. V. Thourhout, and R. Baets, "Low-loss, low-cross-talk crossings for silicon-on-insulator nanophotonic waveguides," Opt. Lett. **32**, 2801–2803 (2007).

[14] E. Timurdogan, Z. Su, K. Settaluri, S. Lin, S. Moazeni, C. Sun, G. Leake, D. D. Coolbaugh, B. Moss, M. Moresco, V. Stojanović, and M. R. Watts, "An Ultra Low Power 3D Integrated Intra-Chip Silicon Electronic-Photonic Link," Optical Fiber Conference, paper Th5B.8 (2015).

[15] K. T. Settaluri, S. Lin, S. Moazeni, E. Timurdogan, C. Sun, M. Moresco, Z. Su, Y.-H. Chen, G. Leake, D. LaTulipe, C. McDonough, J. Hebding, D. Coolbaugh, M. Watts, and V. Stojanović, "Demonstration of an optical chip-to-chip link in a 3D integrated electronic-photonic platform," ESSCIRC Conference 2015 - 41st European Solid-State Circuits Conference pp. 156–159 (2015).

[16] V. Stojanović, K. T. Settaluri, S. Lin, S. Moazeni, E. Timurdogan, C. Sun, M. Moresco, Z. Su, Y. H. Chen, G. Leake, D. LaTulipe, C. McDonough, J. Hebding, D. Coolbaugh, and M. Watts, "High-density 3d electronic-photonic integration," 2015 Fourth Berkeley Symposium on Energy Efficient Electronic Systems (E3S) pp. 1–2 (2015).

[17] Z. Su, E. Timurdogan, E. S. Hosseini, J. Sun, G. Leake, D. D. Coolbaugh, and M. R. Watts, "Four-port integrated polarizing beam splitter," Opt. Lett. **39**, 965–968 (2014).

[18] Z. Su, E. Timurdogan, E. S. Hosseini, and J. Sun, "Broadband mode-evolution-based four-port polarizing beam splitter," Conference on Lasers and Electro-Optics, paper SF2O.3 (2014).

[19] Z. Su, E. S. Hosseini, E. Timurdogan, J. Sun, G. Leake, D. D. Coolbaugh, and M. R. Watts, "Reduced wafer-scale frequency variation in adiabatic microring resonators," Optical Fiber Conference, paper Th5B.8 (2014).

[20] J. Sun, E. Timurdogan, A. Yaacobi, Z. Su, E. S. Hosseini, D. B. Cole, and M. R. Watts, "Large-Scale Silicon Photonic Circuits for Optical Phased Arrays," IEEE J. Sel. Top. Quantum Electron. **20**, 264–278 (2014).

[21] C. V. Poulton, A. Yaccobi, Z. Su, M. J. Byrd, and M. R. Watts, "Optical Phased Array with Small Spot Size, High Steering Range and Grouped Cascaded Phase Shifters," Advanced Photonics 2016 (IPR, NOMA, Sensors, Networks, SPP-Com, SOF), paper IW1B.2 (2016).

[22] J. Sun, A. Yaacobi, E. Timurdogan, Z. Su, D. Cole, E. S. Hosseini, M. Moresco, G. Leake, D. Coolbaugh, and M. R. Watts, "Large-Scale Integrated Silicon Photonic Circuits for Optical Phased Arrays," Advanced Photonics for Communications, paper PT4B.4. (2014).

[23] R. Soref and B. Bennett, "Electrooptical effects in silicon," IEEE J. Quant. Electron. **23**, 123–129 (1987).

[24] E. Timurdogan, Z. Su, J. Sun, M. Moresco, G. Leake, D. D. Coolbaugh, and M. R. Watts, "A high-Q tunable interior-ridge microring filter," Conference on Lasers and Electro-Optics, paper SF2O.3 (2014).

[25] E. Timurdogan, E. S. Hosseini, G. Leake, D. D. Coolbaugh, and M. R. Watt, "L-Shaped Resonant Microring (LRM) Filter with Integrated Thermal Tuner," Conference on Lasers and Electro-Optics, paper SF2O.3 (2013).

[26] N. Li, E. Timurdogan, C. V. Poulton, M. Byrd, E. S. Magden, Z. Su, Purnawirman, G. Leake, D. D. Coolbaugh, D. Vermeulen, and M. R. Watts, "C-band swept wavelength erbium-doped fiber laser with a high-q tunableinterior-ridge silicon microring cavity," Opt. Express **24**, 22741–22748 (2016).

[27] N. Li, E. Timurdogan, C. Poulton, M. Byrd, E. S. Magden, Z. Su, P. Purnawirman, G. Leake, D. Coolbaugh, D. Vermeulen, and M. Watts, "C-Band Swept Wavelength Erbium-Doped Fiber Laser With a High-Q Tunable Interior-Ridge Silicon Microring Cavity," Conference on Lasers and Electro-Optics, paper SM1G.5 (2016).

[28] Z. Su, M. Cherchi, E. Timurdogan, J. Sun, M. Moresco, G. Leake, D. Coolbaugh, and M. R. Watts, "Silicon wavelength-selective partial-drop broadcast filter bank," Opt. Lett. **39**, 5459–5462 (2014).

[29] Z. Su, E. Timurdogan, J. Sun, M. Moresco, G. Leake, D. Coolbaugh, and M. R. Watts, "An on-chip partial drop wavelength selective broadcast network," Conference on Lasers and Electro-Optics, paper SF2O.4 (2014).

[30] Z. Su, E. Timurdogan, M. Moresco, G. Leake, D. D. Coolbaugh, and M. R. Watts, "Wavelength Routing and Multicasting Network in Ring-Based Integrated Photonics," Advanced Photonics, paper IT4A.3 (2015).

[31] Z. Su, E. Hosseini, E. Timurdogan, J. Sun, M. Moresco, G. Leake, T. N. Adam, D. Coolbaugh, and M. Watts, "Resonant Germanium-on-Silicon Photodetector with Evanescent Waveguide Coupling," Conference on Lasers and Electro-Optics, paper STh4E.4 (2016).

[32] J. D. B. Bradley, Z. Su, E. S. Magden, N. Li, M. Byrd, P. Purnawirman, T. N. Adam, G. Leake, D. Coolbaugh, and M. R. Watts, "1.8-μm thulium microlasers integrated on silicon," Proc. SPIE 9744, Optical Components and Materials XIII, 97440U (2016).

[33] B. E. Little, S. T. Chu, H. A. Haus, J. Foresi, and J. P. Laine, "Microring resonator channel dropping filters," J. Lightwave Technol. **15**, 998–1005 (1998).

[34] K. K. Mehta, K. K. Mehta, J. S. Orcutt, J. M. Shainline, O. Tehar-Zahav, Z. Sternberg, R. Meade, M. A. Popović, and R. J. Ram, "Polycrystalline silicon ring resonator photodiodes in a bulk complementary metal-oxide-semiconductor process," Opt. Lett. **39**, 1061–1064 (2014).

[35] K. Preston, Y. H. D. Lee, M. Zhang, M. Zhang, and M. Lipson, "Waveguide-integrated telecom-wavelength photodiode in deposited silicon," Opt. Lett. **36**, 52–54 (2011).

[36] W. A. Zortman, D. C. Trotter, and M. R. Watts, "Silicon photonics manufacturing," Opt. Express **18**, 23598–23607 (2010).

[37] K. J. Vahala, "Optical microcavities," Nature **424**, 839–846 (2003).

[38] Y. Okawachi, K. Saha, J. S. Levy, Y. H. Wen, M. Lipson, and A. L. Gaeta, "Octave-spanning frequency comb generation in a silicon nitride chip," Opt. Lett. **36**, 3398–3400 (2011).

[39] A. C. Turner, M. A. Foster, A. L. Gaeta, and M. Lipson, "Ultra-low power parametric frequency conversion in a silicon microring resonator," Opt. Express **16**, 4881–4887 (2008).

[40] E. Timurdogan, C. M. Sorace-Agaskar, G. Leake, D. D. Coolbaugh, and M. R. Watts, "Adiabatic Resonant Microring (ARM) Modulators with Integrated Thermal Tuner," Advanced Photonics, IT4A.3 (2013).

[41] E. Timurdogan, "Wafer-Scale Integrated Active Silicon Photonics for Manipulation and Conversion of Light," Ph.D. thesis, Massachusetts Institute of Technology (2016).

[42] Z. Su, E. Timurdogan, D. Coleman, N. Fahrenkopf, T. Adam, G. Leake, D. Coolbaugh, D. Caplan, and M. R. Watts, "Second-Order Wavelength-Selective Partial-Drop Multicast Filter Bank," Advanced Photonics (IPR, NOMA, Sensors, Networks, SPPCom, SOF), paper ITu1B.7 (2016).

[43] Z. Su, J. Bradley, N. Li, E. S. Magden, P. Purnawirman, D. Coleman, N. Fahrenkopf, C. Baiocco, T. Adam, G. Leake, D. Coolbaugh, D. Vermeulen,

and M. R. Watts, "Ultra-Compact CMOS-Compatible Ytterbium Microlaser," Advanced Photonics (IPR, NOMA, Sensors, Networks, SPPCom, SOF), paper IW1A.3 (2016).

[44] Z. Su, N. Li, E. Salih Magden, M. Byrd, Purnawirman, T. N. Adam, G. Leake, D. Coolbaugh, J. D. B. Bradley, and M. R. Watts, "Ultra-compact and low-threshold thulium microcavity laser monolithically integrated on silicon," Opt. Lett. **41**, 5708–4 (2016).

[45] N. Kirman, M. Kirman, R. K. Dokania, J. F. Martinez, A. B. Apsel, M. A. Watkins, and D. H. Albonesi, "Leveraging Optical Technology in Future Bus-based Chip Multiprocessors," 39th Annual IEEE/ACM International Symposium on Microarchitecture (MICRO'06) pp. 492–503 (2006).

[46] L. G. Kazovsky, W.-T. Shaw, D. Gutierrez, N. Cheng, and S.-W. Wong, "Next-Generation Optical Access Networks," J. Lightwave Technol. **25**, 3428–3442 (2007).

[47] D. T. Spencer, D. Dai, Y. Tang, M. J. R. Heck, and J. E. Bowers, "Realization of a Novel 1×N Power Splitter With Uniformly Excited Ports," IEEE Photonics Technol. Lett. **25**, 36–39 (2013).

[48] J. D. Joannopoulos, S. G. Johnson, J. N. Winn, and R. D. Meade, "Photonic crystals: molding the flow of light," Princeton University Press, 2nd ed. (2008).

[49] M. A. Popovic, C. Manolatou, and M. R. Watts, "Coupling-induced resonance frequency shifts in coupled dielectric multi-cavity filters," Opt. Express **14**, 1208–1222 (2006).

[50] M. R. Watts, W. A. Zortman, D. C. Trotter, G. N. Nielson, D. L. Luck, and R. W. Young, "Adiabatic Resonant Microrings (ARMs) with Directly Integrated Thermal Microphotonics," Conference on Lasers and Electro-Optics/International Quantum Electronics Conference, paper CPDB10 (2009).

[51] A. Biberman, B. G. Lee, A. C. Turner-Foster, M. A. Foster, M. Lipson, A. L. Gaeta, and K. Bergman, "Wavelength multicasting in silicon photonic nanowires," Opt. Express **18**, 18047–18055 (2010).

[52] M. Asghari and A. V. Krishnamoorthy, "Silicon photonics: Energy-efficient communication," Nat. Photon. **5**, 268–270 (2011).

[53] F. Y. Liu, D. Patil, J. Lexau, P. Amberg, M. Dayringer, J. Gainsley, H. F. Moghadam, X. Zheng, J. E. Cunningham, A. V. Krishnamoorthy, E. Alon, and R. Ho, "10-Gbps, 5.3-mW Optical Transmitter and Receiver Circuits in 40-nm CMOS," IEEE Journal of Solid-State Circuits **47**, 2049–2067 (2012).

[54] J. Michel, J. Liu, and L. C. Kimerling, "High-performance Ge-on-Si photodetectors," Nat. Photon. **4**, 527–534 (2010).

[55] D. Feng, S. Liao, P. Dong, N. N. Feng, and H. Liang, "High-speed Ge photodetector monolithically integrated with large cross-section silicon-on-insulator waveguide," Appl. Phys. Lett. **95**, 261105 (2009).

[56] A. Novack, M. Gould, Y. Yang, Z. Xuan, M. Streshinsky, Y. Liu, G. Capellini, A. E.-J. Lim, G.-Q. Lo, T. Baehr-Jones, and M. Hochberg, "Germanium photodetector with 60 GHz bandwidth using inductive gain peaking," Opt. Express **21**, 28387–28393 (2013).

[57] L. Vivien, A. Polzer, D. Marris-Morini, and J. Osmond, "Zero-bias 40Gbit/s germanium waveguide photodetector on silicon," Opt. Express **20**, 1096–1101 (2012).

[58] G. Li, Y. Luo, X. Zheng, G. Masini, A. Mekis, S. Sahni, H. Thacker, J. Yao, I. Shubin, K. Raj, J. E. Cunningham, and A. V. Krishnamoorthy, "Improving CMOS-compatible Germanium photodetectors," Opt. Express **20**, 26345–26350 (2012).

[59] S. Liao, N.-N. Feng, D. Feng, P. Dong, R. Shafiiha, C.-C. Kung, H. Liang, W. Qian, Y. Liu, J. Fong, J. E. Cunningham, Y. Luo, and M. Asghari, "36 GHz submicron silicon waveguide germanium photodetector," Opt. Express **19**, 10967–10972 (2011).

[60] D. F. Logan, P. Velha, M. Sorel, R. M. De La Rue, A. P. Knights, and P. E. Jessop, "Defect-Enhanced Silicon-on-Insulator Waveguide Resonant Photode-

tector With High Sensitivity at 1.55 μm," IEEE Photonics Technol. Lett. **22**, 1530–1532 (2010).

[61] J. Brouckaert, G. Roelkens, D. Van Thourhout, and R. Baets, "Thin-Film III-V Photodetectors Integrated on Silicon-on-Insulator Photonic ICs," J. Lightwave Technol. **25**, 1053–1060 (2007).

[62] H. Park, A. W. Fang, R. Jones, O. Cohen, O. Raday, M. N. Sysak, M. J. Paniccia, and J. E. Bowers, "A hybrid AlGaInAs-silicon evanescent waveguide photodetector," Opt. Express **15**, 6044–6052 (2007).

[63] Z. Sheng, L. Liu, J. Brouckaert, and S. He, "InGaAs PIN photodetectors integrated on silicon-on-insulator waveguides," Opt. Express **18**, 1756–1761 (2010).

[64] D. K. T. Ng, Q. Wang, J. Pu, K. P. Lim, Y. Wei, Y. Wang, Y. Lai, and S. T. Ho, "Demonstration of heterogeneous III–V/Si integration with a compact optical vertical interconnect access," Opt. Lett. **38**, 5353–5356 (2013).

[65] F. H. L. Koppens, D. E. Chang, and F. J. García de Abajo, "Graphene Plasmonics: A Platform for Strong Light–Matter Interactions," Nano Lett. **11**, 3370–3377 (2011).

[66] E. D. Palik, "Handbook of Optical Constants of Solids," Academic Press (1997).

[67] H. A. Haus and W. Huang, "Coupled-mode theory," Proceedings of the IEEE **79**, 1505–1518 (1991).

[68] E. S. Hosseini, S. Yegnanarayanan, A. H. Atabaki, M. Soltani, and A. Adibi, "Systematic design and fabrication of high-Q single-mode pulley-coupled planar silicon nitride microdisk resonators at visible wavelengths," Opt. Express **18**, 2127–2136 (2010).

[69] Purnawirman, E. S. Hosseini, M. Moresco, Z. Su, E. Timurdogan, A. Baldycheva, J. Sun, M. R. Watts, T. Adam, G. Leake, and D. Coolbaugh, "Integrated Al_2O_3:Er^{3+} DFB Laser for Temperature Control Free Operation with Silicon Nitride Ring Filter," Conference on Lasers and Electro-Optics, paper SM4G.5 (2014).

[70] M. Soltani, "Novel integrated silicon nanophotonic structures using ultra-high Q resonators," Ph.D. thesis, California Institute of Technology (2009).

[71] Q. Wang, J. Geng, and S. Jiang, "2-μm fiber laser sources for sensing," Opt. Eng. **53**, 061609 (2014).

[72] K. Scholle, S. Lamrini, P. Koopmann, and P. Fuhrberg, "2 µm laser sources and their possible applications," In Tech, India pp. 471–500 (2010).

[73] G. Huber, C. Kränkel, and K. Petermann, "Solid-state lasers: status and future [Invited]," JOSA B **27**, B93–B105 (2010).

[74] W. Ryba-Romanowski, R. Lisiecki, H. Jelinková, and J. Šulc, "Thulium-doped vanadate crystals: Growth, spectroscopy and laser performance," Prog. in Quant. Electron. **35**, 109–157 (2011).

[75] M. Gaponenko, N. Kuleshov, and T. Südmeyer, "Efficient diode-pumped Tm:KYW 19-μm microchip laser with 1 W cw output power," Opt. Express **22**, 11578–11582 (2014).

[76] D. J. Richardson, J. Nilsson, and W. A. Clarkson, "High power fiber lasers: current status and future perspectives [Invited]," JOSA B **27**, B63–B92 (2010).

[77] S. D. Jackson, "Towards high-power mid-infrared emission from a fibre laser," Nat. Photon. **6**, 423–431 (2012).

[78] C. W. Rudy, M. J. F. Digonnet, and R. L. Byer, "Advances in 2-µm Tm-doped mode-locked fiber lasers," Opt. Fiber Technol. **20**, 642–649 (2014).

[79] J. Li, Z. Sun, H. Luo, Z. Yan, K. Zhou, Y. Liu, and L. Zhang, "Wide wavelength selectable all-fiber thulium doped fiber laser between 1925 nm and 2200 nm," Opt. Express **22**, 5387–5399 (2014).

[80] A. Rameix, C. Borel, B. Chambaz, and B. Ferrand, "An efficient, diode-pumped, 2μm Tm: YAG waveguide laser," Opt. Lett. **142**, 239–243 (1997).

[81] D. P. Shepherd, G. Kakarantzas, P. D. Townsend, D. J. B. Brinck, J. Wang, A. C. Tropper, and D. C. Hanna, "1.9-μm operation of a Tm:lead germanate glass waveguide laser," Opt. Lett. **19**, 954–956 (1994).

[82] S. Rivier, X. Mateos, V. Petrov, U. Griebner, Y. E. Romanyuk, C. N. Borca, F. Gardillou, and M. Pollnau, "Tm:$KY(WO_4)_2$ waveguide laser," Opt. Express **15**, 5885–5892 (2007).

[83] W. Bolanos, F. Starecki, A. Benayad, G. Brasse, V. Ménard, J.-L. Doualan, A. Braud, R. Moncorgé, and P. Camy, "Tm:$LiYF_4$ planar waveguide laser at 1.9 μm," Opt. Lett. **37**, 4032–4034 (2012).

[84] E. Cantelar, J. A. Sanz-García, G. Lifante, F. Cussó, and P. L. Pernas, "Single polarized Tm^{3+} laser in Zn-diffused $LiNbO_3$ channel waveguides," Appl. Phys. Lett. **86**, 161119 (2005).

[85] D. G. Lancaster, S. Gross, M. J. Withford, and T. M. Monro, "Widely tunable short-infrared thulium and holmium doped fluorozirconate waveguide chip lasers," Opt. Express **22**, 25286–25294 (2014).

[86] K. van Dalfsen, S. Aravazhi, C. Grivas, S. M. García-Blanco, and M. Pollnau, "Thulium channel waveguide laser with 16W of output power and 80% slope efficiency," Opt. Lett. **39**, 4380–4383 (2014).

[87] J. Wu, S. Jiang, T. Qua, M. Kuwata-Gonokami, and N. Peyghambarian, "2μm lasing from highly thulium doped tellurite glass microsphere," Appl. Phys. Lett. **87**, 211118 (2005).

[88] A. Pal, S. Y. Chen, R. Sen, T. Sun, and K. T. V. Grattan, "A high- Qlow threshold thulium-doped silica microsphere laser in the 2 μm wavelength region designed for gas sensing applications," Laser Phys. Lett. **10**, 085101 (2013).

[89] F. Vanier, "Low threshold lasing at 1975 nm in thulium-doped tellurite glass microspheres," Opt. Lett. **40**, 5227–5230 (2015).

[90] R. Soref, "Mid-infrared photonics in silicon and germanium," Nat. Photon. **4**, 495–497 (2010).

[91] G. Roelkens, U. Dave, A. Gassenq, N. Hattasan, C. Hu, B. Kuyken, F. Leo, A. Malik, M. Muneeb, E. Ryckeboer, D. Sanchez, S. Uvin, R. Wang, Z. Hens,

R. Baets, Y. Shimura, F. Gencarelli, B. Vincent, R. Loo, J. Van Campenhout, L. Cerutti, J.-B. Rodriguez, E. Tournie, X. Chen, M. Nedeljkovic, G. Mashanovich, L. Shen, N. Healy, A. C. Peacock, X. Liu, R. Osgood, and W. M. J. Green, "Silicon-Based Photonic Integration Beyond the Telecommunication Wavelength Range," IEEE J. Sel. Top. Quantum Electron. **20**, 394–404 (2014).

[92] J. J. Ackert, D. J. Thomson, L. Shen, and A. C. Peacock, "High-speed detection at two micrometres with monolithic silicon photodiodes," Nat. Photon. **9**, 393–397 (2015).

[93] J. D. B. Bradley and M. Pollnau, "Erbium-doped integrated waveguide amplifiers and lasers," Laser Photon. Rev. **5**, 368–403 (2010).

[94] S. Mehrabani and A. M. Armani, "Blue upconversion laser based on thulium-doped silica m icrocavity," Opt. Lett. **38**, 4346–4349 (2013).

[95] H. Fan, X. Jiang, Y. Ding, and M. Xiao, "Demonstration of ultralow-threshold 2 micrometer microlasers on chip," Science China Physics, Mechanics & Astronomy **58**, 114204 (2015).

[96] M. J. Digonnet, "Rare-earth-doped fiber lasers and amplifiers, revised and expanded," CRC press (2001).

[97] K. Koski, J. Hölsä, and P. Juliet, "Voltage controlled reactive sputtering process for aluminium oxide thin films," Thin Solid Films **326**, 189–193 (1998).

[98] Purnawirman, E. S. Hosseini, J. Sun, T. N. Adam, G. Leake, D. D. Coolbaugh, M. R. Watts, A. Baldycheva, and J. D. Bradley, "Erbium-Doped Laser with Multi-segmented Silicon Nitride Structure," Optical Fiber Communication Conference, paper W4E.5 (2014).

[99] A. Arbabi, S. M. Kamali, E. Arbabi, and B. G. Griffin, "Grating integrated single mode microring laser," Opt. Express **23**, 5335–5347 (2015).

[100] Y.-F. Xiao, C.-L. Zou, Y. Li, C.-H. Dong, Z.-F. Han, and Q. Gong, "Asymmetric resonant cavities and their applications in optics and photonics: a review," Front. Optoelectron. China **3**, 109–124 (2010).

[101] X.-F. Jiang, Y.-F. Xiao, C.-L. Zou, L. He, C.-H. Dong, B.-B. Li, Y. Li, F.-W. Sun, L. Yang, and Q. Gong, "Highly Unidirectional Emission and Ultralow-Threshold Lasing from On-Chip Ultrahigh-Q Microcavities," Adv. Mat. **24**, OP260–OP264 (2012).

[102] X.-F. Jiang, C.-L. Zou, L. Wang, Q. Gong, and Y.-F. Xiao, "Whispering-gallery microcavities with unidirectional laser emission," Laser Photon. Rev. **10**, 40–61 (2016).

[103] M. Soltani, J. Lin, R. A. Forties, J. T. Inman, S. N. Saraf, R. M. Fulbright, M. Lipson, and M. D. Wang, "Nanophotonic trapping for precise manipulation of biomolecular arrays," Nat. Nanotechnol. **9**, 448–452 (2014).

[104] A. H. J. Yang, S. D. Moore, B. S. Schmidt, M. Klug, M. Lipson, and D. Erickson, "Optical manipulation of nanoparticles and biomolecules in sub-wavelength slot waveguides," Nature **457**, 71–75 (2008).

[105] J. L. O'Brien, A. Furusawa, and J. Vučković, "Photonic quantum technologies," Nat. Photon. **3**, 687–695 (2009).

[106] S. C. Masmanidis, R. B. Karabalin, I. De Vlaminck, G. Borghs, M. R. Freeman, and M. L. Roukes, "Multifunctional Nanomechanical Systems via Tunably Coupled Piezoelectric Actuation," Science **317**, 780–783 (2007).

[107] L. He, Ş. K. Özdemir, J. Zhu, W. Kim, and L. Yang, "Detecting single viruses and nanoparticles using whispering gallery microlasers," Nat. Nanotechnol. **6**, 428–432 (2011).

[108] J. Ward and O. Benson, "WGM microresonators: sensing, lasing and fundamental optics with microspheres," Laser Photon. Rev. **5**, 553–570 (2011).

[109] M. R. Watts, "Adiabatic microring resonators," Opt. Lett. **35**, 3231–3233 (2010).

[110] B. Min, T. J. Kippenberg, L. Yang, K. J. Vahala, and J. Kalkman, "Erbium-implanted high-Q silica toroidal microcavity laser on a silicon chip," Phys. Rev. A **70**, 033803 (2004).